UNIVERSITY OF CAPE TOWN
IYUNIVESITHI YASEKAPA • UNIVERSITEIT VAN KAAPSTAD

Computational simulation of bone remodelling post reverse total shoulder arthroplasty

by

Helen Liedtke

Dissertation Presented in Partial Fulfilment for the Degree of
Master of Science in Mechanical Engineering
University of Cape Town

February 20, 2017

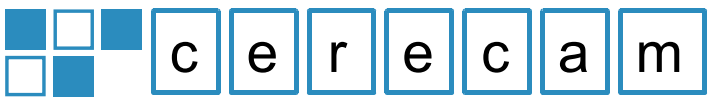

Declaration

I know the meaning of plagiarism and declare that all the work in the document, save for that which is properly acknowledged, is my own.

This thesis/dissertation has been submitted to the Turnitin module (or equivalent similarity and originality checking software) and I confirm that my supervisor has seen my report and any concerns revealed by such have been resolved with my supervisor.

Signed by candidate 9.12.2016

(H. Liedtke)

Acknowledgements

I would like to thank my supervisor Andrew McBride for the guidance and all the help.

I also thank Prof Reddy for making it possible to attend the GAMM-DMV conference in Germany. It was a great experience.

Andie, thanks for teaching me the hexablocking technique in ANSA!
Damien, thanks for always being one step ahead in AceGen and helping me when I was stuck.
Ritesh, thanks for always helping me with PC related issues.

The help and information for the reverse shoulder model provided by Jonathan Glenday from the Division of Biomedical Engineering at UCT and Andreas Kontaxis at the Leon Root Motion Analysis Laboratory at the Hospital for Special Surgery in New York City is greatly appreciated.

The input from Sudesh Sivarasu and Stephen Roche is also gratefully acknowledged.

Further, the statistical shape model provided by Tinashe Mutsvangwa in the Department of Biomedical Engineering at UCT is gratefully acknowledged.

Finally, I would like to thank my family for supporting me throughout my master's studies.

Contents

1

Introduction

Reverse total shoulder arthroplasty is a surgical procedure to restore the integrity and functionality of the shoulder joint for rotator cuff deficient patients. In the reverse procedure, the humeral head is removed and a stem is placed in the central channel of the humerus with a polyethylene cup press fitted into the top. A hemispherical implant, termed the glenosphere, is screwed into the glenoid component of the scapula (shoulder blade). Many complications are reported post procedure, up to 75 % in some clinical series (Hsu et al., 2011).

A common issue in orthopaedics is stress shielding, where the orthopaedic implant carries the majority of the load, resulting in the bone not experiencing the full mechanical stress. Bone is a complex, living tissue, which responds to variations in the loading environment by changing density and trabecular orientations, resulting in changes in material properties. This phenomenon is termed bone remodelling. If stress shielding occurs, the decreased loading on the bone causes a decrease in density in the affected regions. If the bone density decreases significantly, the fixation of the implant can be jeopardised and loosening and ultimately failure of the prosthesis may occur. It is therefore necessary, for the design of successful implants, to understand the loading environment to promote bone growth in the correct areas. Computational models, such as those based on the finite element method, can serve as valuable predictive tools in the field of orthopaedics. New implant designs and the outcome of surgical procedures can be predicted with the finite element model. In order to act as a predictive tool, the numerical model has to be validated and calibrated to the problem at hand.

The aim of this project is to develop a finite element model to predict the density evolution in the scapula post reverse shoulder arthroplasty. Several mathematical and computational models have been developed for bone remodelling. In these models, bone is generally modelled as a porous, solid structure. Because the remodelling response of bone is optimal to the loading environment, the density evolution is generally based on an optimisation approach. The difference between a mechanical stimulus, which may be a stress, strain or strain-energy density, and an attractor state, which is the optimal state the bone is driving towards, drives the density evolution.

This work is part of a larger project with collaborators in the Division of Biomedical Engineering and the Department of Orthopaedics at the University of Cape Town (UCT), where researches are working on the different design aspects of the reverse shoulder prosthesis. Further our collaborators have worked with Andreas Kontaxis at the Leon Root Motion Analysis Laboratory in the Hospital for Special Surgery in New York City to develop a biomechanical model of the upper limb. A robust finite element model would extend this work, as the effectiveness of the designs can be evaluated with the finite element code serving as a predictive tool.

The physical process of remodelling is modelled here using continuum scale, open system thermodynamics whereby the density of bone evolves isotropically in response to the loading it experiences. The fully-nonlinear continuum theory is solved approximately using the finite element method. The author is only aware of seven works on bone remodelling studies in the scapula (see Campoli et al. (2014, 2013); Quental et al. (2012, 2014b); Sharma et al. (2009, 2010); Sharma and Robertson (2013)), where different remodelling theories were adopted.

The aim of this project is to develop a reliable finite element code, which predicts the density distribution due to remodelling in the bone for a given loading environment. The objectives are to implement

the remodelling theory developed by Kuhl and Steinmann (2003) using the finite element method and to validate and test the code against various benchmark problems and finally, to apply the validated code to the intact scapula and to the scapula post reverse total shoulder arthroplasty. The issue of stress shielding can be predicted and some initial guidance to improve the surgical procedure may be offered.

The dissertation is organised as follows. The microstructure of bone and the remodelling mechanism is detailed in Chapter 2. Different remodelling theories, which have been developed over the past 40 years, are also detailed. The literature on the material properties of bone in the scapula region and previous computational remodelling work on the scapula is discussed. This is followed by a description of the anatomical shoulder and the reverse shoulder procedure in Chapter 3. The complications following the reverse procedure and the experimental and computational work done on the reverse shoulder is detailed. The continuum formulation of bone is then introduced in Chapter 4, where the basics of closed system thermodynamics are detailed, followed by the open system relations and the constitutive relations for bone remodelling. The theory is implemented with the finite element method, which is presented in Chapter 5, followed by the code validation in Chapter 6, where various benchmark problems from the literature have been implemented and the different aspects of the code investigated. The validated code is applied to the scapula pre and post procedure. Here, the ASTM F2028 (ASTM, 2015) problem of the glenoid component implanted into a polyurethane foam block bone substitute is investigated, followed by the remodelling response in the intact scapula and the scapula post procedure. Finally, the numerical model is discussed and conclusions are drawn in Chapter 8.

2

Bone as a material

Bone is a complex living tissue. It consists of a solid matrix and a fluid phase. The characteristic response of bone is primarily due to the solid phase at low strain rates. Bone can further be classified as very dense cortical bone or spongy trabecular bone. Remodelling is governed by various cells in the matrix phase, which deposit minenerals onto (osteoblastic action) or remove (osteoclastic action) minerals from the bone, resulting in density changes.

Bone is generally modelled as a porous, solid structure. The remodelling response can be viewed from the perspective of optimisation theory whereby a function describing the change in internal energy required to adapt the bone to the external loading is minimised. The result is a density evolution driven by the difference between a mechanical stimulus, which may be a stress, strain or strain-energy density, and an attractor state, which is the optimal state for bone is driving towards.

The material properties of bone, essential inputs for accurate mathematical or computational models, are difficult to obtain. The material properties differ, depending on the type of bone and the anatomical site. Even if the same bone types are tested, a large amount of scatter in the data is present. Nonetheless, relationships between the density and material properties of bone have been established. However, the material properties of the scapula, the area of interest in this project, are not well known. The material properties of the glenoid have been experimentally investigated, however, a large amount of scatter exists. The author is only aware of seven works, where bone remodelling studies in the scapula are reported. In general, relationships between the density and the material properties are reported for different bones, such as the femur.

2.1 The structure of bone

Bone provides protection for the organs in the body and the attachment points for ligaments and tendons. The skeletal system is the weight bearing support structure against gravity and other loading.

It is well known that bone adapts to its loading environment. The German orthopaedic surgeon Julius Wolff first postulated a law describing the relationship between the mechanical loading environment and the corresponding adaptive behaviour observed in bone in 1892, called *the law of transformation of the bone* (Wolff, 1892). His work laid the foundation of modern medicine in the field of orthopaedics. Wolff's law states that the strut-like structures in bone, called the trabeculae, reorientate along the directions of the principle stresses caused by the loading environment. Simultaneously, the bone density changes due to the internal remodelling process in response to the different loading conditions (Taber, 1995). This phenomenon is evident in Figure 2.1 from Taylor et al. (2009) where the left and right humerus of a professional tennis player is depicted. It is very clear from these x-ray images that the dominant right arm of the tennis player, which experiences more severe loading than the weaker left arm, is much denser. Taylor et al. successfully simulated the final density distribution using the finite element method.

Another example is that, to counter the affects of remodelling, astronauts in space have to exercise regularly and can only spend a limited amount of time in the micro-gravitational environment to avoid drastic bone resorption (Ohshima, 2012).

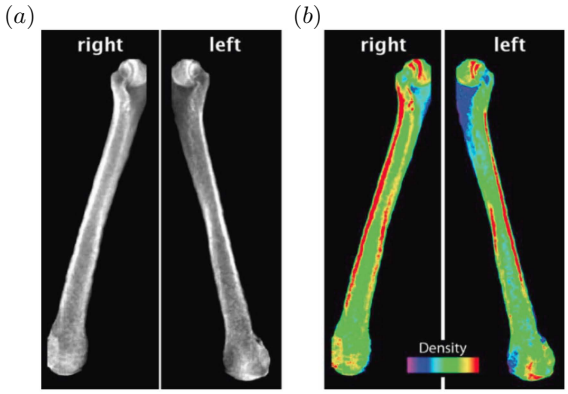

Fig. 2.1: (a) X-ray image and (b) simulated density distribution in the right and left humerus of a professional tennis player (Taylor et al., 2009).

Bone adaptation can be categorised into remodelling, growth and morphogenesis (Cowin, 2004; Taber, 1995). All three phenomena may occur simultaneously. Remodelling refers to the changes in material properties of a tissue.These are changes in density and internal structure, which in turn alter the strength and stiffness. Morphogenesis usually refers to embryonic development, as well as to wound healing and organ regeneration.Finally, growth refers to the net change in volume of a tissue.

An appreciation of the microstructure and constituents of bone is required to understand the remodelling process. Most bones in the human body consist of a thin, compact outer layer and a porous interior structure as shown in Figure 2.2. The porous structure is generally also found in the vicinity of joints (Cowin and Hegedus, 1976). The compact component is called cortical bone and the porous interior is called trabecular, spongy or cancellous bone and consists of the strut-like trabeculae. Gibson and Ashby (1999) and Carter and Hayes (1977) reported that the material properties of both types of bone fall within a similar range. Further, Gibson and Ashby (1999) and Cowin and Hegedus (1976) report that cancellous bone can be viewed as a cellular solid. The porosity of cortical bone falls within a range of 5 % - 30 %, whereas the porosity of cancellous varies between 30 % to over 90 % (Carter and Hayes, 1977).

As mentioned, bone consists of a solid matrix and a fluid phase. The solid component mainly consists of type I collagen onto which dahlite (hydroxyapatite) crystals form (Weiner and Wagner, 1998). These mineralised collagen fibrils are arranged in bundles and arrays to form lamellar bone, the orientations of which depend on the loading. The fibrils are arranged in such a way that they are capable of withstanding stresses in multiple directions, as stated in Wolff's law.

Cortical bone consists of densely packed osteons, also called Haversian systems. The osteons consist of lamellar bone, which is folded into cylinders (Weiner and Wagner, 1998). The cylinders have a diameter of ≈ 150 μm and a length of $1 - 2$ cm (Cowin and Hegedus, 1976). Three types of cells are active in this system. Osteoclasts remove material through excavation of tunnels and channels in the Harvesian system. Osteoblasts then deposit material on the walls of the cavities created by osteoclasts. Osteoblasts, which are trapped in the solid matrix are transformed to osteocytes. Osteocytes are cells responsible for bone maintenance and govern the remodelling process of osteoclastic and -blastic activities (Weiner and Wagner, 1998). The narrow channels and capillary-like features in the Harvesian system are termed Haversian and Volkmann's channels, which allow for blood flow (Keaveny and Hayes, 1993). The constituents of bone are shown in Figure 2.3.

The trabeculae in cancellous bone consist of lamellae and are surrounded by bone marrow and small blood vessels, which function as the blood supply (Cowin and Hegedus, 1976; Singh, 2012). A detailed

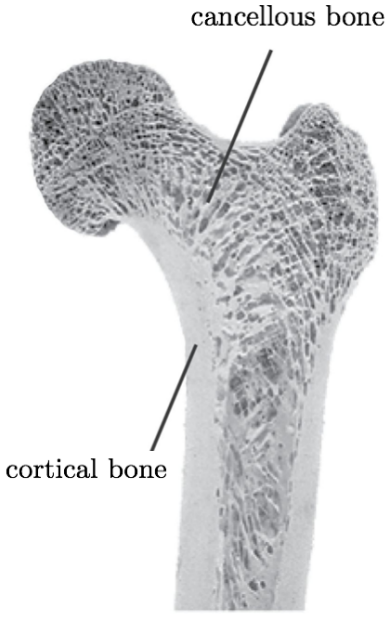

Fig. 2.2: A cross-section of the human femur showing the dense cortical outside layer and the cancellous bone in the interior (Willems et al., 2014).

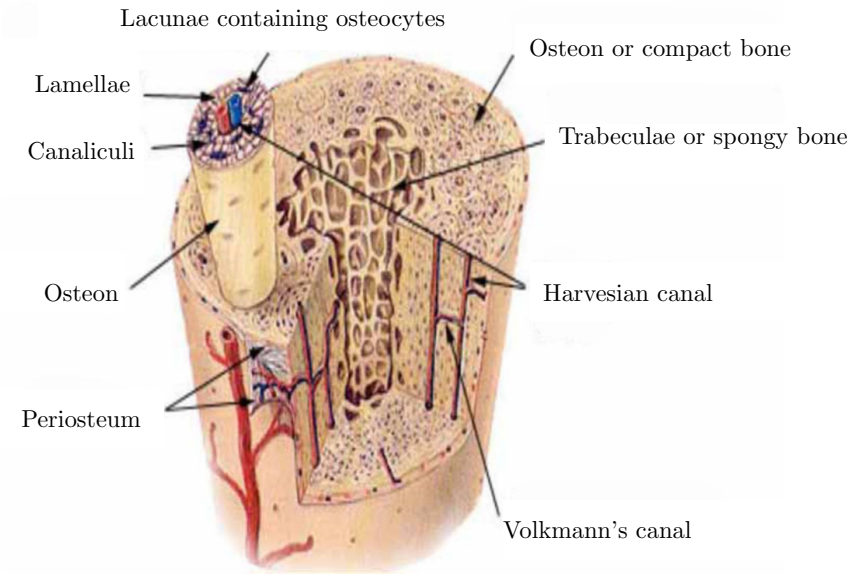

Fig. 2.3: The constituents of bone, taken from Cowin and Cardoso (2015). Lacunae are small cavities in the bone, canaliculi are microscopic canals and periosteum are vascular connective tissue.

view of the trabeculae of cancellous bone is shown in Figure 2.4. The orientation of the trabeculae corresponding to the loading environment is also evident in the cross-sectional view of the femur in Figure 2.2. Osteoblasts, -clasts and -cytes are also present in the trabeculae and are responsible for remodelling (Singh, 2012). The deposition and mineralisation of nutrients on the trabeculae from the osteoblasts, result in density changes in the bone.

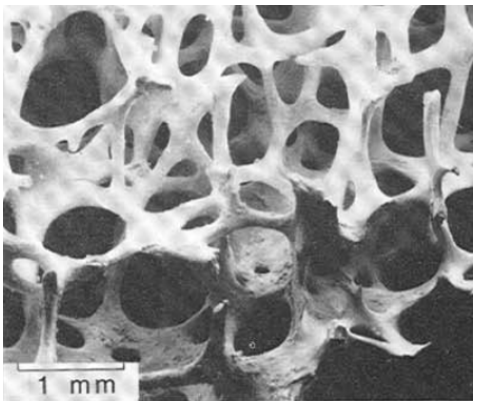

Fig. 2.4: An image showing the trabeculae of cancellous bone, taken from Gibson (2005).

It is still unclear what the trigger mechanism is which stimulates the remodelling process (Taber, 1995). Furthermore, the adaptive behaviour of bone may not solely be regulated by the loading environment, but also by the genetics of the individual (Cowin, 2004). Nevertheless, the theory that remodelling is captured by the loading environment alone is well established and useful. Several trigger mechanisms have been proposed in literature, including a piezoelectric effect, microdamage, extracellular fluid pressure, that the shear stress of the flowing fluid may be sensed by the cells, or the direct loads on the cells, to name a few (Cowin, 1999; Taber, 1995).

Similarly, the relation between the mechanical properties and the apparent density and the strain rate is still unclear (Helgason et al., 2008). Carter and Hayes (1977) conducted compression tests of human and bovine trabecular bone. 100 cylindrical specimens of the human tibia and 24 specimens of the bovine femur were used. The specimens were loaded in uni-axial compression at various strain rates. The tests of the human specimens were conducted with and without the bone marrow. Carter and Hayes concluded that the viscous flow of the marrow had no effect on the bone at strain rates of 0.001 s^{-1}, 0.01 s^{-1}, 0.1 s^{-1} and 1.0 s^{-1}. Hence viscous effects do not affect the material properties at the low strain rates experienced during everyday activities such as walking. Furthermore, they found that the strain rate has a far less significant influence on the compressive strength than the density. Carter and Hayes assumed a power law relation between the material properties and the density. The power law relations between relative density, and Young's modulus and the compressive strength was observed. The results for the compressive strength are shown in Figure 2.5. The compressive strength corresponds to the maximum compressive load the bone can withstand before it fractures.

Carter and Hayes (1977) determined the relationships for the compressive strength σ_{comp} and Young's modulus E as:

$$\sigma_{\text{comp}} = \sigma_c \dot{\epsilon}^{0.06} \left(\frac{\rho}{\rho_c}\right)^2 \qquad \text{and similarly} \qquad E = E_c \dot{\epsilon}^{0.06} \left(\frac{\rho}{\rho_c}\right)^3,$$

where $\dot{\epsilon}$ the total time derivative of the strain ϵ, i.e. the strain rate, and ρ the apparent density. The apparent density is the total mass per total volume of the porous bone. The subscript c indicates the counterpart of the property for cortical bone.

Gibson (2005) summarised the results of various compression test studies on the human tibia and femur and found a quadratic relationship between the compressive strength and the density, as well as between the Young's modulus and the density. Gibson (2005) and Carter and Hayes (1977) both

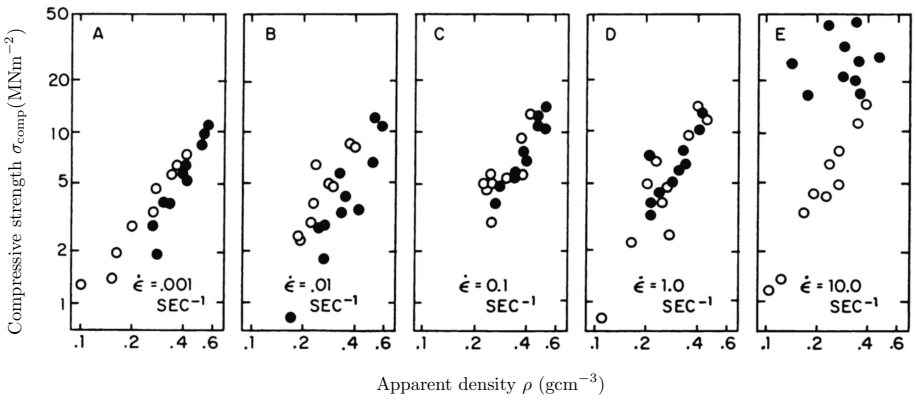

Fig. 2.5: The experimental results from Carter and Hayes (1977) showing the plots of compressive strength versus the apparent density at different strain rates.

report a fair amount of scatter in the data, which may explain the discrepancy between the cubic (Carter and Hayes, 1977) and quadratic (Gibson, 2005) relation for the Young's modulus. The scatter can be explained by the different trabecular architectures in each test specimen (Gibson, 2005). Gibson reports that the quadratic relation indicates that bending is the dominant failure mode during linear elastic deformation in cancellous bone in accordance with the theory of cellular solids. With the analyses of micro-CT scans and finite element simulations, Gibson proved that this is indeed the case for trabecular bone.

Morgan et al. (2003) conducted uniaxial tension and compression tests on bone for a range of anatomical sites. Samples from the vertebra, the proximal tibia, the greater trochanter and the femoral neck were analysed. The resulting relationship between the Young's moduli and the density are shown in Figure 2.6. Morgan et al. used a power law for the relation between the mechanical properties and the density of the form

$$E = A\rho^B \,.$$

Parameters A and B are fitted for each bone type and vary between 4730 and 15520 MPa [g cm^{-3}]$^{-B}$, and 1.49 and 2.18, respectively. Morgan et al. show that the anatomical origin of the bone has a vital influence on the material properties.

Helgason et al. (2008) conducted a review of 26 studies on the relations between the bone density and material properties, focusing on human bone. Different testing techniques, loading directions, specimen sizes, geometries, and anatomic sites are some of the variables reported. Large scatter is present among the data, even after normalisation. Therefore, it is essential to carefully choose the elasticity-density or strength-density relationships for a mathematical or computational model. It is important to choose the relationship which is most closely related to the anatomical region and bone type in question. Also, the experimental technique has to be scrutinised before a relationship is adopted. Some techniques for instance underestimate the stiffness of the bone (Helgason et al., 2008).

Even though no standardised material relations for bone at the anatomical sites are available, various power law relations reported in literature are adopted in finite element analyses. Subject-specific models have become prevalent in literature (see Schileo et al., 2007). The general procedure is to use the subject specific CT-scans and interpolate the density distribution using the Hounsfield unit. The Hounsfield unit is known for water, air, compact bone and fat and a linear interpolation is used to determine the density values for bone in a CT image (Luijkx and Nadrljanski, 2016). A power law is then used to assign the material properties to the subject-specific model.

Understanding and predicting the material properties, as well as the adaptive nature of bone is important when designing medical implants. Implants alter the load distribution in the bone. This can result in stress shielding, where the implant carries the majority of the load, resulting in regions of unloaded bone, which induces remodelling and leads to potentially devastating consequences for the

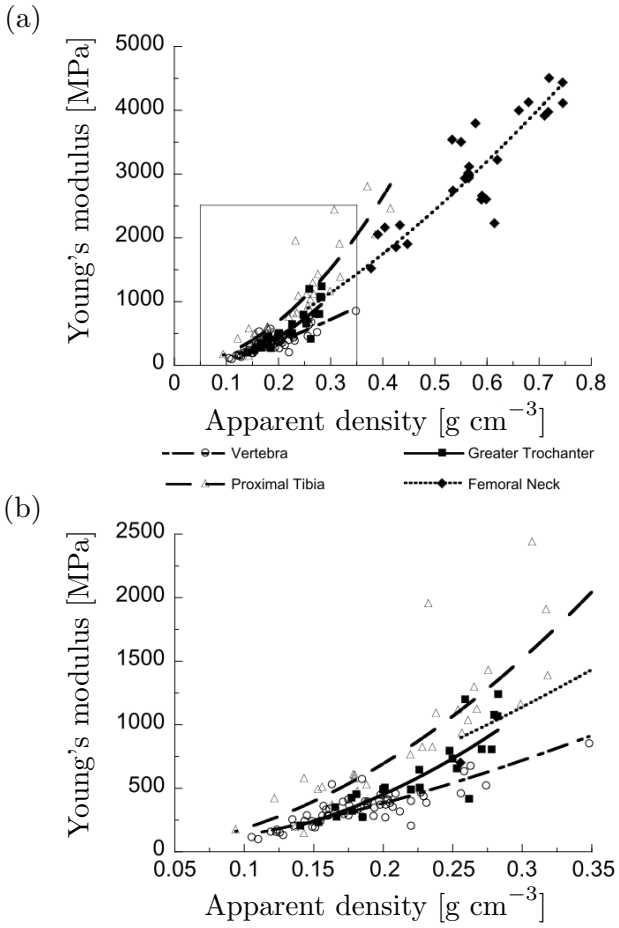

Fig. 2.6: The experimental results from Morgan et al. (2003) showing Young's modulus - density relations. (a) shows the entire range of the results and (b) is zoomed into the region shown in (a).

patient (Schmidutz et al., 2014). A model, which can predict the stress distribution in the bone and the resulting remodelling, is therefore a valuable tool for the design of new prostheses.

2.2 Bone remodelling theories

Various theories for bone remodelling are reported in literature. One of the earliest theories is an open system thermodynamics approach by Cowin and Hegedus (1976), named the theory of adaptive elasticity, which is based on the theory of poroelasticity. The Cowin and Hegedus model is derived from that of a porous elastic solid, filled with fluid. Only the solid component is modelled, as the properties of bone are captured by the solid constituents at small strain rates. The fluid phase is accounted for by the reactions in the open system relations. Remodelling is assumed to take place due to a strain-controlled chemical reaction, where mass, momentum, entropy and energy are transferred to and from the solid. The balance relations are therefore the standard closed system thermodynamics balance relations with added contributions due to the mass transfer and interactions between the solid and fluid phase. The fluid is assumed to be an isothermal heat reservoir, as the heat generated in the chemical reactions is very quickly removed by the blood circulation. Several further assumptions concerning the balance of momentum are made. The force between the fluid and solid phase is assumed to be negligible compared to the magnitudes of the external loads. Inertia effects are also neglected, as the characteristic time of remodelling is far greater than the time for stress wave propagation.

The balance of mass in the Cowin and Hegedus theory is governed by the evolution of the bulk density, which depends on the solid material density and the volume fraction. Cowin and Hegedus present the constitutive relations, where the volume fraction in a reference state is introduced as the primary variable in the balance of mass formulation. In summary, their model captures the mechanical properties of bone by modelling it as a porous solid using the theory of open system thermodynamics.

Other mathematical models for bone remodelling are based on optimisation theory with an objective function which captures the adaptive behaviour of bone (see Carter et al. (1987); Harrigan et al. (1996); Jacobs et al. (1997); Weinans et al. (1992)). Some of these theories are based on continuum damage mechanics (see Carter et al. (1987); Jacobs et al. (1997)). The general concept behind the optimisation theories is captured in a density evolution relation of the form:

$$\frac{\partial \rho}{\partial t} = B(S - \Psi_0^*)\,, \qquad \text{with} \qquad 0 < \rho \leq \rho_c\,,$$

where B is a constant, ρ_c is the density of cortical bone, Ψ_0^* is a reference stimulus, which the system is driving towards, and S is the mechanical stimulus, which may take the form of an effective stress, strain, or strain energy density (see Weinans et al. (1992), Jacobs et al. (1997), Carter et al. (1987)). The reference stimulus may be site or non-site specific and is the state where the bone density does not change as it is loaded in an equilibrium condition, the so-called homeostatic condition (Carter et al., 1987; Weinans et al., 1992). Material anisotropy may be introduced in the elasticity tensor as detailed by Jacobs et al. (1997), for example.

Weinans et al. (1992) introduced the accumulated strain energy density U_a as the mechanical stimulus of the form

$$S = \frac{U_a}{\rho} \qquad \text{where} \qquad U_a := \frac{1}{n}\sum_{i=1}^{n} \frac{U_i}{n_i}\,,$$

where U_i is the value of a strain-energy function at load condition i and n is the number of loading conditions. Constitutive parameters such as E are then assumed to be a function of the density (e.g. a power law relation is employed). Harrigan et al. (1996) introduced a modification to the relations reported by Weinans et al. given by

$$S \equiv \frac{U}{\rho^m} \qquad \text{and} \qquad E \equiv E_0 \rho^n\,,$$

where $n, m > 0$ are model parameters. The factor n is chosen from the power law relations and is typically 2. The factor m is introduced to ensure numerically stability. Harrigan (1994) showed that stability is guaranteed, if $m > n > 0$.

The bone remodelling theory developed by Kuhl and Steinmann (2003) is based on the theory of poroelasticity and open system thermodynamics and makes use of the constitutive relations developed by Harrigan et al. (1996) That theory is used in this project and is detailed in Chapter 4. The general

theory of the model is based on that by Cowin and Hegedus (1976). However, the balance of mass is formulated differently. A mass source term is introduced, which is derived from the optimisation function reported by Harrigan et al. (1996). Furthermore, a mass flux contribution is introduced and the constitutive relations for the free energy and stress differ significantly.

The model by Kuhl and Steinmann is isotropic, which of course is not accurate as bone, especially the cancellous bone, is anisotropic due to the trabecular architecture. However, predicting regions of high and low stresses and densities is a valuable tool in orthopaedics. Bone remodelling predictions have, for example, revolutionised the design of a hip prosthesis by changing the prosthesis from a long stem to a small peg, which ensures secure implant fixation (Ambrosi et al., 2011). The predicted density distributions by Ambrosi et al. (2011) are shown in Figure 2.7 for the intact femur, the traditional prosthesis design and the new design.

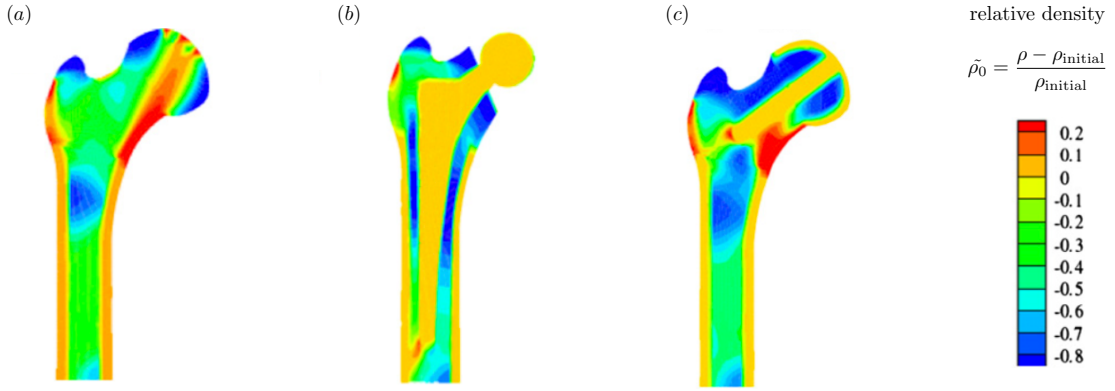

Fig. 2.7: Results from Ambrosi et al. (2011) showing the relative density distribution of (a) the proximal femur, (b) the proximal femur with a traditional hip prosthesis and (c) the proximal femur with a novel prosthesis, which improved the fixation and eliminated stress shielding.

Waffenschmidt et al. (2012) proposed an extension of Kuhl and Steinmann (2003) model to include anisotropy. An extension of the Kuhl and Steinmann theory to account for anisotropy will be discussed in the concluding chapter. It is critical, however, to have a robust isotropic model prior to considering such extensions. This is one objective of the current presentation.

2.3 The scapula

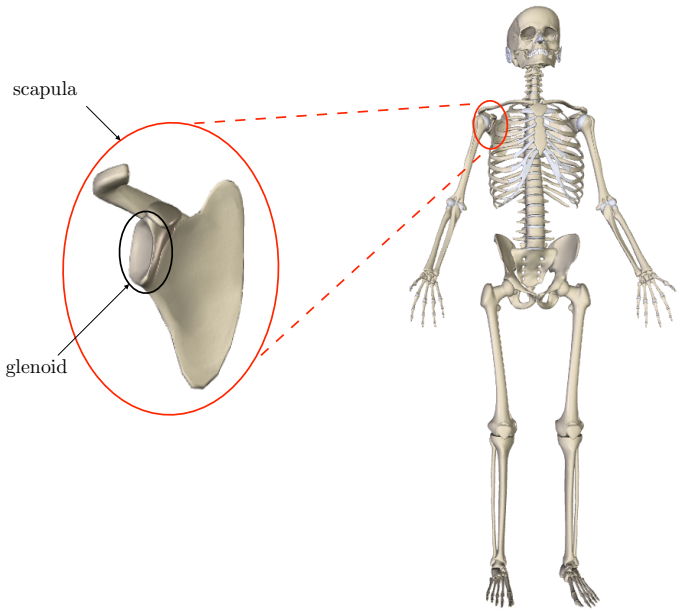

Fig. 2.8: The bones of the human skeleton, focussing on the scapula and glenoid (BioDigitalHuman, 2015).

The scapula, also known as the shoulder blade, is shown in Figure 2.8. It is a flat bone in the human body, which consists of mainly cancellous bone (Currey, 1984). The only experimental studies of the bone in the scapula, which the author is aware of, are of the material properties of the cancellous glenoid bone. The results of these studies show that the cancellous bone in the glenoid exhibits highly anisotropic material properties (Frich et al., 1997; Kalouche et al., 2010; Mansat et al., 1998). Kalouche et al. (2010) and Mansat et al. (1998) report that the anisotropy may be the result of the non weight-bearing characteristic of the scapula. The joint contact force on the glenoid is at its maximum about one body weight, whereas the force on the hip is approximately six body weights and on the knee 2 to 4 body weights (Mansat et al., 1998). Different experimental studies of the glenoid bone are reported in literature (see Anglin et al. (1999), Anglin et al. (1984), Frich et al. (1997), Kalouche et al. (2010), Mimar et al. (2008) and Mansat et al. (1998)). The studies include indentation tests of the intact glenoid or cubic glenoid specimens. Uni-axial compression tests on cylindrical or cubic glenoid test specimens are also frequently reported. Ultrasonic measurements of cubic glenoid specimens are also detailed in literature. The results of some of the studies reported in literature are summarised in Table 2.1. The author is not aware of any proposed relations between the mechanical properties and the density.

Property-density relations reported for the femur or tibia have been used in finite element analyses of the scapula (see e.g. Büchler et al., 2002; Campoli et al., 2014; Gupta et al., 2004; Pomwenger et al., 2015; Sharma and Robertson, 2013). Some studies such as Denard et al. (2016) simply use the material properties of a polyurethane foam block, as the material properties are reported to be comparable to cancellous bone. A summary of the material properties used in finite element simulations of the scapula is given in Table 2.2.

Most of the finite element simulations of the scapula only analyse the stress distribution and do not consider bone remodelling. The author is only aware of seven reports on bone remodelling in the scapula.

Table 2.1: A summary of the experimental results of the material properties of cancellous bone reported in literature. ρ_{app} is the apparent bone density.

Source	Method	Properties
Anglin et al. (1984)	indentation test of the intact glenoid	E = 119 - 234 MPa
Anglin et al. (1999)	indentation test of the intact glenoid of 10 cadavar test specimens	E = 67 - 171 MPa large scatter among test specimens
Mimar et al. (2008)	indentation test of intact glenoid	E = 119 - 234 MPa
Frich et al. (1997)	indentation and compression tests cylindrical and cubic specimens	E = 100 - 400 MPa, $\nu = 0.263$, $\rho_{\text{app}} = 0.35\ \text{g}\,\text{cm}^{-3}$
Kalouche et al. (2010)	uni-axial compression tests 82 cubic specimens of 11 scapulae	$E_1 = 204$ MPa , $E_2 = 113.5$ MPa, $E_3 = 102.1$ MPa, $\rho_{\text{app}} = 0.29\ \text{g}\,\text{cm}^{-3}$
Mansat et al. (1998)	ultrasonic measurements 74 x 6 mm specimens of 6 cadavers	$E_1 = 372 \pm 164$ MPa , $E_2 = 222 \pm 79$ MPa , $E_3 = 198 \pm 75$ MPa

Sharma and Robertson (2013) reports on bone remodelling in the scapula. The geometry of the scapula was obtained from CT-scans of a cadaver. The density distribution in the scapula was determined using an interpolation of the Hounsfield number from the CT scan. A finite element simulation was then conducted to validate the computational model. An initial uniform density distribution of $\rho_0^* = 0.6\ \text{g}\,\text{cm}^{-3}$ was assumed. An isotropic remodelling theory, with a strain-energy based reference stimulus was used, following the approach taken by Jacobs et al. (1997). The bone was modelled as a linear elastic material. The minimum and maximum density values were set to $\rho_{\text{min}} = 0.001\text{g}\,\text{cm}^{-3}$ and $\rho_{\text{max}} = 1.8\text{g}\,\text{cm}^{-3}$. The boundary conditions for the muscle and joint loads were taken from literature. Sharma and Robertson simulation set up is shown in Figure 2.9.

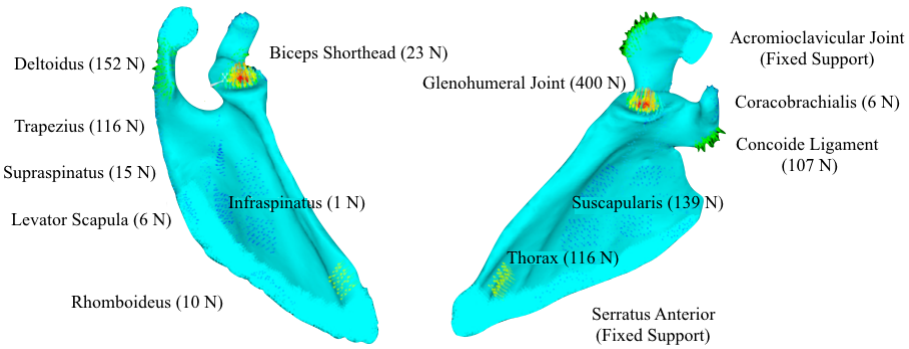

Fig. 2.9: The boundary conditions and geometry used by Sharma and Robertson (2013).

The density distributions determined and predicted by Sharma and Robertson (2013) are shown in Figure 2.10. The predicted density magnitudes over- and underestimate the actual density values in the scapula. The loading conditions were also taken from literature and are not specific to the

Table 2.2: A summary for the material properties used for the scapula in finite element simulations reported in literature. E is the Young's modulus, E_0 is the Young's modulus of the solid constituent, ρ_c is the density of cortical bone, ρ_0^* is the initial uniform density distribution.

author	bone type and source	material properties
Sharma and Robertson (2013), Büchler et al. (2002)	cancellous bone three studies	$E = E_0 \left(\frac{\rho}{\rho_c}\right)^2$, $E_0 = 15$ GPa $\rho_c = 1.8\mathrm{g\,cm^{-3}}$ $\nu = 0.3$ $\rho_0^* = 0.6\mathrm{g\,cm^{-3}}$
Quental et al. (2012)	-	$E = 17$ GPa , $\nu = 0.3$
Campoli et al. (2013), Campoli et al. (2014)	pooled: Morgan et al. (2003) vertebra, proximal tibia, greater trochanter, femoral neck	$E = a\rho^b$, a = 6850, b = 1.49, $\nu = 0.3$
Stone et al. (1999)	-	cortical: E = 8 GPa, $\nu = 0.35$ cancellous:E = 0.4 GPa, $\nu = 0.21$
Yongpravat et al. (2013)	femur Schileo et al. (2007)	cortical: E = 2705 MPa, $\nu = 0.3$ cancellous: E = 574 MPa , $\nu = 0.3$
Denard et al. (2016)	PU foam block ASTM	E = 0.553 GPa, $\nu = 0.3$, $\rho_0^* = 481\mathrm{kg\,m^{-3}}$
Gupta et al. (2004), Pomwenger et al. (2015)	cortical and cancellous bone Gibson (1985)	cortical: $E = 17500$ MPa, power relations for cancellous bone: $E = 1 - 128$ MPa for $\rho < 350\mathrm{kg\,m^{-3}}$, $E = 128 - 17500$ MPa for $350\mathrm{kg\,m^{-3}} \leq \rho \leq 1800\mathrm{kg\,m^{-3}}$, $\nu = 0.3$

scapula. However, this analysis shows that there is potential for finite element models to capture the remodelling response of the scapula. Sharma et al. (2009, 2010) reported in earlier studies on two-dimensional simulations of the bone remodelling in intact scapula and considered a prosthesis in the conventional total shoulder procedure using the same remodelling theory.

Campoli et al. (2013) conducted a similar three-dimensional finite element analysis of bone remodelling in the scapula as reported by Sharma and Robertson (2013). A cadaveric scapula was CT-scanned and the density distribution interpolated from the grey scale data. An optimisation-based density evolution algorithm (Weinans et al., 1992) was used with the strain as the mechanical stimulus. An initial uniform density distribution of $\rho_0^* = 0.8\mathrm{g\,cm^{-3}}$ was assigned to the scapula. The muscle loads were determined from the Delft Shoulder and Elbow Model (SimTK, 2016) for abduction and flexion, as these two movements are performed frequently on a daily basis. Campoli et al. reported errors between the measured and predicted density to be approximately 30 %. Campoli et al. (2014) further reported on an uncertainty study of the parameters used in the subject specific scapula model and concluded that some parameters have an uncertainty of up to 30 %. It is therefore important to develop subject specific models as accurately as possible, using the most realistic geometries, boundary conditions and material parameters.

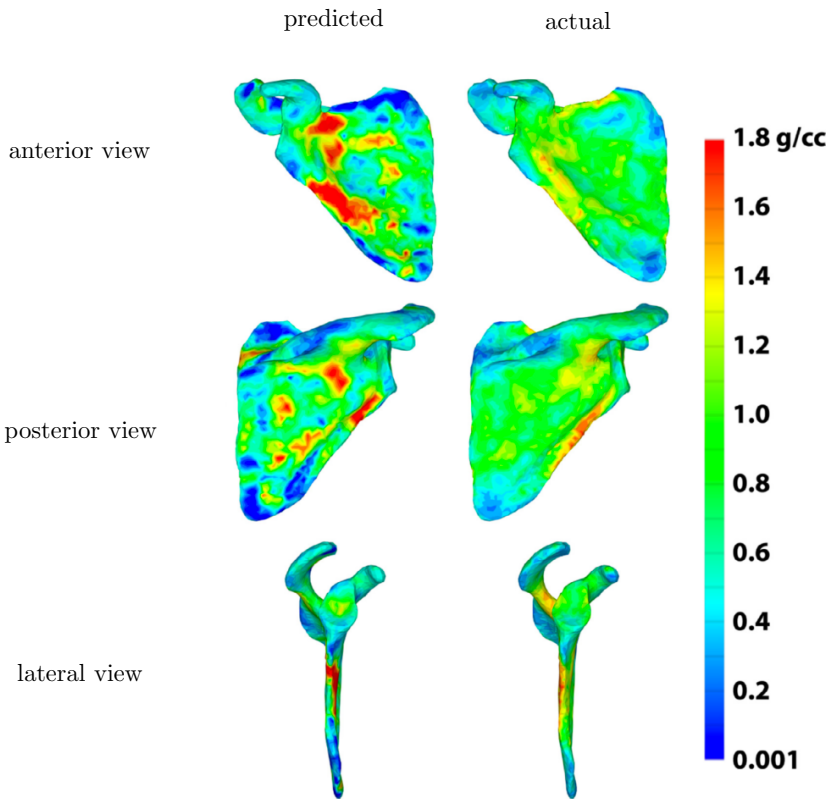

Fig. 2.10: The density distributions in the subject specific scapula determined and predicted by Sharma and Robertson (2013).

Quental et al. (2012) developed a three-dimensional subject specific finite element model of bone remodelling in the scapula. The bone was modelled as a linear elastic orthotropic, porous material following the theory by Fernandes et al. (1999) (see also Folgado et al. (2009)). An optimisation theory is adopted, with a strain-based mechanical stimulus. The bone micro-structure is modelled as a periodic structure, with repeated unit cells with prismatic holes, accounting for the porosity (Folgado et al., 2009). The density depends on the solid volume fraction of the cells. The cells align according to the loading environment and only a single load case can be considered at a time. Bone material properties are obtained through homogenisation and the initial uniform density distribution was taken as $\rho_0^* = 0.4\ \mathrm{g\,cm^{-3}}$. The loading conditions were taken from a biomechanical model (Quental et al., 2012). The influence of various parameters in the theory were then analysed. Quental et al. reported that when the resulting densities at only 89 % of the nodes are considered, the absolute error lies below 33 %.

The results of the three studies reported in literature are all encouraging and support the development of a robust, reliable bone remodelling model for the scapula as detailed in the rest of this presentation.

3

Reverse total shoulder arthroplasty

Reverse total shoulder arthroplasty is a surgical technique to restore the functionality and integrity of a rotator cuff deficient shoulder. In this chapter, the anatomical shoulder is first described - for additional detail see Calais-Germain (2007); Drake et al. (2010). The reverse total shoulder procedure and the related complications are described next, followed by a review of experimental and computational approaches to analyse the procedure.

3.1 The anatomical shoulder

The shoulder is the region where the arm connects to the body. It consists of three bones, namely the scapula, the clavicle and the humerus, as illustrated in Figure 3.1. The scapula is a mobile bone and the shoulder joint is the most dynamic in the human body (Hitzmann, 2004). The primary joint and the one of interest in the context of a reverse shoulder, is the connection of the scapula and the humerus. The surface area of the head of the humerus is two to three times larger than the surface area of the shallow glenoid cavity in the scapula (Calais-Germain, 2007). This ball-and-socket type joint is called the glenohumeral joint.

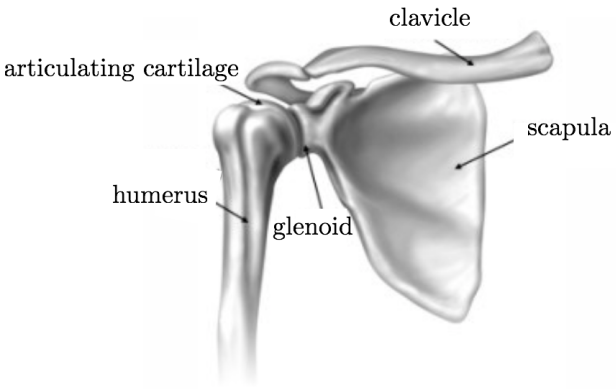

Fig. 3.1: The bones of the shoulder (AAOS, 2011).

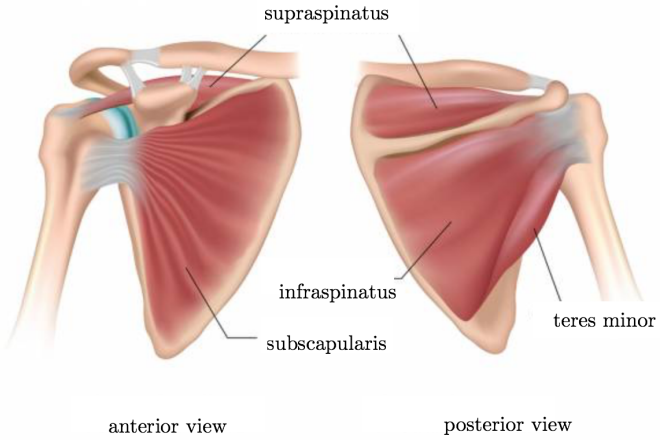

Fig. 3.2: An illustration of the four rotator cuff muscles stabilising the glenohumeral joint (Stotts, 2015).

The glenohumeral joint is encased by a capsule, which is reinforced by ligaments. This capsular joint is not very strong. The stabilisation is provided by the four rotator cuff muscles connecting the humerus and the scapula. The rotator cuff muscles are illustrated in Figure 3.2.

A total of 18 muscles connect to the shoulder. A further muscle of interest for the reverse shoulder procedure, is the deltoid muscle shown in Figure 3.3. The deltoid muscle is partly responsible for the characteristic shape of the shoulder. The deltoid connects the scapula and clavicle to the humerus. The function of the deltoid is to provide the necessary force for full abduction.

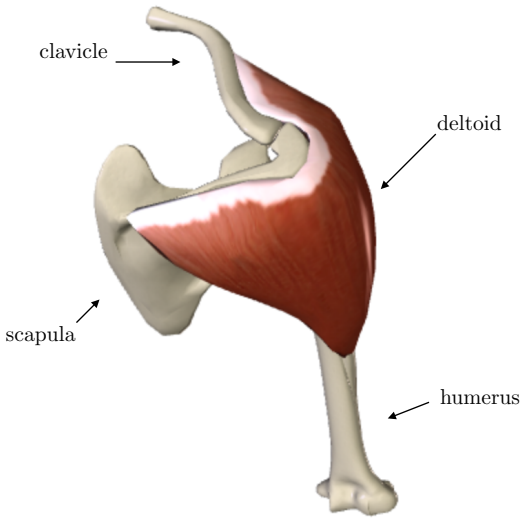

Fig. 3.3: The deltoid muscle, connecting the scapula and clavicle to the humerus (BioDigitalHuman, 2015).

3.2 The surgical procedure

As discussed in section 3.1, the rotator cuff muscles and the deltoid play a major role in the reverse shoulder procedure. Patients with rotator cuff deficient shoulders were previously treated using a standard anatomical total shoulder replacement (Hsu et al., 2011). However, this procedure did not alleviate pain or restore functionality to the shoulder. The reason for these shortcomings is that the rotator cuff muscles no longer stabilise the glenohumeral joint and as a result the force provided by the deltoid is unopposed. Consequently, the humeral head is placed superiorly (upwards), rather than medially (towards the center of the body) during abduction. This causes pain for the patient, who will soon be unable to perform this action due to pseudo-paralysis. For additional details see Hsu et al. (2011).

In 1985, the orthopaedic surgeon Paul Grammont proposed the concept of a reverse shoulder procedure to treat patients with rotator cuff deficient shoulders (Boileau et al., 2005). The anatomical glenohumeral joint is reversed, as shown in Figure 3.4. With this procedure it is possible to restore the integrity and stability of the glenohumeral joint. The humeral head is removed and replaced with a polyethylene humeral cup. A stem is placed in the central channel of the humerus and the cup is press-fitted in the top of the humeral stem. A hemispherical implant, termed the glenosphere, is screwed into the scapula. The center of rotation is now located medially compared to the anatomical shoulder. As a result, the force applied by the deltoid muscle is also directed medially. The deltoid therefore compensates for the absent rotator cuff muscles, providing stability, improved range of motion and pain relief (Boileau et al., 2005).

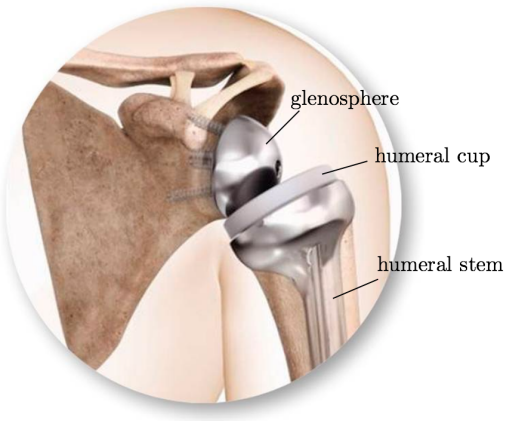

Fig. 3.4: An illustration of the reverse shoulder (DePuySynthes, 2016).

3.3 Complications

As ingenious as the concept of the reverse shoulder is, many complications, up to 75 % in some clinical series (Hsu et al., 2011), have been reported following the procedure. The most common complication is scapular notching (see Boileau et al. (2005), Virani et al. (2008), Hsu et al. (2011), Gutiérrez et al. (2011) and Berliner et al. (2015)). At full adduction, the humeral cup impinges on the inferior border of the scapula. The impingement causes bone resorption in the affected regions. Further, the polyethylene debris cause infection and osteolysis (Boileau et al., 2005). Collaborators in the Department of Orthopaedics at the University of Cape Town (UCT) also hypothesize that the change in the stress distribution in the scapula may cause atrophy in the inferior region.

To mitigate scapular notching, a lateralised center of rotation has been proposed (see Boileau et al. (2005), Hsu et al. (2011), Virani et al. (2008), Berliner et al. (2015)). The medialised and lateralised configurations are shown in Figure 3.5. The lateralised center of rotation mitigates scapular notching and also improves external rotation post procedure. However, a resultant force, which acts superiorly is introduced (Berliner et al., 2015). This induces a moment at the bone-baseplate interface, which in turn creates new complications. These include baseplate loosening and glenosphere unscrewing (Berliner et al., 2015).

The design of the reverse shoulder prosthesis is highly intricate. Several additional design factors are evaluated in the literature. These include the glenosphere tilt, neck-shaft angle, fixation techniques and surgical approaches (see Hsu et al. (2011), Nigro et al. (2013), Virani et al. (2008), Berliner et al. (2015), Gutiérrez et al. (2011)). The design has not yet been optimised and the research is ongoing.

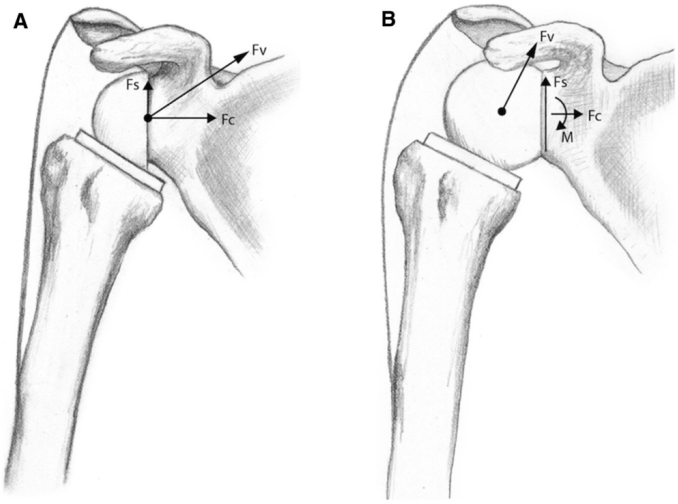

Fig. 3.5: Medialised (A) and lateralised (B) centre of rotation of the reverse shoulder, where F_c and F_s are the compressive and shear components of the joint contact force F_v, respectively, and M is the moment induced at the baseplate-bone interface due to the lateralised centre of rotation (Berliner et al., 2015).

3.4 Experimental and computational analysis

Analyses of the different reverse shoulder designs and design factors are reported in the literature. One method is the biomechanical analysis of the shoulder. Generally the upper limb is modelled in an appropriate software, such as SIMM (Software for Interactive Musculoskeletal Modeling) (MusculoGraphics, 2012-2016). The muscles are attached to the bones and the muscle lengths, moment arms, forces and range of motion are analysed. A virtual surgery may be performed to implant a standard or reverse prosthesis and the resulting biomechanics analysed. For an overview of the biomechanical models see Prinold et al. (2013). One such biomechanical model is the Newcastle Shoulder Model (NSM) developed by Kontaxis and Johnson (2009). The official model and the model developed by collaborators in the Department of Orthopaedics at UCT in collaboration with Kontaxis and Johnson for a reverse shoulder are shown in Figure 3.6. Collaborators at UCT are therefore able to provide the muscle attachment points and forces. The model is used in studies such as investigating the optimal humeral tray position where the humeral cup is fitted (see Berhouet et al. (2014b)). The investigation of the effect of the lateralisation of the centre of rotation on the joint contact forces is another example of the application of the model (Costantini et al., 2015).

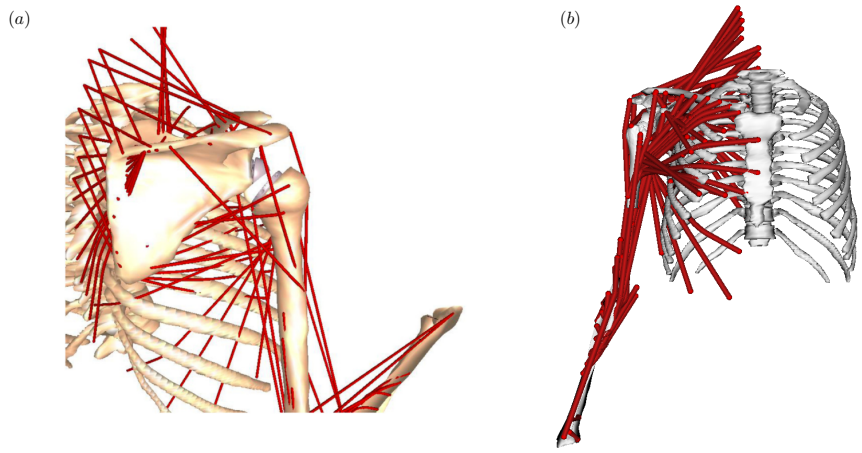

Fig. 3.6: An image of the (a) original Newcastle shoulder model from Berhouet et al. (2014b) and (b) a graphic of the Newcastle shoulder model implemented in OpenSim (NCSRR, 2010) by collaborators in the Department of Orthopaedics at UCT.

Other testing procedures for glenoid component loosening are detailed in the ASTM standard F2028-14 (ASTM, 2015). Here the glenosphere component is screwed into a high-strength polyurethane foam block, as the material properties of the polyurethane foam block are comparable to human cancellous bone. Therefore polyurethane foam is frequently used as a bone substitute in experiments. The material properties for the foam block are detailed in the ASTM standard F1839-08 (ASTM, 2014). The experimental guidelines state that the glenoid component should be loaded in compression and shear over a number of cycles. One possible experimental test proposed by the standard is shown in Figure 3.7. The worst case loading scenario at the glenohumeral joint is taken as 89% of a standard body weight of 86 kg. This results in a shear and compressive force of 750 N. The Young's modulus recommended in this standard is 193 MPa, as this value conforms with the ASTM F1839-08 standard and correlates well with values reported for the cancellous glenoid bone.

Glenohumeral contact forces are also reported in the literature, see e.g. Anglin et al. (2000). Harman et al. (2005) investigated glenoid loosening by following the guidelines set out in the ASTM standard F2028-14. The experimental set-up is shown in Figure 3.8. The micromotion threshold, i.e. the maximum allowable relative motion at the implant-bone interface, is reported to be 150 μm to ensure bone ingrowth and thus secure implant fixation. Harman et al. compared two different implants, the Delta

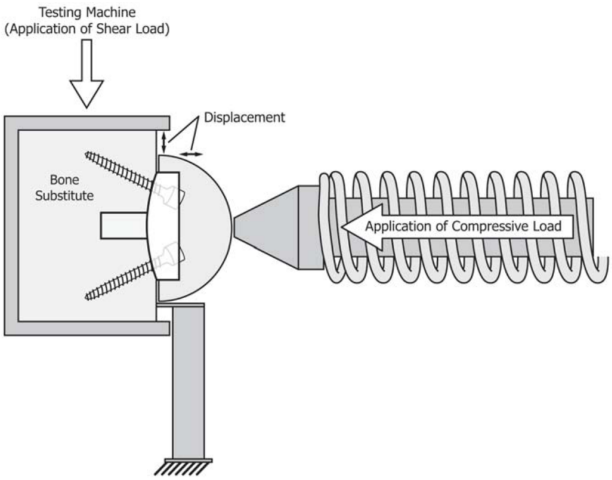

Fig. 3.7: A possible test set-up as detailed by the ASTM F2028-14 standard to analyse glenoid loosening by screwing the glenoid component into a polyurthane foam block and applying compressive and shear loads of ±750 N (ASTM, 2015).

III prosthesis manufactured by DePuy and the Reverse Shoulder Prosthesis (RSP) manufactured by Encore Medical Corp, by analysing the micro-motion.

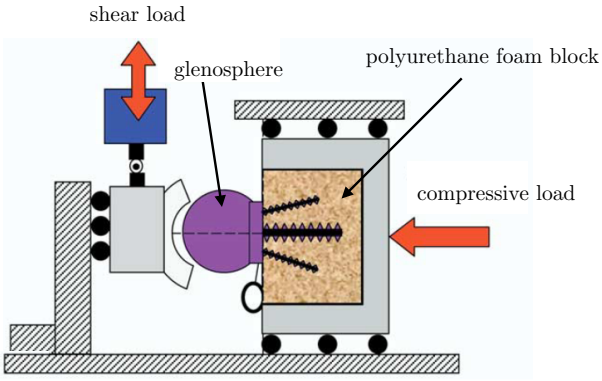

Fig. 3.8: The experimental set-up used by Harman et al. (2005).

Virani et al. (2008) followed the same testing procedure as Harman et al. (2005) and evaluated the same prostheses, but considered 7 different glenosphere-baseplate configurations. No significant differences between the designs were reported. Virani et al. did not only experimentally investigate the micro-motion at the implant-bone interface, but also simulated it using the finite element method. The mesh for the finite element model is shown in Figure 3.9.

A similar analysis is reported by Gutiérrez et al. (2011) who investigated the compressive forces under the glenosphere for different glenosphere placements. Nigro et al. (2013), also reported a similar set-up, analysing the effect of the contact area on the stability of the baseplate using the finite element method. Finally, Hopkins et al. (2008) reported on a micro-motion analysis of the set-up using the finite element method. Hopkins et al. took into account the bone quality by varying the magnitude of the Young's modulus. They concluded that increasing the length and diameter of the fixation screws and increasing the inclination of the glenosphere, decreases the micromotion.

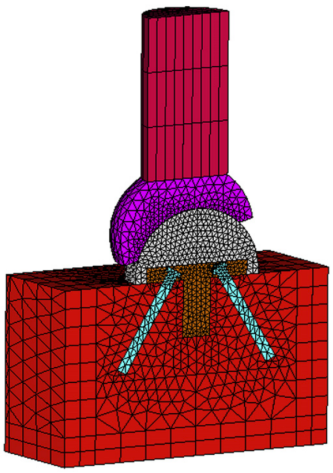

Fig. 3.9: The finite element mesh for the Delta III prosthesis by DePuy implanted in a polyurethane foam block used by Virani et al. (2008) to investigate the micro-motion at the implant-bone interface.

The material properties vary among the studies reported here. The ASTM standard F1839-08 is followed by the authors, however, a relatively wide range of material properties are used. The different material properties reported in some of the studies are summarised in Table 3.1.

Table 3.1: A summary of the material properties used in the investigations of glenoid side loosening associated with a reverse shoulder procedure. E = Young's Modulus, ν = Poisson's ratio, ρ = density.

source	foam block: high strength polyurethane	glenosphere: cobalt-chromium-molybdenum (CoCrMo) alloy	baseplate and screws: Titanium (Ti6Al4V) alloy
Virani et al. (2008), Gutiérrez et al. (2011) Nigro et al. (2013) Harman et al. (2005)	E = 553 MPa, $\nu = 0.25$	E = 230 GPa $\nu = 0.3$	E =117 GPa $\nu = 0.3$
Hopkins et al. (2008)	E = 193 MPa	E = 220 GPa	E = 110 GPa

Baseplate motion has also been investigated in cadaveric studies. James et al. (2013) investigated baseplate motion when four or two screws are used for glenosphere fixation. A reverse shoulder prosthesis was implanted in each scapula of six cadavers (James et al., 2013). The scapulae were tested in cyclic loading. James et al. reported that the use of two screws is sufficient to ensure secure implant fixation and that the inferior and superior screws are the most important. Berhouet et al. (2014a) also performed a cadaveric study. 40 cadaver shoulders were implanted, with different centre of rotations and humeral component inclination. The maximum range of motion for abduction and adduction was determined.

Vaupel et al. (2012) and Smith et al. (2015) examined polyethylene wear of the humeral cup. Vaupel et al. used a hip wear simulator to examine the polyethylene wear. Smith et al. (2015) developed a wear simulator specifically to investigate the wear associated with the reverse shoulder procedure. Ribeiro et al. (2011) and Quental et al. (2015) report on computational analyses of polyethylene cup wear in the conventional and reverse shoulder procedure using the finite element method.

The finite element method has successfully been used for stress analyses in a conventional anatomical shoulder replacement (see for example Gunther et al. (2012), Mansat et al. (2007), Gupta et al. (2004), Stone et al. (1999), Yongpravat et al. (2013), Sharma et al. (2010)). Finite element analysis is an important tool in orthopaedics, as the stress, strain and even remodelling state can be predicted. However, only a limited number of reports on the use of the finite element method in the scapula post reverse shoulder procedure are available. Yang et al. (2013) reported on a finite element simulation, considering the stress distribution and micromotion in two dimensions. The resulting von Mises stress distribution is shown in Figure 3.10.

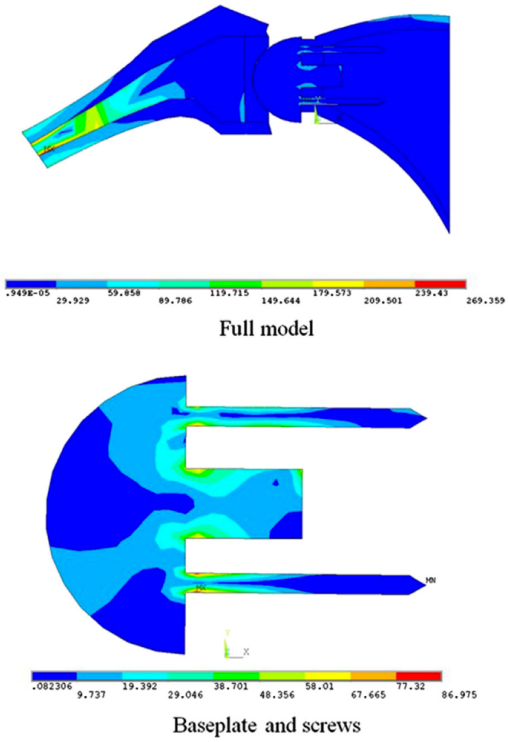

Fig. 3.10: The von Mises stress distribution in the reverse shoulder in 2D as reported by Yang et al. (2013).

The only finite element simulations of bone remodelling post reverse shoulder procedure in the scapula that the author is aware of are by Quental et al. (2014a). The remodelling theory adapted by Quental et al. is detailed in Chapter 2.2. Quental et al. simulated bone remodelling for a patient specific intact scapula. Four anatomical shoulder prosthesis and one reverse shoulder prosthesis were virtually implanted in the same subject specific scapula. All simulations were performed twice, once modelling a healthy scapula and then modelling an osteoporotic shoulder. The resulting densities of each scapula post procedure were compared with the intact scapula. The results post reverse total shoulder arthroplasty are shown in Figure 3.11.

Quental et al. (2014a) reported that the difference in densities between osteoporotic and healthy bone is only noticeable when considering the density magnitudes. The regions of bone apposition and resorption do not change.

This is the first study that the author is aware of, which considers bone remodelling post reverse shoulder procedure. A lot of work still lies ahead, as the medical field is moving more towards patient-specific treatments. An isotropic finite element model for bone remodelling in the scapula post reverse

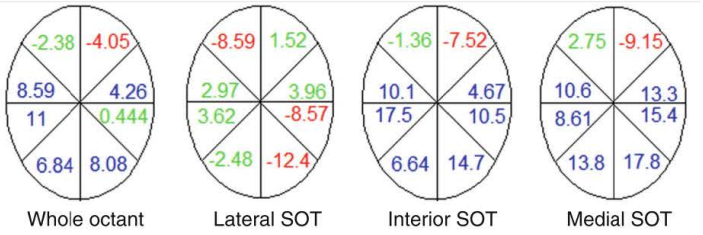

Fig. 3.11: The percentage changes in bone mass post reverses shoulder arthroplasty compared to the initial configuration in various slices of the glenoid, as reported by Quental et al. (2014a). Blue indicates bone apposition, red bone resorption and green indicates negligible changes in bone mass (Quental et al., 2014a).

total arthroplasty is developed in this project as a first step in the process of developing a reliable predictive computational tool. The isotropic model is easier to implement and validate at first to provide a solid foundation for the extension of the model, where anisotropy may be incorporated.

3.5 Summary

The reverse total shoulder procedure was developed for rotator cuff deficient patient. By removing the humeral head and replacing it by a humeral cup and screwing a glenosphere into the scapula, the integrity of the joint can be restored. The deltoid muscle now compensates for the absent rotator cuff muscles. However, up to 75 % complications are reported in some clinical series (Hsu et al., 2011). These complications include scapular notching and glenosphere loosening.

Biomechanical models of the upper extremity, such as the Newcastle shoulder model, have been developed to analyse the shoulder post procedure. Further, cadaveric studies and wear simulations are reported. Glenosphere loosening is analysed with the guidelines set out in the ASTM standard F2028-14 (ASTM, 2015). Computational analysis of the reverse shoulder procedure is limited. A reliable predictable tool to determine the stress and density distribution in the scapula post reverse shoulder arthroplasty would be an invaluable tool in the design process, especially considering the complications reported.

4

Continuum formulation for bone

Bone is modelled here as a continuum. This means that it is treated as continuous matter on the macro-scale. The micro-structure of bone is thus not directly accounted for. An image showing the complexity of the bone remodelling process at the micro-scale is shown in Figure 4.1.

The kinematics and general notation for the continuum formulation for bone are now defined. The Kuhl and Steinmann (2003) theory, which is based on open system thermodynamics, is adopted. To thoroughly define the necessary balance relations, the relations for a closed system approach are detailed first, followed by the open system formulation. The constitutive relations for bone remodelling are then detailed. Finally, the relative bone density is introduced as the primary variable in the governing and constitutive relations.

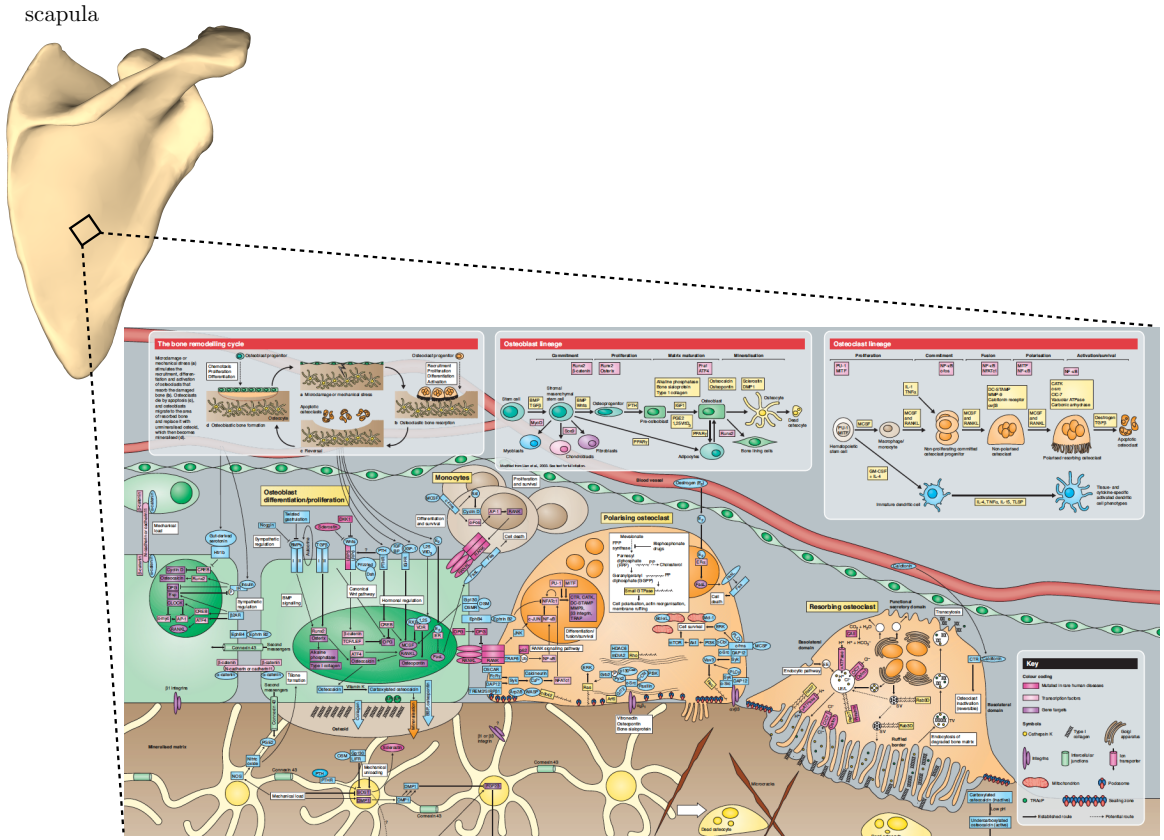

Fig. 4.1: The macro-scale and the highly complex process involved in remodelling on the microlevel of bone (Crockett et al., 2011)

4.1 Kinematics

Kinematics in continuum mechanics is the description of the motion characterising the deformation of a body as depicted in Figure 4.2.

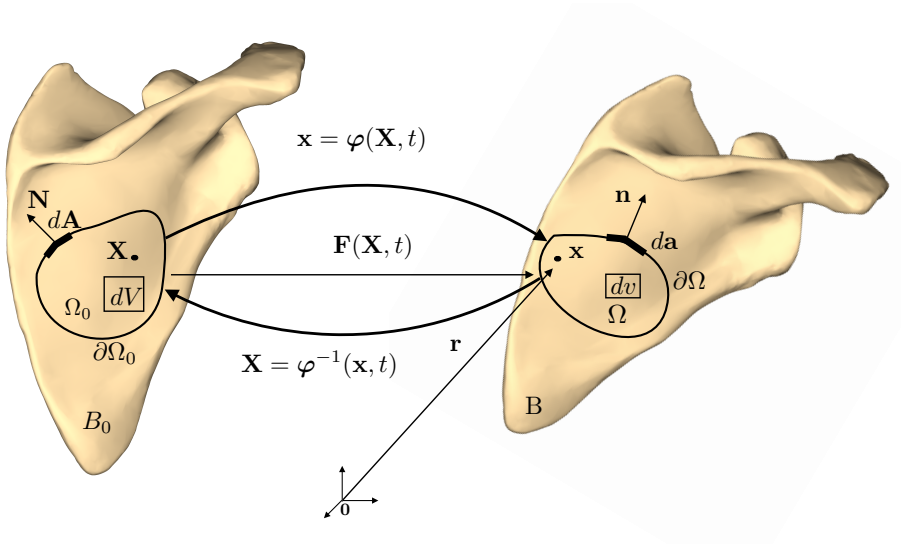

Fig. 4.2: Motion and deformation of a continuum body in a closed system.

At time $t = t_0$ the body is in the reference configuration, also called the Lagrangian configuration. At time $t > t_0$ the body occupies the current (Eulerian) configuration. This configuration describes the deformed body after it has been exposed to some loading conditions. $\mathbf{X}$ is a material point in the body B_0 in the reference configuration. The non-linear deformation map called the motion $\mathbf{x} = \boldsymbol{\varphi}(\mathbf{X}, t)$ maps point $\mathbf{X}$ to $\mathbf{x}$ in the current configuration. Similarly, the inverse of the deformation map is defined by $\mathbf{X} = \boldsymbol{\varphi}^{-1}(\mathbf{x}, t)$.

4.1.1 Notation

At this point the notation is defined. The scalar product of vectors $\boldsymbol{a}$ and $\boldsymbol{b}$ is denoted by $\boldsymbol{a} \cdot \boldsymbol{b}$ and the cross product by $\boldsymbol{a} \times \boldsymbol{b}$. The third-order permutation tensor is denoted by $\boldsymbol{\epsilon}$. The scalar product of two tensors $\boldsymbol{A}$ and $\boldsymbol{B}$ is denoted as $\boldsymbol{A} : \boldsymbol{B}$. The cofactor of a tensor cof$\boldsymbol{A}$ is defined by cof$\boldsymbol{A}$ = [det$\boldsymbol{A}$]$\boldsymbol{A}^{-T}$, where det$\boldsymbol{A}$ is the determinant of $\boldsymbol{A}$.

Upper case letters indicate quantities in the reference configuration, whereas lower case letters refer to quantities in the current configuration.

The material and spatial gradients of a quantity $\{\bullet\}$ are defined by Grad$\{\bullet\} = \frac{\partial\{\bullet\}}{\partial \mathbf{X}}$ and grad$\{\bullet\} = \frac{\partial\{\bullet\}}{\partial \mathbf{x}}$, respectively. Similarly the divergence of a quantity in the material placement Div$\{\bullet\}$ and current configuration div$\{\bullet\}$ are taken with respect to the material placement $\boldsymbol{X}$ and current position $\boldsymbol{x}$, respectively. The total derivative with respect to time of any quantity is denoted by $D_t\{\bullet\}$ and may also be denoted as $\{\dot{\bullet}\}$ in some instances, where there is no chance of confusion. For further details, see Holzapfel (2001).

4.1.2 Kinematic relations

The remaining kinematic relations are now detailed. The gradient of the non-linear deformation map $\mathbf{F}$ = Grad$\boldsymbol{\varphi}$ is termed the deformation gradient. The deformation gradient transforms line, area and volume elements between the configurations (see Figure 4.2) as follows:

$$
\begin{aligned}
\text{line element:} \quad & d\mathbf{x} = \mathbf{F} d\mathbf{X} \,, \\
\text{area element:} \quad & d\mathbf{a} = \text{cof}(\mathbf{F}) d\mathbf{A} \,, \\
\text{volume element:} \quad & dv = J dV \text{ where } J = \det\mathbf{F} \,.
\end{aligned}
$$

The velocity and acceleration are given by the first and second temporal derivatives of the motion as

$$
\mathbf{V}(\mathbf{X}, t) = \frac{\partial \boldsymbol{\varphi}(\mathbf{X}, t)}{\partial t} \qquad \text{and} \qquad \mathbf{A}(\mathbf{X}, t) = \frac{\partial \mathbf{V}(\mathbf{X}, t)}{\partial t} \,.
$$

In the current configuration, the velocity and acceleration field are defined by

$$
\mathbf{v}(\mathbf{x}, t) = \frac{\partial \boldsymbol{\varphi}(\mathbf{x}, t)}{\partial t} \qquad \text{and} \qquad \mathbf{a}(\mathbf{x}, t) = \frac{\partial \mathbf{v}(\mathbf{x}, t)}{\partial t} + \text{grad}\mathbf{v}(\mathbf{x}, t) \cdot \mathbf{v}(\mathbf{x}, t) \,.
$$

4.1.3 Strain and stress measures

The strain and stress measures used in the continuum formulations for bone remodelling are detailed in this section.

The right Cauchy-Green tensor $\boldsymbol{C} = \boldsymbol{F}^T \boldsymbol{F}$ and the left Cauchy-Green tensor $\boldsymbol{b} = \boldsymbol{F}\boldsymbol{F}^T$ are introduced as the strain measures in the material and current configurations respectively.

The stress tensors are introduced through Cauchy's stress theorem. A traction force $\boldsymbol{t}(\boldsymbol{x}, t, \boldsymbol{n})$, called the Cauchy traction in the current configuration, acts on the surface $\partial\Omega$ with outward unit normal $\boldsymbol{n}$. Cauchy's theorem states that there exists a spatial tensor field $\boldsymbol{\sigma}(\boldsymbol{x}, t)$, which is called the Cauchy stress tensor, such that $\boldsymbol{t}(\boldsymbol{x}, t, \boldsymbol{n}) = \boldsymbol{\sigma}(\boldsymbol{x}, t)\boldsymbol{n}$, i.e. the traction is linear in the normal $\boldsymbol{n}$.

The first Piola-Kirchhoff traction $\boldsymbol{T}(\boldsymbol{X}, t, \boldsymbol{N})$ is the counterpart of the Cauchy traction in the material configuration. The first Piola-Kirchhoff stress tensor, is a two-point tensor, defined by $\boldsymbol{T}(\boldsymbol{X}, t, \boldsymbol{N}) = \boldsymbol{P}(\boldsymbol{X}, t)\boldsymbol{N}$, where $\boldsymbol{N}$ is the outward unit normal of the surface $\partial\Omega$ in the material setting.

The divergence of the two stress tensors $\boldsymbol{\sigma}$ and $\boldsymbol{P}$ are related via the Piola Identity $\text{Div}(J\boldsymbol{F}^{-T}) = 0$ and using the standard relation $\text{Div}(\boldsymbol{A}) = \text{div}(\boldsymbol{A})\boldsymbol{F}^{-T}$, where $\boldsymbol{A}$ is a second-order tensor. The relation is thus given by

$$
\text{Div}\boldsymbol{P} = \text{Div}(J\boldsymbol{\sigma}\boldsymbol{F}^{-T}) = J\text{Div}(\boldsymbol{\sigma})\boldsymbol{F}^{-T} = J\text{div}(\boldsymbol{\sigma}) \,.
$$

4.2 Balance relations

The balance relations are obtained from the conservation of fundamental properties. The balances can be performed either using a closed or open system approach. Bone remodelling is modelled here using an open system continuum thermodynamics framework. The balance relations will however, first be derived for the more familiar closed system, followed by the open system formulation. The balance relations are those of mass, linear and angular momentum, energy and entropy.

4.2.1 Closed system

Holzapfel (2001) defines a system as a particular collection of matter in space. The system boundary $\partial\Omega$ separates the system Ω from the surroundings. A closed system contains a fixed amount of mass (control mass), while energy in the form of thermal energy and mechanical energy can flux across the boundary as shown in Figure 4.3. The balance relations are presented following Holzapfel (2001).

Balance of mass

The mass of the system is the defined by $m(\Omega_0) = \rho_0 V(\Omega_0)$ and similarly $m(\Omega) = \rho v(\Omega)$. The balance of mass relation is also referred to as the conservation of mass in a closed system as no mass

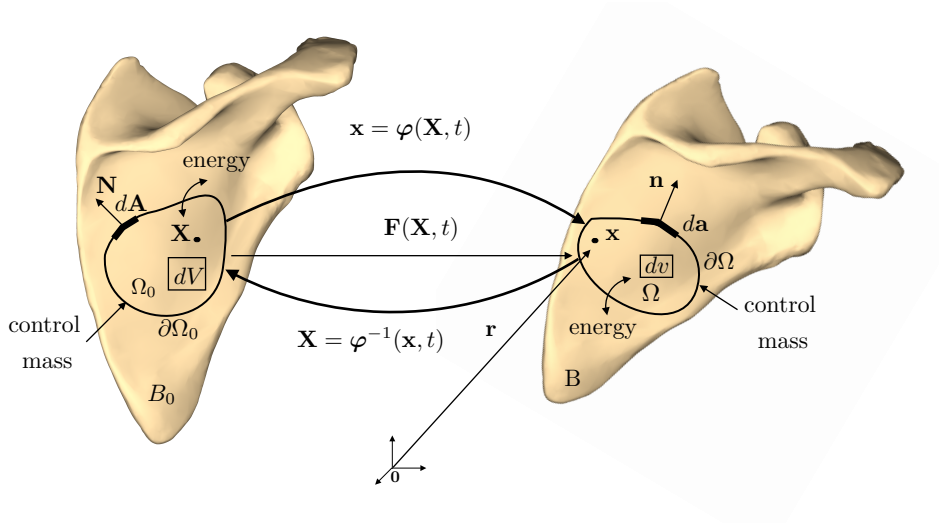

Fig. 4.3: Motion and deformation of a continuum body in a closed system

sources/sinks are present. The volume may change, but the mass in the system is always conserved during motion, making it an invariant of the system. The balance and conservation of mass are given by

$$m(\Omega_0) = m(\Omega) > 0 \,\forall t \qquad \text{and} \qquad D_t[m(\Omega_0)] = D_t[m(\Omega)] = 0\,.$$

The reference density $\rho_0(\mathbf{X})$ only depends on the material position $\mathbf{X}$. The current density $\rho(\mathbf{x}, t)$ depends on the current position $\mathbf{x}$ and time t. The balance of mass is now formulated for the infinitesimal mass elements $\mathrm{d}m(\boldsymbol{X})$ and $\mathrm{d}m(\boldsymbol{x})$ of the infinitesimal volume elements $\mathrm{d}V$ and $\mathrm{d}v$ in the reference and current configurations respectively,

$$\mathrm{d}m(\mathbf{X}) = \rho_0(\mathbf{X})\mathrm{d}V \qquad \text{and} \qquad \mathrm{d}m(\mathbf{x}, t) = \rho(\mathbf{x}, t)\mathrm{d}v\,.$$

The infinitesimal mass also satisfies balance of mass relation $\mathrm{d}m(\mathbf{X}) = \mathrm{d}m(\mathbf{x}, t) > 0$. Therefore the relation $\rho_0(\mathbf{X})\mathrm{d}V = \rho(\mathbf{x}, t)\mathrm{d}v > 0$ holds. The total mass is the integral of the infinitesimal mass element over the domain, given by

$$m = \int_{\Omega_0} \rho_0(\mathbf{X}) dV = \int_{\Omega} \rho(\mathbf{x}, t) dv \; = \text{constant} \; > 0\,.$$

The continuity of mass follows from this relation as

$$\int_{\Omega_0} \rho_0(\mathbf{X}) dV - \int_{\Omega} \rho(\mathbf{x}, t) dv \; = \; 0\,.$$

Making use of the determinant of the deformation gradient J to transform the infinitesimal volume element $\mathrm{d}v$ to the reference configuration, results in the integral expression

$$\int_{\Omega_0} [\rho_0(\mathbf{X}) - J\rho(\mathbf{x}, t)] dV \; = \; 0\,.$$

As the volume is arbitrary, the relation between the reference and current density is given by

$$\rho_0 = J\rho. \tag{4.1}$$

The conservation of mass states that the material time derivative of the mass is zero, that is

$$D_t \int_{\Omega_0} \rho_0(\mathbf{X}) dV = D_t \int_{\Omega} \rho(\mathbf{x}, t) dv \; = \; 0 \, .$$

Therefore

$$D_t \int_{\Omega_0} \rho_0(\mathbf{X}) dV - D_t \int_{\Omega} \rho(\mathbf{x}, t) dv \; = \; 0 \, .$$

Again, the integral over the current domain is transformed to the reference configuration, resulting in the integral expression

$$D_t \int_{\Omega_0} [\rho_0(\mathbf{X}) - J\rho(\mathbf{x}, t)] dV \; = \; 0 \, .$$

The domain Ω_0 is independent of time, this leads to the expression

$$\int_{\Omega_0} [D_t \rho_0(\mathbf{X}) - D_t J\rho(\mathbf{x}, t)] dV \; = \; 0 \, .$$

Finally, as the volume is arbitrary, the time derivatives of the reference and current density are related by

$$D_t[\rho_0] = D_t[J\rho] = 0. \tag{4.2}$$

Balance of momentum

The linear momentum $\boldsymbol{L}(t)$ is defined by

$$\boldsymbol{L}(t) = \int_{\Omega} \rho(\boldsymbol{x}, t) \boldsymbol{v}(\boldsymbol{x}, t) dv = \int_{\Omega_0} \rho_0(\boldsymbol{X}) \boldsymbol{V}(\boldsymbol{X}, t) dV \, .$$

The angular momentum $\mathbf{J}(t)$ is defined by

$$\boldsymbol{J}(t) = \int_{\Omega} \boldsymbol{r} \times \rho(\boldsymbol{x}, t) \boldsymbol{v}(\boldsymbol{x}, t) dv = \int_{\Omega_0} \boldsymbol{r} \times \rho(\boldsymbol{X}) \boldsymbol{V}(\boldsymbol{X}, t) dV \, ,$$

where $\mathbf{r}$ is the vector from the origin to the point $\boldsymbol{x}$, see Figure 4.3.

.

The balance of linear momentum is given by

$$\dot{\boldsymbol{L}}(t) = D_t \left[\int_{\Omega} \rho(\boldsymbol{x}, t) \boldsymbol{v}(\boldsymbol{x}, t) dv \right] = D_t \left[\int_{\Omega_0} \rho(\boldsymbol{X}) \boldsymbol{V}(\boldsymbol{X}, t) dV \right] = \boldsymbol{F}_{\text{ext}}(t) \, ,$$

where $\boldsymbol{F}_{\text{ext}}(t)$ is the net external force acting on the system. Similarly, the balance of angular momentum is given by

$$\dot{\boldsymbol{J}}(t) = D_t \left[\int_{\Omega} \boldsymbol{r} \times \rho(\boldsymbol{x}, t) \boldsymbol{v}(\boldsymbol{x}, t) dv \right] = D_t \left[\int_{\Omega_0} \boldsymbol{r} \times \rho(\boldsymbol{X}) \boldsymbol{V}(\boldsymbol{X}, t) dV \right] = \boldsymbol{M}(t) \, .$$

Here $\boldsymbol{M}(t)$ is the resultant moment due to the external force $\boldsymbol{F}_{\text{ext}}(t)$. The external force is due to tractions $\boldsymbol{t}(\boldsymbol{x}, t, \boldsymbol{n})$ acting on the surface $\partial\Omega$ with unit outward normal $\mathbf{n}$ (see Figure 4.2), as well as a body force $\boldsymbol{b}$ acting within the body Ω in the current configuration. The total external force is thus given by

$$\boldsymbol{F}_{\text{ext}}(t) = \int_{\partial\Omega} \boldsymbol{t}(\boldsymbol{x}, t, \boldsymbol{n}) ds + \int_{\Omega} \boldsymbol{b}(\boldsymbol{x}, t) dv \, .$$

The total moment due to the external force acting at $\boldsymbol{r}$ (see Figure 4.2), is given by

$$\boldsymbol{M}(t) = \int_{\partial\Omega} \boldsymbol{r} \times \boldsymbol{t}(\boldsymbol{x}, t, \boldsymbol{n}) ds + \int_{\Omega} \boldsymbol{r} \times \boldsymbol{b}(\boldsymbol{x}, t) dv \,.$$

Using Cauchy's stress theorem and the divergence theorem, the contribution due to the traction can be rephrased as

$$\int_{\partial\Omega} \boldsymbol{t}(\boldsymbol{x}, t, \boldsymbol{n}) ds = \int_{\partial\Omega} \boldsymbol{\sigma}(\boldsymbol{x}, t) \boldsymbol{n} ds = \int_{\Omega} \mathrm{div}\boldsymbol{\sigma} dv \,.$$

Using this relation and making use of rate of change of the density (see equation 4.2), the balance of linear momentum can now be expressed as

$$\dot{\boldsymbol{L}}(t) = D_t \int_{\Omega} \rho(\boldsymbol{x}, t) \boldsymbol{v}(\boldsymbol{x}, t) dv = \int_{\Omega} \rho(\boldsymbol{x}, t) \dot{\boldsymbol{v}}(\boldsymbol{x}, t) dv = \int_{\Omega} (\mathrm{div}\boldsymbol{\sigma} + \boldsymbol{b}) dv.$$

In global form the balance of linear momentum is given by

$$\int_{\Omega} (\mathrm{div}\boldsymbol{\sigma} + \boldsymbol{b} - \rho\dot{\boldsymbol{v}}) dv = \boldsymbol{0} \,.$$

Similarly, the local form of the balance of linear momentum is given by

$$\mathrm{div}\boldsymbol{\sigma} + \boldsymbol{b} = \rho\dot{\boldsymbol{v}} \,.$$

A material description of the balance of linear momentum is obtained by transforming the current balance relation as detailed below. The density and body force is transformed from the current to the reference configuration with the determinant of the deformation gradient as

$$\rho_0 := J\rho \qquad \text{and} \qquad \boldsymbol{B} := J\boldsymbol{b} \,.$$

The acceleration is simply transformed from the current to reference configuration, by changing the parametrisation, that is

$$\dot{\boldsymbol{v}}(\boldsymbol{x}, t) \to \dot{\boldsymbol{V}}(\boldsymbol{X}, t) \,.$$

The relationship between the divergence of the stress measures is given by

$$\mathrm{Div}\boldsymbol{P} = J\mathrm{div}[\boldsymbol{\sigma}] \,.$$

The global form of the balance of momentum can now be expressed as

$$\int_{\Omega} [\mathrm{div}\boldsymbol{\sigma} + \boldsymbol{b} - \rho\dot{\boldsymbol{v}}] dv = \int_{\Omega_0} [\mathrm{Div}\boldsymbol{P} + \boldsymbol{B} - \rho_0\dot{\boldsymbol{V}}] dV \,.$$

The local form of the balance of linear momentum in the material description is thus given by

$$\mathrm{Div}\boldsymbol{P} + \boldsymbol{B} = \rho_0\dot{\boldsymbol{V}} \,. \tag{4.3}$$

The proof for the symmetry of the Cauchy stress tensor stems from the balance of angular momentum. Again, using Cauchy's stress theorem the following substitutions can be made:

$$\int_{\partial\Omega} \boldsymbol{r} \times \boldsymbol{t}(\boldsymbol{x}, t, \boldsymbol{n}) ds = \int_{\partial\Omega} \boldsymbol{r} \times \boldsymbol{\sigma}(\boldsymbol{x}, t) \boldsymbol{n} ds = \int_{\Omega} \boldsymbol{r} \times \mathrm{div}\boldsymbol{\sigma} + \boldsymbol{\epsilon} : \boldsymbol{\sigma}^T dv \,,$$

The global form in the current description of the balance of angular momentum is now given by

$$\int_{\Omega} \boldsymbol{r} \times (\mathrm{div}\boldsymbol{\sigma} + \boldsymbol{b} - \rho\dot{\boldsymbol{v}}) dv = \int_{\Omega} \boldsymbol{\epsilon} : \boldsymbol{\sigma}^T dv = \boldsymbol{0} \,.$$

As the volume is arbitrary, the local form of holds true and from the balance of linear momentum the left-hand side $= \mathbf{0}$ thus $\boldsymbol{\epsilon} : \boldsymbol{\sigma}^T = \mathbf{0}$, and from this it follows that the Cauchy stress is symmetric, that is

$$\boldsymbol{\sigma}^T = \boldsymbol{\sigma} \,.$$

As the first Piola-Kirchhoff stress $\boldsymbol{P}$ is related to the Cauchy stress through $\boldsymbol{P} = J\boldsymbol{\sigma}\boldsymbol{F}^{-T}$, it is a two-point tensor with one leg in the current and one in the reference configuration and is not symmetric. However, $\boldsymbol{S} := \boldsymbol{P}\boldsymbol{F}^T = \boldsymbol{F}\boldsymbol{P}^T = \boldsymbol{S}^T$ is symmetric and introduces the second Piola-Kirchhoff stress tensor $\boldsymbol{S}$.

Balance of energy

The energy balance is important, as it governs the transformation of one form of energy to another. It is necessary to ensure a sound thermodynamic formulation. The balance of energy comprises two parts, namely the balance of mechanical energy and the balance of thermal energy. The balance of mechanical energy is formulated first.

The balance of mechanical energy equates the external mechanical power $P_{\text{ext}}(t)$ with the kinetic energy $\kappa(t)$ and the internal mechanical work, also termed the stress power, $P_{\text{int}}(t)$.

The external mechanical power is the power input to a region Ω at time t due to the resultant external force $\boldsymbol{F}_{\text{ext}}(t)$, given by

$$P_{\text{ext}}(t) := \int_{\partial\Omega} \boldsymbol{t} \cdot \boldsymbol{v} \, ds + \int_{\Omega} \boldsymbol{b} \cdot \boldsymbol{v} \, dv \,.$$

The kinetic energy κ is simply the continuum mechanics counterpart of the Newtonian expression and is given by

$$\kappa(t) = \int_{\Omega} \frac{1}{2} \rho \boldsymbol{v}^2 \, dv \,.$$

The stress power P_{int} captures the deformation of the region Ω due to the applied stress field and is given by

$$P_{\text{int}}(t) := \int_{\Omega} \boldsymbol{\sigma} : \boldsymbol{d} \; dv \,,$$

where $\boldsymbol{d}$ is the rate of deformation tensor, defined by

$$\boldsymbol{d} = \frac{1}{2}[\text{grad}\boldsymbol{v} + (\text{grad}\boldsymbol{v})^T] \,.$$

The balance of mechanical energy is thus given by

$$D_t \kappa(t) + P_{\text{int}}(t) = P_{\text{ext}}(t) \,, \tag{4.4}$$

$$\rightarrow D_t \int_{\Omega} \frac{1}{2} \rho \boldsymbol{v}^2 \, dv + \int_{\Omega} \boldsymbol{\sigma} : \boldsymbol{d} \, dv = \int_{\partial\Omega} \boldsymbol{t} \cdot \boldsymbol{v} \, ds + \int_{\Omega} \boldsymbol{b} \cdot \boldsymbol{v} \, dv \,.$$

The balance of mechanical energy is equivalent to Cauchy's first equation of motion for an isothermal system. The traction term can be expressed as:

$$\int_{\partial\Omega} \boldsymbol{t} \cdot \boldsymbol{v} \, ds = \int_{\partial\Omega} \boldsymbol{\sigma}\boldsymbol{n} \cdot \boldsymbol{v} \, ds = \int_{\partial\Omega} \boldsymbol{\sigma}\boldsymbol{v} \cdot \boldsymbol{n} \, ds \text{ as } \boldsymbol{\sigma} = \boldsymbol{\sigma}^T \,.$$

Applying the divergence theorem results in the expression

$$\int_{\partial\Omega} \boldsymbol{t}\cdot\boldsymbol{v} ds = \int_{\Omega} \mathrm{div}\boldsymbol{\sigma}\boldsymbol{v}\, dv = \int_{\Omega} [\mathrm{div}\boldsymbol{\sigma}\cdot\boldsymbol{v} + \boldsymbol{\sigma} : \mathrm{grad}\boldsymbol{v}]\, dv\,.$$

Substituting this into the expression for the external power and adding and subtracting $\rho\dot{\boldsymbol{v}}\cdot\boldsymbol{v}$ yields

$$P_{\mathrm{ext}}(t) = \int_{\Omega} [\mathrm{div}\boldsymbol{\sigma} + \boldsymbol{b} - \rho\dot{\boldsymbol{v}}]\cdot\boldsymbol{v}\, dv + \int_{\Omega} [\boldsymbol{\sigma} : \mathrm{grad}\boldsymbol{v} + \rho\dot{\boldsymbol{v}}\cdot\boldsymbol{v}]\, dv.$$

Making use of Reynold's transport theorem[1], this external power equates to,

$$P_{\mathrm{ext}}(t) = \int_{\Omega} \boldsymbol{\sigma} : \mathrm{grad}\boldsymbol{v} + D_t \int_{\Omega} \frac{1}{2}\rho\boldsymbol{v}\cdot\boldsymbol{v}\, dv \;=\; P_{\mathrm{int}}(t) + D_t\kappa(t)\,,$$

as defined in equation 4.4.

The material description of the balance of mechanical energy is obtained through the usual transformations. The traction and body forces, as well as the velocity are transformed as detailed in section 4.2.1, where

$$\int_{\partial\Omega} \boldsymbol{t}\cdot\boldsymbol{v}\, ds = \int_{\partial\Omega_0} \boldsymbol{T}\cdot\boldsymbol{V}\, dS \qquad \text{and} \qquad \int_{\Omega} \boldsymbol{b}\cdot\boldsymbol{v}\, dv = \int_{\Omega_0} \boldsymbol{B}\cdot\boldsymbol{V}\, dV\,.$$

Similarly, the transformation of the time rate of change of the kinetic energy is given by

$$D_t \int_{\Omega} \frac{1}{2}\rho\boldsymbol{v}^2\, dv = D_t \int_{\Omega_0} \frac{1}{2}\rho_0\boldsymbol{V}^2\, dV.$$

Finally, the internal mechanical energy is transformed. The rate of deformation tensor can also be expressed as $\boldsymbol{d} = \dot{\boldsymbol{F}}\boldsymbol{F}^{-1}$ yielding

$$\int_{\Omega} \boldsymbol{\sigma} : \boldsymbol{d}\, dv = \int_{\Omega} \boldsymbol{\sigma} : \dot{\boldsymbol{F}}\boldsymbol{F}^{-1}\, dv = \int_{\Omega_0} J\boldsymbol{\sigma}\boldsymbol{F}^{-T} : \dot{\boldsymbol{F}}\, dV = \int_{\Omega_0} \boldsymbol{P} : \dot{\boldsymbol{F}}\, dV\,.$$

The material description of the balance of mechanical energy is thus given by

$$D_t \int_{\Omega_0} \frac{1}{2}\rho_0\boldsymbol{V}^2\, dV + \int_{\Omega_0} \boldsymbol{P} : \dot{\boldsymbol{F}}\, dV = \int_{\partial\Omega_0} \boldsymbol{T}\cdot\boldsymbol{V}\, dS + \int_{\Omega_0} \boldsymbol{B}\cdot\boldsymbol{V}\, dV\,.$$

The balance of energy in continuum thermodynamics includes both thermal and mechanical energy. Thermal power, which is the non-mechanical power, also referred to as the rate of thermal work $Q(t)$, is defined analogous to the external power and is given by

$$Q(t) = \int_{\partial\Omega} q_n\, ds + \int_{\Omega} q_0\, dv = \int_{\partial\Omega_0} Q_N\, dS + \int_{\Omega_0} Q_0\, dV\,.$$

Here $q_n(\boldsymbol{x}, t, \boldsymbol{n})$ and $Q_N(\boldsymbol{X}, t, \boldsymbol{N})$ are the heat fluxes and $q_0(\boldsymbol{x}, t)$ and $Q_0(\boldsymbol{X}, t)$ are the heat sources in the current and reference settings, respectively.

Similar to Cauchy's stress theorem, Stoke's flux theorem relates the fluxes to the outward unit normals $\boldsymbol{n}, \boldsymbol{N}$ as follows

$$\begin{aligned} q_n &= -\boldsymbol{q}\cdot\boldsymbol{n} && \text{where } \boldsymbol{q} \text{ is the Cauchy (true) heat flux}\,, \\ Q_N &= -\boldsymbol{Q}\cdot\boldsymbol{N} && \text{where } \boldsymbol{Q} \text{ is the Piola-Kirchhoff heat flux}\,. \end{aligned}$$

The heat fluxes $\boldsymbol{q}$ and $\boldsymbol{Q}$ are related via the Piola transformation $\boldsymbol{Q} = J\boldsymbol{F}^{-1}\boldsymbol{q}$.

[1] Reynolds' transport theorem: $D_t \int_{\Omega} f\, dv = \int_{\Omega} \frac{\partial f}{\partial t}\, dv + \int_{\partial\Omega} f\boldsymbol{v}\cdot\boldsymbol{n}\, ds$

The first law of thermodynamics is the balance of energy in the system. This law governs the transformation of one form of energy to another, but not the direction. The rate of internal energy $\varepsilon(t)$ is balanced by the rate of internal mechanical power $P_{\text{int}}(t)$ and the rate of thermal work $Q(t)$ as follows

$$D_t\varepsilon(t) = P_{\text{int}}(t) + Q(t)\,. \tag{4.5}$$

Substituting the balance of mechanical energy (equation 4.4) into the above equation yields

$$D_t\kappa(t) + D_t\varepsilon(t) = P_{\text{ext}}(t) + Q(t)\,.$$

Finally, substituting the expression

$$D_t\epsilon(t) = D_t \int_\Omega e\, dv$$

for the internal energy density (e in the local form) results in the expression

$$D_t \int_\Omega [\frac{1}{2}\rho \boldsymbol{v}^2 + e]\, dv = \int_{\partial\Omega} [\boldsymbol{t}\cdot\boldsymbol{v} - \boldsymbol{q}\cdot\boldsymbol{n}]\, ds + \int_\Omega [\boldsymbol{b}\cdot\boldsymbol{v} + q_0]\, dv\,,$$

$$D_t \int_\Omega e dv + \int_\Omega \rho\dot{\boldsymbol{v}}\cdot\boldsymbol{v}\, dv = \int_\Omega [[\text{div}\boldsymbol{\sigma} + \boldsymbol{b} - \rho\dot{\boldsymbol{v}}]\cdot\boldsymbol{v} \; + \boldsymbol{\sigma} : \text{grad}\boldsymbol{v} + q_0]\, dv + \int_{\partial\Omega} q_n\, ds\,.$$

This results in the expression for the internal energy

$$D_t \int_\Omega e\, dv = \int_\Omega [\boldsymbol{\sigma} : \boldsymbol{d} - \text{div}\boldsymbol{q} + q_0]\, dv\,.$$

The material description is determined similarly as reported for the balance of mechanical energy as

$$D_t \int_{\Omega_0} E\, dV = \int_{\Omega_0} \dot{E}\, dV = \int_\Omega [\boldsymbol{P} : \dot{\boldsymbol{F}} - \text{Div}\boldsymbol{Q} + Q_0]\, dV\,,$$

where E is the counterpart of e in the material description. In local form the balance of internal energy is given by

$$\dot{E} = \boldsymbol{P} : \dot{\boldsymbol{F}} - \text{Div}\boldsymbol{Q} + Q_0\,.$$

Balance of entropy

The balance of energy governs the transformation of mechanical work to heat. The entropy inequality, which is the second law of thermodynamics, governs the direction of the energy transfer. Entropy is a measure of disorder in a system and the entropy production is never decreasing. This can be explained with the naturally occurring irreversibilities in a system. In any system, energy dissipation occurs, for example through the generation of heat due to friction in a mechanical process.

The entropy inequality is important in the context of continuum thermodynamics, as it gives rise to the constitutive relations, necessary to describe the system. The entropy density is denoted by S per unit reference volume and s per unit current volume. The entropy in a continuum body $\tilde{S}$ is defined by:

$$\tilde{S} = \int_\Omega s(\boldsymbol{x}, t)\, dv = \int_{\Omega_0} S(\boldsymbol{X}, t)\, dV\,.$$

The rate of entropy input $\tilde{Q}(t)$ is defined by

$$\begin{aligned}\tilde{Q}(t) &= -\int_{\partial\Omega} \boldsymbol{h}\cdot\boldsymbol{n}\, ds + \int_{\Omega} h_0\, dv\,,\\ &= -\int_{\partial\Omega_0} \boldsymbol{H}\cdot\boldsymbol{N}\, dS + \int_{\Omega_0} H_0\, dV\,,\end{aligned}$$

where $\boldsymbol{h}$ is the Cauchy entropy flux, $\boldsymbol{H}$ the Piola-Kirchhoff entropy flux, and h_0 and H_0 are the entropy sources in the current and reference configurations.

The second law of thermodynamics states that the entropy production $\Gamma(t)$ is non negative, where the inequality accounts for the irreversibilities of the system, given by

$$\Gamma(t) = D_t\tilde{S}(t) - \tilde{Q}(t) \geq 0\,.$$

The entropy production density, in the local form $\gamma(t)$ and $\gamma_0(t)$ in the current and reference configuration, respectively, is therefore given by

$$\begin{aligned}\Gamma(t) &= \int_{\Omega} \gamma(t)\, dv = D_t\int_{\Omega} s(\boldsymbol{x},t)\, dv + \int_{\partial\Omega}\boldsymbol{h}\cdot\boldsymbol{n}\, ds - \int_{\Omega} h_0\, dv \geq 0\\ &= \int_{\Omega_0} \gamma_0(t)\, dV = D_t\int_{\Omega_0} S(\boldsymbol{X},t)\, dV + \int_{\partial\Omega_0}\boldsymbol{H}\cdot\boldsymbol{N}\, dS - \int_{\Omega_0} H_0\, dV \geq 0\,.\end{aligned}$$

Applying the divergence theorem yields

$$\Gamma(t) = \int_{\Omega_0} \gamma_0(t)\, dV = D_t\int_{\Omega_0} S(\boldsymbol{X},t)\, dV + \int_{\Omega_0}\mathrm{Div}\boldsymbol{H}\, dV - \int_{\Omega_0} H_0\, dV \geq 0\,.$$

The local form of the entropy inequality per unit reference volume is thus given by

$$\gamma_0(t) = D_t S(\boldsymbol{X},t) + \mathrm{Div}\boldsymbol{H} - H_0\,. \tag{4.6}$$

Next, the Clausius-Duhem inequality is introduced. This inequality arises from the assumption that the rate of entropy input and the rate of thermal work can be related via the absolute temperature $\theta > 0$. The flux and source terms are simply related as follows:

$$\boldsymbol{h} = \frac{\boldsymbol{q}}{\theta}\,,\ h_0 = \frac{r}{\theta} \qquad \text{and} \qquad \boldsymbol{H} = \frac{\boldsymbol{Q}}{\theta}\,,\ H_0 = \frac{Q_0}{\theta}\,.$$

Substituting the expressions of the heat flux and source into the entropy production inequality leads to the Clausius-Duhem inequality, given by

$$\Gamma(t) = D_t\int_{\Omega} s(\boldsymbol{x},t)\, dv + \int_{\partial\Omega}\frac{\boldsymbol{q}}{\theta}\cdot\boldsymbol{n}\, ds - \int_{\Omega}\frac{r}{\theta}\, dv \geq 0$$

in the current configuration and in the reference configuration given by

$$\Gamma(t) = D_t\int_{\Omega_0} S(\boldsymbol{X},t)\, dV + \int_{\partial\Omega_0}\frac{\boldsymbol{Q}}{\theta}\cdot\boldsymbol{N}\, dS - \int_{\Omega_0}\frac{Q_0}{\theta}\, dV \geq 0\,.$$

Applying the divergence theorem to the term $\int_{\partial\Omega_0}\frac{1}{\theta}\boldsymbol{Q}\cdot\boldsymbol{N}dS$ yields

$$\int_{\partial\Omega_0}\frac{\boldsymbol{Q}}{\theta}\cdot\boldsymbol{N}\, dS = \int_{\Omega_0}\mathrm{Div}(\frac{\boldsymbol{Q}}{\theta})\, dV = \int_{\Omega_0}\left[\frac{1}{\theta}\mathrm{Div}(\boldsymbol{Q}) - \frac{1}{\theta^2}\boldsymbol{Q}\cdot\mathrm{Grad}(\theta)\right]\, dV\,.$$

The Clausius-Duhem inequality can now be formulated in the local form as

$$\dot{S} + \frac{1}{\theta}\mathrm{Div}\boldsymbol{Q} - \frac{1}{\theta^2}\boldsymbol{Q}\cdot\mathrm{Grad}(\theta) - \frac{Q_0}{\theta} \geq 0\,.$$

Substituting the expression for the heat source from the balance of energy, that is

$$Q_0 = \dot{E} - \boldsymbol{P} : \dot{\boldsymbol{F}} + \mathrm{Div}\boldsymbol{Q}\,,$$

results in the following formulation for the Clausius-Duhem inequality:

$$\boldsymbol{P} : \dot{\boldsymbol{F}} - \dot{E} + \theta \dot{S} - \frac{1}{\theta} \boldsymbol{Q} \cdot \mathrm{Grad}(\theta) \geq 0 \,.$$

Each term in the Clausius-Duhem inequality has to be greater than or equal to zero. The heat conduction inequality follows from this, given by:

$$\theta > 0 \;\rightarrow \boldsymbol{Q} \cdot \mathrm{Grad}(\theta) \leq 0 \,.$$

A reduced form of the second law follows from the heat conduction inequality and the Clausius-Duhem inequality. This is the Clausius-Planck inequality, which introduces the internal dissipation, also referred to as the local production of entropy, D_{int}, given by

$$D_{\mathrm{int}} = \boldsymbol{P} : \dot{\boldsymbol{F}} - \dot{E} + \theta \dot{S} \geq 0 \,.$$

From the balance of energy:

$$\boldsymbol{P} : \dot{\boldsymbol{F}} - \dot{E} = -\mathrm{Div}\boldsymbol{Q} + Q_0 \,.$$

Substituting this into the internal dissipation inequality yields

$$D_{\mathrm{int}} = \mathrm{Div}\boldsymbol{Q} - Q_0 \theta + \dot{S} \geq 0 \,.$$

Finally, Duhamel's law of heat conduction is introduced. This is a phenomenological law, which states that the heat flux depends on the temperature gradient, as heat flows from hot to cold. Duhamel's law of heat conduction is thus defined as follows

$$\boldsymbol{q} = -\boldsymbol{\kappa} \mathrm{grad}\theta \qquad \text{and} \qquad \boldsymbol{Q} = -\boldsymbol{F}^{-1} \boldsymbol{\kappa}_0 \boldsymbol{F}^{-T} \mathrm{Grad}\theta \,,$$

where $\boldsymbol{\kappa}$ s the spatial thermal conductivity tensor and $\boldsymbol{\kappa}_0 = J\boldsymbol{\kappa}$.

In the case of thermal isotropy, $\boldsymbol{\kappa} = \kappa \boldsymbol{I}$ and $\boldsymbol{\kappa}_0 = \kappa_0 \boldsymbol{I}$. Duhamel's law of heat conduction can now be expressed as

$$\boldsymbol{q} = -\kappa \mathrm{grad}\theta \qquad \text{and} \qquad \boldsymbol{Q} = -\kappa_0 \boldsymbol{C}^{-1} \mathrm{Grad}\theta \,,$$

which is also known as Fourier's law of heat conduction. κ and κ_0 are the heat conduction coefficients and $\boldsymbol{C}^{-1}$ is the inverse of the right Cauchy-Green strain tensor.

As a final step in the derivation, the heat equation is introduced, following from the first law of thermodynamics (4.5). The heat equation in the material configuration is given by

$$\rho_0 c_h D_t \theta = -\mathrm{Div}\boldsymbol{Q} + Q_0 \,, \tag{4.7}$$

where c_h is the heat capacity.

Summary of balance relations for a closed system in the material description

The fundamental relations in closed system thermodynamics are summarised in Table 4.1.

Table 4.1: Summary governing equations for a closed system (local form, reference configuration)

Balance of mass:	$D_t\rho_0 = D_t(J\rho) = 0$
Balance of linear momentum:	$\mathrm{Div}\boldsymbol{P} + \boldsymbol{B} = \rho_0\dot{\boldsymbol{V}}$
Balance of internal energy:	$\dot{E} = \boldsymbol{P} : \dot{\boldsymbol{F}} - \mathrm{Div}(\boldsymbol{Q}) + Q_0$
Balance of entropy:	$\gamma_0(t) = D_t S(\boldsymbol{X}, t) + \mathrm{Div}\boldsymbol{H} - H_0$
Dissipation inequality:	$D_{\mathrm{int}} = \mathrm{Div}\boldsymbol{Q} - Q_0\theta + \dot{S} \geq 0$

4.2.2 Open system

An open system contains a fixed volume. Unlike a closed system, energy and mass can cross the boundary as shown in Figure 4.4. Any quantity in an open system can be volume specific denoted by a subscript zero $\{\bullet\}_0$ or mass specific $\{\bullet\}$. The two quantities are related via the mass density as

$$\{\bullet\}_0 = \rho_0\{\bullet\}\,.$$

The density is a volume specific quantity, which will be denoted as before with ρ_0 in the reference configuration and ρ in the current configuration.

The balance relations for the open system are based on those proposed by Kuhl and Steinmann (2003) and are detailed in the following sections.

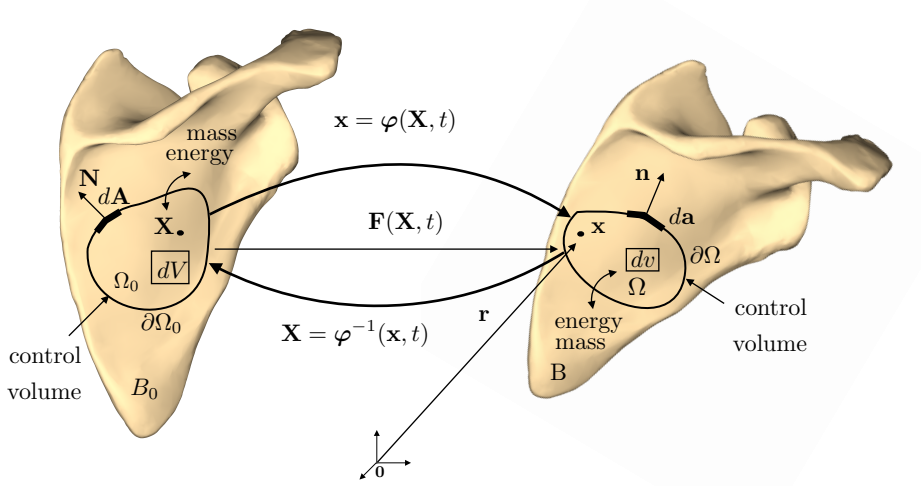

Fig. 4.4: Motion and deformation of a continuum body: control volume in an open system

Balance of mass

The mass of the control volume is not constant in an open system. Density sources/sinks are present in the control volume and a mass flux over the boundary of the control volume governs the density evolution. This implies that the density is parameterised in terms of the reference configuration $\rho_0(\boldsymbol{X}, t)$ is now also time dependent. The density evolution is given by

$$D_t\rho_0 = \mathrm{Div}\boldsymbol{R} + R_0\,, \tag{4.8}$$

where $\boldsymbol{R}$ is the mass flux and R_0 the mass source.

The incremental mass in the reference and current configuration at time t is the same, i.e. $dm(\boldsymbol{X},t) = dm(\boldsymbol{x},t)$. The transformation of the density between the two configurations is also given as before (see equation 4.1) by

$$\rho_0 = J\rho\,.$$

The balance of mass in an open system is therefore given by

$$D_t\rho_0 = D_t[J\rho] = \dot{J}\rho + J\dot{\rho} = \mathrm{div}\boldsymbol{v}\rho + J\dot{\rho} = \mathrm{Div}\boldsymbol{R} + R_0\,.$$

Balance of linear momentum

The volume specific balance of linear momentum $\boldsymbol{L_0}(t)$ is derived from Cauchy's first equation of motion. The closed system, volume specific version of Cauchy's first equation of motion, as detailed in section 4.2.1, is given by

$$\mathrm{div}\boldsymbol{\sigma} + \boldsymbol{b} = \rho\dot{\boldsymbol{v}}\,.$$

The right-hand side can be expressed as:

$$\rho\dot{\boldsymbol{v}} = \dot{\overline{\rho\boldsymbol{v}}} - \boldsymbol{v}\dot{\rho}\,. \tag{4.9}$$

The time rate of change of the density in the current configuration is given by

$$\dot{\rho} = j[\mathrm{Div}\boldsymbol{R} - \mathrm{div}\boldsymbol{v}\rho + R_0]\,.$$

Substituting into equation 4.9 yields

$$\rho\dot{\boldsymbol{v}} = \dot{\rho}\boldsymbol{v} - j[\mathrm{Div}\boldsymbol{R} - \mathrm{div}[\boldsymbol{v}]\rho + R_0]\boldsymbol{v}\,.$$

Now the balance of linear momentum equation is multiplied by the determinant of the deformation gradient J, which results in the material equivalent of the balance of linear momentum, given by

$$J\mathrm{div}\boldsymbol{\sigma} + J\boldsymbol{b} = \mathrm{Div}\boldsymbol{P} + \boldsymbol{B} = J\rho\dot{\boldsymbol{v}}\,.$$

This leads to

$$\mathrm{Div}\boldsymbol{P} + \boldsymbol{B} = J\dot{\rho}\dot{\boldsymbol{v}} - [\mathrm{Div}\boldsymbol{R} - \mathrm{div}(\boldsymbol{v})\rho + R_0]\boldsymbol{v}\,.$$

Rearranging the above yields:

$$J\dot{\rho}\dot{\boldsymbol{v}} + \mathrm{div}\boldsymbol{v}\ \ \rho\boldsymbol{v} = \mathrm{Div}\boldsymbol{P} + \boldsymbol{B} + [\mathrm{Div}\boldsymbol{R} + R_0]\boldsymbol{v}\,,$$

and making use of the following relations:

$$\mathrm{div}\boldsymbol{v}\rho = \dot{J}\rho = D_t\rho_0 - J\dot{\rho} \qquad \text{and therefore} \qquad \mathrm{div}\boldsymbol{v}\rho\boldsymbol{v} = [D_t\rho_0 - J\dot{\rho}]\boldsymbol{v}\,,$$

results in the following expression

$$J\dot{\rho}\dot{\boldsymbol{v}} + [D_t\rho_0 - J\dot{\rho}]\boldsymbol{v} = J\dot{\rho}\boldsymbol{v} + J\rho\dot{\boldsymbol{v}} + D_t\rho_0\boldsymbol{v} - J\dot{\rho}\boldsymbol{v} = \rho_0\dot{\boldsymbol{v}} + D_t\rho_0\boldsymbol{v} = D_t[\rho_0\boldsymbol{v}]\,.$$

Substituting into the balance of linear momentum yields

$$D_t[\rho_0\boldsymbol{v}] = \mathrm{Div}\boldsymbol{P} + \boldsymbol{B} + [\mathrm{Div}\boldsymbol{R} + R_0]\boldsymbol{v}\,,$$
$$\text{where } \mathrm{Div}(\boldsymbol{R})\boldsymbol{v} = \mathrm{Div}(\boldsymbol{v}\otimes\boldsymbol{R}) - \mathrm{Grad}\boldsymbol{v}\cdot\boldsymbol{R}\,.$$

Finally, the volume specific material balance of linear momentum is given by

$$\boldsymbol{L_0} = \rho_0 \boldsymbol{L} = D_t[\rho_0 \boldsymbol{v}] = \mathrm{Div}[\boldsymbol{P} + \boldsymbol{v} \otimes \boldsymbol{R}] + \boldsymbol{B} + R_0 \boldsymbol{v} - \mathrm{Grad}\boldsymbol{v} \cdot \boldsymbol{R}\,.$$

The mass specific version is obtained by firstly multiplying the balance of mass by the velocity:

$$\boldsymbol{v} D_t \rho_0 = \mathrm{Div}(\boldsymbol{v} \otimes \boldsymbol{R}) - \mathrm{Grad}\boldsymbol{v} \cdot \boldsymbol{R} + \boldsymbol{v} R_0$$

and then subtracting it from the volume specific balance of linear momentum, resulting in

$$D_t[\rho_0 \boldsymbol{v}] - \boldsymbol{v} D_t \rho_0 = \mathrm{Div}\boldsymbol{P} + \boldsymbol{B}\,. \tag{4.10}$$

Substituting

$$D_t[\rho_0 \boldsymbol{v}] - \boldsymbol{v} D_t \rho_0 = \rho_0 D_t \boldsymbol{v}$$

into equation 4.10 yields the mass specific linear momentum balance given by

$$\boldsymbol{L}(t) = \rho_0 D_t \boldsymbol{V} = \mathrm{Div}\boldsymbol{P} + \boldsymbol{B}\,.$$

Balance of internal energy

The volume specific balance of internal energy, is equivalent to the closed system balance of energy with the open system contributions added. The open system contribution is the energy due to the mass flux and source. This is given by

$$D_t(E_0) = -\mathrm{Div}(\boldsymbol{Q} + E\boldsymbol{R}) + Q_0 + ER_0 - \mathrm{Grad}E \cdot \boldsymbol{R} + \boldsymbol{P} : \dot{\boldsymbol{F}}\,.$$

The mass specific version of the balance relation is obtained as before. The balance of mass is weighted by the energy E :

$$E D_t \rho_0 = \mathrm{Div}(\boldsymbol{R})E + ER_0\,,$$

which can be expanded to

$$E D_t \rho_0 = \mathrm{Div}(E\boldsymbol{R}) - \mathrm{Grad}E \cdot \boldsymbol{R} + ER_0\,.$$

Subtracting the weighted balance of mass from the volume specific balance of energy results in the mass specific version of the balance of internal energy, given by

$$\rho_0 D_t E = -\mathrm{Div}\boldsymbol{Q} + Q_0 + \boldsymbol{P} : \dot{\boldsymbol{F}}\,. \tag{4.11}$$

Balance of entropy

The volume specific version of the open system is again equivalent to the closed system with the added open system contributions.

The second law of thermodynamics (see equation 4.6) can be rewritten to make the entropy the subject of the formula:

$$\gamma_0(t) = D_t S + \mathrm{Div}\boldsymbol{H} - H_0 \geq 0 \Rightarrow D_t S = \gamma_0(t) - \mathrm{Div}\boldsymbol{H} + H_0\,.$$

Including the open system contributions due to the mass flux and source, result in the volume specific formulation of the entropy

$$D_t S_0 = \mathrm{Div}(-\boldsymbol{H} + S\boldsymbol{R}) + H_0 + SR_0 - \mathrm{Grad}(S) \cdot \boldsymbol{R} + \gamma_0\,.$$

The mass specific version is determined by subtracting the balance of mass weighted by the entropy,

$$SD_t\rho_0 = \mathrm{Div}(\boldsymbol{R})S + SR_0\,,$$

from the volume specific version of the balance of entropy yielding

$$SD_t\rho_0 = \mathrm{Div}(S\boldsymbol{R}) + SR_0 - \mathrm{Grad}(S)\cdot\boldsymbol{R}\,.$$

Using

$$D_t(S_0) = SD_t\rho_0 + \rho_0 D_t S\,,$$

yields

$$D_t(S_0) - \rho_0 D_t S = \mathrm{Div}(S\boldsymbol{R}) + SR_0 - \mathrm{Grad}(S)\cdot\boldsymbol{R}\,.$$

Finally, subtracting the weighted balance of mass from the volume specific formulation, renders the mass specific version of the balance of entropy, given by

$$\rho_0 D_t S = -\mathrm{Div}(\boldsymbol{H}) + H_0 + \gamma_0(t)\,.$$

To introduce the Clausius-Duhem inequality for an open system, two new quantities are required to account for the open system interactions with the surroundings. The new quantities are the "extra entropy flux" $\tilde{\boldsymbol{S}}$ and the "extra entropy source" $\tilde{S}_0$ The relationship between the rate of entropy input and the heat flux and sources for the open system is now given by

$$\boldsymbol{H} = \frac{\boldsymbol{Q}}{\theta} + \tilde{\boldsymbol{S}} \qquad \text{and} \qquad H_0 = \frac{Q_0}{\theta} + \tilde{S}_0\,. \tag{4.12}$$

The dissipation rate D_{int}, which is the entropy production weighted by the absolute temperature θ, is defined by

$$D_{\mathrm{int}} := \theta\Gamma \geq 0\,.$$

From Section 4.2.1 the temperature weighted dissipation rate is given by

$$D_{\mathrm{int}} = \theta\rho_0 D_t S + \mathrm{Div}(\boldsymbol{H})\theta - H_0\theta \geq 0\,.$$

Substituting the relations from equation 4.12 yields

$$D_{\mathrm{int}} = \theta\rho_0 D_t S + \mathrm{Div}(\frac{\boldsymbol{Q}}{\theta} + \tilde{\boldsymbol{S}})\theta - (\frac{Q_0}{\theta} + \tilde{S}_0)\theta \geq 0\,.$$

Grouping terms and expanding the relation yields

$$\begin{aligned} D_{\mathrm{int}} &= \theta\rho_0 D_t S + \mathrm{Div}(\frac{\boldsymbol{Q}}{\theta})\theta - Q_0 + [\mathrm{Div}\tilde{\boldsymbol{S}} - \tilde{S}_0]\theta \geq 0\,, \\ &= \theta\rho_0 D_t S + \mathrm{Div}\boldsymbol{Q} - Q_0 - \frac{1}{\theta}\boldsymbol{Q}\cdot\mathrm{Grad}\theta + [\mathrm{Div}\tilde{\boldsymbol{S}} - \tilde{S}_0]\theta \geq 0\,. \end{aligned}$$

Making use of the relation from the balance of internal energy (4.11) gives

$$\mathrm{Div}\boldsymbol{Q} - Q_0 = \boldsymbol{P} : \dot{\boldsymbol{F}} - \rho_0 D_t E \qquad \text{and} \qquad \frac{1}{\theta}\mathrm{Grad}\theta = \mathrm{Grad}(\ln\theta)$$

which results in the expression

$$D_{\text{int}} = \theta\rho_0 D_t S + \boldsymbol{P} : \dot{\boldsymbol{F}} - \rho_0 D_t E - \boldsymbol{Q} \cdot \text{Grad}(\ln\theta) + [\text{Div}\tilde{\boldsymbol{S}} - \tilde{S}_0]\theta \geq 0\,.$$

The Helmholtz free energy $\Psi(\rho_0, \theta, \boldsymbol{F})$ is now introduced through the Legendre Transformation

$$\Psi = E - S\theta\,.$$

The density weighted time-rate of change of the free energy is given by

$$\rho_0\dot{\Psi} = \rho_0\left[D_t E - D_t(S)\theta - S D_t\theta\right]\,.$$

Substituting this into the dissipation rate relation gives

$$D_{\text{int}} = -\rho_0\dot{\Psi} - \rho_0 S D_t\theta + \boldsymbol{P} : \dot{\boldsymbol{F}} - \boldsymbol{Q} \cdot \text{Grad}(\ln\theta) + [\text{Div}\tilde{\boldsymbol{S}} - \tilde{S}_0]\theta \geq 0\,.$$

From now on, only the isothermal case is considered. The time-rate of change of the free energy $\Psi = \Psi(\rho_0, \boldsymbol{F})$ is therefore given by the chain rule as

$$\dot{\Psi} = D_{\rho_0}\Psi D_t\rho_0 + D_{\boldsymbol{F}} : \Psi\dot{\boldsymbol{F}}\,.$$

Finally, the dissipation rate for an open system is therefore given by

$$D_{\text{int}} = -\rho_0 D_{\rho_0}\Psi[\text{Div}\boldsymbol{R} - R_0] + [\boldsymbol{P} - \rho_0 D_{\boldsymbol{F}}\Psi] : \dot{\boldsymbol{F}} + [\text{Div}\tilde{\boldsymbol{S}} - \tilde{S}_0]\theta \geq 0\,.$$

Summary of balance relations for a open system in the material description, mass specific

The governing relations of the open-system formulation are summarised in Table 4.2.

Table 4.2: Summary governing equations for a open system (local form, reference configuration,mass specific)

Balance of mass:	$D_t\rho_0 = D_t(J\rho) = \text{Div}\boldsymbol{R} + R_0$
Balance of linear momentum:	$\boldsymbol{L} = \rho_0 D_t\boldsymbol{V} = \text{Div}\boldsymbol{P} + \boldsymbol{B}$
Balance of internal energy:	$\rho_0 D_t E = \boldsymbol{P} : \dot{\boldsymbol{F}} - \text{Div}\boldsymbol{Q} + Q_0$
Balance of entropy:	$\gamma(t) = \rho_0 D_t S(\boldsymbol{X}, t) + \text{Div}\boldsymbol{H} - H_0$
Dissipation inequality:	$D_{\text{int}} = \theta\rho_0 D_t S + \text{Div}(\frac{\boldsymbol{Q}}{\theta})\theta - Q_0\theta + [\text{Div}\tilde{\boldsymbol{S}} - \tilde{S}_0]\theta \geq 0$
	$D_{\text{int}} = -\rho_0 D_{\rho_0}\Psi[\text{Div}\boldsymbol{R} - R_0] + [\boldsymbol{P} - \rho_0 D_{\boldsymbol{F}}\Psi] : \dot{\boldsymbol{F}} + [\text{Div}\tilde{\boldsymbol{S}} - \tilde{S}_0]\theta \geq 0$

Constitutive relations

Now that the open system relations have been formulated, the constitutive relations for bone can be determined. The Helmholtz free energy for bone is chosen as a Neo-Hookean energy, weighted by the relative density to a positive power (Kuhl and Steinmann, 2003). Recall from Section 2.2 in Chapter 2, that the material properties of a porous structure were found to depend on the relative density and the solid properties. The relative density is the ratio of the current density ρ_0 to the initial reference density ρ_0^*. The exponent n, captures the material porosity and is determined empirically (Gibson, 2005). The free energy thus takes the following form:

$$\Psi = \Psi(\boldsymbol{F}, \rho_0) = \left[\frac{\rho_0}{\rho_0^*}\right]^n \tilde{\Psi}^{neo} \text{ where } 1 \leq n \leq 3.5\,.$$

The weighted Neo-Hookean free energy $\tilde{\Psi}^{neo}$ is given by

$$\tilde{\Psi}^{neo} = \frac{1}{\rho_0}\Psi^{neo}\,,$$

where the standard compressible Neo-Hookean free energy,

$$\Psi^{neo} = \frac{1}{2}\lambda \ln^2 J + \frac{1}{2}\mu\left[\boldsymbol{C} : \boldsymbol{I} - 3 - 2\ln J\right]\,,$$

where λ and μ are the Lamé constants. Thus the mass specific free energy is given by

$$\Psi = \left[\frac{\rho_0}{\rho_0^*}\right]^n \frac{1}{\rho_0}\Psi^{neo}\,.$$

The constitutive relations are determined from the dissipation inequality

$$D_{\text{int}} = -\rho_0 \frac{\partial \Psi}{\partial \rho_0}[\text{Div}\boldsymbol{R} - R_0] + [\boldsymbol{P} - \rho_0 \frac{\partial \Psi}{\partial \boldsymbol{F}}] : \dot{\boldsymbol{F}} + [\text{Div}\tilde{\boldsymbol{S}} - \tilde{S}_0]\theta \geq 0\,, \tag{4.13}$$

where

$$D_t\Psi = \frac{\partial \Psi}{\partial \rho_0} D_t\rho_0 + \frac{\partial \Psi}{\partial \boldsymbol{F}} : \dot{\boldsymbol{F}}\,.$$

Each term in the inequality needs to be non-negative. A hyperelastic relation for the first Piola-Kirchhoff stress tensor is therefore given by

$$\boldsymbol{P} = \rho_0 \frac{\partial \Psi}{\partial \boldsymbol{F}}\,.$$

In order to obtain the constitutive relations for the flux and source terms, the derivative of the free energy with respect to the density is required, that is

$$\begin{aligned}
\frac{\partial \Psi}{\partial \rho_0} &= [n-1]\left[\frac{\rho_0}{\rho_0^*}\right]^{n-2}\left[\frac{1}{\rho_0^*}\right]^2 \Psi^{neo} \text{ with } \Psi^{neo} = \rho_0\tilde{\Psi}^{neo} \\
&= [n-1]\frac{1}{\rho_0}\left[\frac{\rho_0}{\rho_0^*}\right]^n \tilde{\Psi}^{neo} \\
&= [n-1]\frac{1}{\rho_0}\Psi\,.
\end{aligned}$$

An appropriate assumption for the mass flux vector $\boldsymbol{R}$ is one analogous to Fick's law of concentrations or Fourier's law of heat conduction (Kuhl and Steinmann, 2003):

$$\boldsymbol{R} = K_0 \,\text{Grad}\,\rho_0\,. \tag{4.14}$$

The mass flux thus depends on the density gradient weighted by a mass conduction coefficient K_0 (with dimensions length squared over time). To satisfy the dissipation inequality, the extra entropy flux vector is defined by

$$\tilde{\boldsymbol{S}} = [n-1]\Psi\frac{1}{\theta}\boldsymbol{R} = [n-1]\Psi\frac{1}{\theta}K_0 \,\mathrm{Grad}\,\rho_0\,.$$

The mass source terms follows from the formulations set out by Harrigan et al. (1996) as

$$R_0 = c\left[\left[\frac{\rho_0}{\rho_0^*}\right]^{-m}\Psi_0 - \Psi_0^*\right], \tag{4.15}$$

where $\Psi_0 = \rho_0\Psi$ and $m > n$. Ψ_0^* is the attractor state stimulus, i.e. the reference free energy which the system is driving towards. The parameter c has dimensions of time divided by length squared, and governs the speed of the remodelling process (Kuhl et al., 2003).

The definition for the extra entropy source $\tilde{S}_0$ follows from the dissipation inequality as

$$\tilde{S}_0 = -[n-1]\Psi\frac{1}{\theta}\,R_0 = -[n-1]\,\Psi\frac{1}{\theta}\,c\left[\left[\frac{\rho_0}{\rho_0^*}\right]^{-m}\Psi_0 - \Psi_0^*\right].$$

Summary of the open system in the material description, mass specific

The governing equations and constitutive relations are summarised in Table 4.3.[2]

Table 4.3: Summary of governing equations for a open system (local form, reference configuration,mass specific)

governing equations		
Balance of mass:	$D_t\rho_0 = D_t[J\rho] = \mathrm{Div}\boldsymbol{R} + R_0$	$[\mathrm{kg\,m^{-3}\,s^{-1}}]$
Balance of linear momentum:	$\boldsymbol{L} = \rho_0 D_t\boldsymbol{V} = \mathrm{Div}\boldsymbol{P} + \boldsymbol{B}$	$[\mathrm{kg\,m^{-2}\,s^{-2}}]$
Balance of internal energy:	$\rho_0 D_t E = \boldsymbol{P} : \dot{\boldsymbol{F}} - \mathrm{Div}\boldsymbol{Q} + Q_0$	$[\mathrm{kg\,m^{-1}\,s^{-3}}]$
Balance of entropy:	$\gamma(t) = \rho_0 D_t S(\boldsymbol{X},t) + Div(\boldsymbol{H}) - H_0$	$[\mathrm{kg\,m^{-1}\,s^{-3}\,K^{-1}}]$
constitutive relations		
first Piola-Kirchhoff stress :	$\boldsymbol{P} = \rho_0 D_{\boldsymbol{F}}\Psi$	$[\mathrm{kg\,m^{-1}\,s^{-2}}]$
mass flux:	$\boldsymbol{R} = K_0\mathrm{Grad}(\rho_0)$	$[\mathrm{kg\,m^{-2}\,s^{-1}}]$
mass source:	$R_0 = c\left[\left[\frac{\rho_0}{\rho_0^*}\right]^{-m}\Psi_0 - \Psi_0^*\right]$	$[\mathrm{kg\,m^{-3}\,s^{-1}}]$
extra entropy flux:	$\tilde{\boldsymbol{S}} = [n-1]\Psi\frac{1}{\theta}\boldsymbol{R}$	$[\mathrm{kg\,s^{-3}}]$
extra entropy source:	$\tilde{S}_0 = -[n-1]\Psi\frac{1}{\theta}\,R_0$	$[\mathrm{kg\,m^{-1}\,s^{-3}\,K^{-1}}]$

[2] Waffenschmidt et al. (2012) proposed a time evolution in days, which is a physiologically meaningful time unit when considering bone remodelling. The only changes from the SI units are that the time-step size and end time of a simulation now have the units of days and the units of the density evolution velocity, the factor c, change to $\left[\mathrm{d\,m^{-2}}\right]$ and finally, the density conduction coefficient K_0 units change to $\left[\mathrm{m^2\,d^{-1}}\right]$

4.3 Relative density as the primary variable

Before aspects of numerical modelling are introduced, the governing equations are modified such that the relative density $\tilde{\rho_0}$ is introduced as the primary variable. This was suggested by Kuhl and Steinmann (2003) to avoid an ill-conditioned problem. The relative density is dimensionless. Negative values indicate bone resorption and positive values bone apposition that is:

$$\tilde{\rho_0} = \frac{\rho_0 - \rho_0^*}{\rho_0^*} \begin{cases} -1 \leq \tilde{\rho_0} \leq 0 \text{ resorption} \\ 0 < \tilde{\rho_0} \leq \infty \text{ absorption} \end{cases} .$$

The remodelling approach is isotropic and the initial density distribution ρ_0^* is uniform throughout the body. This means that $\text{Grad}\rho_0^* = 0$. The governing equations are formulated in terms of $\tilde{\rho_0}$ in the following sections.

4.3.1 Free energy

The free energy is easily parametrised by the relative density as follows:

$$\Psi(\rho_0, \boldsymbol{F}) = \left[\frac{\rho_0}{\rho_0^*}\right]^n \frac{1}{\rho_0} \Psi^{neo} = \left[\frac{\rho_0}{\rho_0^*}\right]^{n-1} \frac{1}{\rho_0^*} \Psi^{neo}$$

with $\rho_0 = \rho_0^*[\tilde{\rho_0} + 1]$. The free energy therefore yields

$$\Psi(\tilde{\rho_0}, \boldsymbol{F}) = [\tilde{\rho_0} + 1]^{n-1} \frac{1}{\rho_0^*} \Psi^{neo} .$$

4.3.2 Balance of mass

Introducing the relative density in the balance of mass relation (4.8) yields

$$D_t \tilde{\rho_0} = D_t \left[\frac{\rho_0 - \rho_0^*}{\rho_0^*}\right] = \frac{1}{\rho_0^*} D_t \rho_0 = \frac{1}{\rho_0^*} [\text{Div}\boldsymbol{R} + R_0] .$$

The mass flux term (4.14) is modified as follows

$$\frac{1}{\rho_0^*} \boldsymbol{R} = \frac{1}{\rho_0^*} K_0 \text{Grad}\rho_0 = K_0 \text{Grad}\tilde{\rho_0} + 1 = K_0 \text{Grad}\tilde{\rho_0} \text{ as } \rho_0^* \text{ is uniform.}$$

The mass flux is therefore given by

$$\frac{1}{\rho_0^*} \boldsymbol{R}(\rho_0) \equiv \boldsymbol{R}(\tilde{\rho_0}) = K_0 \text{Grad}\tilde{\rho_0} .$$

The mass source term (4.15) is expressed in terms of the relative density by

$$\frac{1}{\rho_0^*} R_0[\rho_0] = \frac{c}{\rho_0^*} \left[\left[\frac{\rho_0}{\rho_0^*}\right]^{-m} \Psi_0(\rho_0, \boldsymbol{F}) - \Psi_0^*\right] = \frac{c}{\rho_0^*} \left[[\tilde{\rho_0} + 1]^{-m} \Psi_0(\tilde{\rho_0}) - \Psi_0^*\right] = R_0(\tilde{\rho_0}) .$$

The balance of mass with the relative density as the primary variable thus takes the form

$$\begin{aligned} D_t \tilde{\rho_0} &= \text{Div}[\boldsymbol{R}(\tilde{\rho_0})] + R_0(\tilde{\rho_0}) \\ &= \text{Div}[K_0 \text{ Grad}\tilde{\rho_0}] + \frac{c}{\rho_0^*} \left[[\tilde{\rho_0} + 1]^{-m} \Psi_0(\tilde{\rho_0}, \boldsymbol{F}) - \Psi_0^*\right] . \end{aligned}$$

4.3.3 Balance of linear momentum

The balance of momentum (equilibrium equation) is given by

$$\mathrm{Div}\boldsymbol{P} = \boldsymbol{0} \tag{4.16}$$

$$\text{with } \boldsymbol{P}(\rho_0) = \rho_0 \frac{\partial \Psi(\rho_0, \boldsymbol{F})}{\partial \boldsymbol{F}} \,.$$

Changing the parameterisation of the first Piola-Kirchhoff stress tensor to the relative density results in the following constitutive relation

$$\boldsymbol{P}(\tilde{\rho_0}) = \rho_0^* \left[\tilde{\rho_0} + 1\right] \frac{\partial \Psi(\tilde{\rho_0}, \boldsymbol{F})}{\partial \boldsymbol{F}} \,.$$

4.3.4 Summary

A summary of the governing equations and constitutive relations with $\tilde{\rho_0}$ as the primary variable is given in Table 4.4.

Table 4.4: Summary of the governing equations with the relative density $\tilde{\rho_0}$ as the primary variable.

governing equations:	
Balance of mass	$D_t\tilde{\rho_0} = \mathrm{Div}\left(\boldsymbol{R}(\tilde{\rho_0})\right) + R_0(\tilde{\rho_0})$
Balance of linear momentum	$\mathrm{Div}\left(\boldsymbol{P}(\tilde{\rho_0})\right) = \boldsymbol{0}$
constitutive relations:	
mass specific free energy	$\Psi(\tilde{\rho_0}, \boldsymbol{F}) = \left[\tilde{\rho_0} + 1\right]^{n-1} \frac{1}{\rho_0^*} \Psi^{neo}$
mass flux	$\boldsymbol{R}\left(\tilde{\rho_0}\right) = K_0 \mathrm{Grad}\tilde{\rho_0}$
mass source	$R_0\left(\tilde{\rho_0}\right) = \frac{c}{\rho_0^*}\left[\left[\tilde{\rho_0} + 1\right]^{-m} \Psi_0(\tilde{\rho_0}, \boldsymbol{F}) - \Psi_0^*\right]$
first Piola-Kirchoff stress tensor	$\boldsymbol{P}(\tilde{\rho_0}) = \rho_0^* \left[\tilde{\rho_0} + 1\right] \frac{\partial \Psi(\tilde{\rho_0}, \boldsymbol{F})}{\partial \boldsymbol{F}}$

5

Numerical modelling

It is generally not possible to compute analytical solutions for all but the simplest boundary value problems. Numerical methods, such as the finite element method are commonly employed to approximately solve complex engineering problems. As the name suggests, the domain of interest is subdivided into small sections called elements. In this dissertation, the finite element method is applied to the continuum formulation of bone. The finite element formulation is based on Kuhl and Steinmann (2003).

Note: the finite element formulations are more conveniently expressed using the density rather than the relative density.

5.1 Strong form

The balance of mass (4.8) and momentum (4.16) in absence of the body forces are the governing equations in the continuum formulation for bone. They are cast into residual statements R^ρ and $\boldsymbol{R^u}$ on the domain Ω_0 as:

$$R^\rho := D_t\rho - R_0 + \mathrm{Div}\boldsymbol{R} = 0\,, \tag{5.1}$$

$$\boldsymbol{R^u} := -\mathrm{Div}\boldsymbol{P} = \boldsymbol{0}\,. \tag{5.2}$$

The boundary $\partial\Omega_0$ is divided into essential pairs $\partial\Omega_0^\rho$ and $\partial\Omega_0^u$, where the density ρ and displacements $\boldsymbol{u}$ are prescribed, respectively, and natural pairs $\partial\Omega_0^R$ and $\partial\Omega_0^T$ where the mas flux and tractions are prescribed respectively. The boundary division is subject to the requirements that

$$\begin{aligned} \partial\Omega_0^\rho \cup \partial\Omega_0^R &= \partial\Omega_0 \quad \text{and} \quad \partial\Omega_0^\rho \cap \partial\Omega_0^R = \emptyset \\ \partial\Omega_0^u \cup \partial\Omega_0^T &= \partial\Omega_0 \quad \text{and} \quad \partial\Omega_0^u \cap \partial\Omega_0^T = \emptyset\,. \end{aligned}$$

The boundary conditions for the density, density flux, displacement and tractions are given by

$$\begin{aligned} \rho &= \bar\rho \quad \text{on } \partial\Omega_0^\rho \times]0, t_{\mathrm{end}}[\\ \boldsymbol{R}\cdot\boldsymbol{N} &= \bar R \quad \text{on } \partial\Omega_0^R \times]0, t_{\mathrm{end}}[\\ \boldsymbol{u} &= \bar{\boldsymbol{u}} \quad \text{on } \partial\Omega_0^u \times]0, t_{\mathrm{end}}[\\ \boldsymbol{P}\boldsymbol{N} &= \bar{\boldsymbol{T}} \quad \text{on } \partial\Omega_0^T \times]0, t_{\mathrm{end}}[\,, \end{aligned}$$

where t_{end} is the total time. The initial condition for the density is given by

$$\rho(\boldsymbol{X}, t=0) = \rho_0^*\,.$$

5.2 Weak form

The residual statements (5.1, 5.2) in the strong form are now cast into the weak form to proceed towards the discretised finite element formulation of the problem. Test functions and trial solutions are introduced in the weak form. These functions are required to be in H^1, which is a function space with square integrable derivatives. A function f, with components $f_i = (f_x, f_y, f_z)$ is square integrable (in L_2) if

$$L_2 = \{f_i | \int_{\Omega_0} f_i^2 \, dV \; < \; \infty\} \, .$$

The H^1 function space is defined as

$$H^1 = \{f_i | \in L_2, \int_{\Omega_0} [\mathrm{Grad} f_i]^2 \, dV \; < \; \infty\} \, .$$

The residua are multiplied by admissible test functions $\delta\rho$ and $\delta\boldsymbol{u}$ with components $\delta\rho$ and δu_i, respectively, and their product integrated over the domain Ω_0. The admissible test functions ρ and $\boldsymbol{u}$ with components ρ and u_i are in the function spaces U_0 and V_0 respectively, which are defined by

$$U_0 = \{\delta\rho(\boldsymbol{X}) | \delta\rho(\boldsymbol{X}) \in H^1, \delta\rho = 0 \text{ on } \partial\Omega_0^\rho\} \quad \text{and} \quad V_0 = \{\delta u_i(\boldsymbol{X}) | \delta u_i(\boldsymbol{X}) \in H^1, \delta u_i = 0 \text{ on } \partial\Omega_0^u\} \, .$$

The restriction means that the test functions vanish on their essential boundaries. The sets of admissible trial solutions are defined by

$$U = \{\rho(\boldsymbol{X}, t) | \rho(\boldsymbol{X}, t) \in H^1, \rho = \bar{\rho} \text{ on } \partial\Omega_0^\rho\} \quad \text{and} \quad V = \{u_i(\boldsymbol{X}, t) | u_i(\boldsymbol{X}, t) \in H^1, u_i = \bar{u} \text{ on } \partial\Omega_0^u\} \, .$$

The weak form of the balance of mass residual G^ρ is given by

$$G^\rho(\rho, \boldsymbol{u}, \delta\rho) = \int_{\Omega_0} \delta\rho D_t\rho \, dV - \int_{\Omega_0} \delta\rho R_0 \, dV - \int_{\Omega_0} \delta\rho \mathrm{Div}\boldsymbol{R} \, dV \; \forall\delta\rho \, .$$

Performing integration by parts on the last term yields

$$\int_{\Omega_0} \delta\rho \mathrm{Div}\boldsymbol{R} \, dV = -\int_{\Omega_0} \mathrm{Grad}\delta\rho \cdot \boldsymbol{R} \, dV + \int_{\partial\Omega_0} \delta\rho \boldsymbol{R} \cdot \boldsymbol{N} dS \quad \forall\delta\rho \, .$$

Dividing the boundary into its essential and natural components, with $\delta\rho = 0$ on $\partial\Omega_0^\rho$ and $\boldsymbol{R} \cdot \boldsymbol{N} = \bar{R}$ on $\partial\Omega_0^R$ the weak form of the balance of mass becomes

$$G^\rho(\rho, \boldsymbol{u}, \delta\rho) = \int_{\Omega_0} \delta\rho D_t\rho \, dV - \int_{\Omega_0} \delta\rho R_0 \, dV + \int_{\Omega_0} \mathrm{Grad}\delta\rho \cdot \boldsymbol{R} \, dV - \int_{\partial\Omega_0^R} \delta\rho \bar{R} dS \quad \text{for all} \delta\rho \, . \quad (5.3)$$

The weak form of the balance of linear momentum $\boldsymbol{G}^u$ is given by

$$G^u(\rho, \boldsymbol{u}, \delta\boldsymbol{u}) = -\int_{\Omega_0} \delta\boldsymbol{u} \cdot \mathrm{Div}\boldsymbol{P} \, dV \; \forall\delta\boldsymbol{u} \, .$$

Applying Green's formula yields

$$-\int_{\Omega_0} \delta\boldsymbol{u} \cdot \mathrm{Div}\boldsymbol{P} = \int_{\Omega_0} \mathrm{Grad}\delta\boldsymbol{u} : \boldsymbol{P} \, dV - \int_{\partial\Omega_0} \delta\boldsymbol{u} \cdot [\boldsymbol{P}\boldsymbol{N}] \, dS \; \forall\delta\boldsymbol{u} \, .$$

Dividing the boundary into the essential and natural components, where $\delta\boldsymbol{u} = \boldsymbol{0}$ on $\partial\Omega_0^u$ and $\boldsymbol{P}\boldsymbol{N} = \bar{\boldsymbol{T}}$ on $\partial\Omega_0^T$, the weak form of the balance of linear yields

$$G^u(\rho, \boldsymbol{u}, \delta\boldsymbol{u}) = \int_{\Omega_0} \mathrm{Grad}\delta\boldsymbol{u} : \boldsymbol{P} \, dV - \int_{\partial\Omega_0^T} \delta\boldsymbol{u} \cdot \bar{\boldsymbol{P}} \, dS \; \forall\delta\boldsymbol{u} \, . \quad (5.4)$$

5.3 Time discretisation

The time discretisation is done with the fully-implicit backward Euler method. A time step is defined by $\Delta t = t_{n+1} - t_n$, where t_{n+1} is the next and t_n is the current time. All quantities are known and equilibrium is assumed at t_n.

The time discrete version of the weak form of the balance of mass at t_{n+1} yields

$$G^{\rho}_{n+1}(\rho, \boldsymbol{u}, \delta\rho) = \int_{\Omega_0} \delta\rho \frac{\rho_{n+1} - \rho_n}{\Delta t}\, dV - \int_{\Omega_0} \delta\rho R_{0n+1}\, dV + \int_{\Omega_0} \mathrm{Grad}\delta\rho \cdot \boldsymbol{R}_{n+1}\, dV - \int_{\partial\Omega_0^R} \delta\rho \bar{R}_{n+1}\, dS \;\forall \delta\rho\,.$$

Similary, the time discretised weak form of the balance of linear momentum results in

$$G^{u}(\rho, \boldsymbol{u}, \delta\boldsymbol{u})_{n+1} = \int_{\Omega_0} \mathrm{Grad}\delta\boldsymbol{u} : \boldsymbol{P}_{n+1} - \int_{\partial\Omega_0^T} \delta\boldsymbol{u} \cdot \bar{\boldsymbol{T}}_{n+1}\, dS \,\forall \delta\boldsymbol{u}\,.$$

5.4 Linearisation

The non-linear coupled system of equations (5.3, 5.4) can be solved by reducing the problem to a linear system, which is solved iteratively to approximate the full problem. The coupled problem (5.3,5.4) is solved monolithically and a Newton-Raphson technique used as the iterative solution strategy. This is done at each time step. For clarity the subscript $n+1$ is dropped henceforth.

In general, a new residual statement $\boldsymbol{R}^{k+1}$ for the next Newton iteration at each time step is expressed as

$$\boldsymbol{R}^{k+1}(\boldsymbol{d}) = \boldsymbol{R}^k + d\boldsymbol{R} \doteq 0 \text{ where } d\boldsymbol{R} = \frac{\partial \boldsymbol{R}^k}{\partial \boldsymbol{d}} \Delta\boldsymbol{d}$$

where $\boldsymbol{R}^k$ is the residual from the previous Newton iteration k, $d\boldsymbol{R}$ is the directional derivative of $\boldsymbol{R}$ at $\boldsymbol{d}^k$ in the direction of the increment $\Delta\boldsymbol{d}$. The directional derivative is equivalent to the expression

$$d\boldsymbol{R} = \frac{\partial}{\partial \epsilon}\left[\boldsymbol{R}(\boldsymbol{d}^k + \epsilon\Delta\boldsymbol{d})\right]\,, \tag{5.5}$$

where $\epsilon \ll 1$ is a scalar. The term $\frac{\partial \boldsymbol{R}^k}{\partial \boldsymbol{d}}$ is referred to as the tangent matrix of $\boldsymbol{R}$ at $\boldsymbol{d}^k$.

The new solution $\boldsymbol{d}^{k+1}$ is determined from

$$\boldsymbol{d}^{k+1} = \boldsymbol{d}^k + \Delta\boldsymbol{d}\,.$$

For the coupled system (5.3, 5.4) the residual $\boldsymbol{R}$ consists of the residual for the balance of mass equation R^{ρ} and the residual of the balance of linear momentum $\boldsymbol{R}^u$. The linearisation of

$$\boldsymbol{R}(\boldsymbol{d}) = \begin{bmatrix} R^{\rho}(\rho) \\ \boldsymbol{R}^u(\boldsymbol{u}) \end{bmatrix}$$

is done as follows

$$R^{\rho}_{k+1} = R^{\rho}_k + dR^{\rho} \doteq 0\,, \tag{5.6}$$

$$\boldsymbol{R}^u_{k+1} = \boldsymbol{R}^u_k + d\boldsymbol{R}^u \doteq \boldsymbol{0}\,. \tag{5.7}$$

The directional derivatives are determined in the direction of

$$\boldsymbol{d} = \begin{bmatrix} \rho \\ \boldsymbol{u} \end{bmatrix}$$

for the first residual statement(5.6) by

$$dR^\rho = \frac{\partial R^\rho_k}{\partial \rho}\Delta\rho + \frac{\partial R^\rho_k}{\partial \boldsymbol{u}}\Delta\boldsymbol{u}\,,$$

and using equation (5.5)

$$= \frac{\partial}{\partial\epsilon}\left[R^\rho_k(\rho+\epsilon\Delta\rho,\boldsymbol{u})\right]|_{\epsilon=0} + \frac{\partial}{\partial\epsilon}\left[R^\rho_k(\rho,u+\epsilon\Delta\boldsymbol{u})\right]|_{\epsilon=0}\,.$$

This yields

$$\begin{aligned} dR^\rho = &\int_{\Omega_0}\left[\delta\rho\frac{\Delta\rho}{\Delta t} - \delta\rho\frac{\partial R_0}{\partial\rho}\Delta\rho - \mathrm{Grad}\delta\rho\cdot K_0\mathrm{Grad}\Delta\rho\right]\,dV \\ &- \int_{\Omega_0}\delta\rho\frac{\partial R_0}{\partial\boldsymbol{F}} : \mathrm{Grad}\Delta\boldsymbol{u}\,dV\,. \end{aligned}$$

The directional derivative for the second residual (5.7) is given by

$$d\boldsymbol{R}^u = \frac{\partial R^u_k}{\partial\rho}\Delta\rho + \frac{\partial R^u_k}{\partial\boldsymbol{u}}\Delta\boldsymbol{u}\,.$$

The directional derivatives are therefore determined by

$$d\boldsymbol{R}^u = \int_{\Omega_0}\mathrm{Grad}\delta\boldsymbol{u} : \frac{\partial}{\partial\epsilon}\boldsymbol{P}(\rho+\epsilon\Delta\rho,\boldsymbol{u})|_{\epsilon=0}\,dV + \int_{\Omega_0}\mathrm{Grad}\delta\boldsymbol{u} : \frac{\partial}{\partial\epsilon}\boldsymbol{P}(\rho,\boldsymbol{u}+\epsilon\Delta\boldsymbol{u})|_{\epsilon=0}\,dV\,.$$

The directional derivative of the displacement problem 5.7 is given by

$$d\boldsymbol{R}^u = \int_{\Omega_0}\mathrm{Grad}\delta\boldsymbol{u}\cdot\frac{\partial\boldsymbol{P}}{\partial\rho}\Delta\rho\,dV + \int_{\Omega_0}\mathrm{Grad}\delta\boldsymbol{u} : \frac{\partial\boldsymbol{P}}{\partial\boldsymbol{F}} : \mathrm{Grad}\Delta\boldsymbol{u}\,dV\,.$$

5.5 Spatial discretisation

The finite element method is now described. The reference domain, which can have an arbitrary shape or size, is subdivided into a number of elements as

$$\Omega_0 \approx \bigcup_{e=1}^{n_{\mathrm{elm}}}\Omega^e_0\,,$$

where Ω^e_0 is the domain of an element and n_{elm} refers to the number of elements that the domain is divided into, as shown in Figure 5.1.

The Galerkin method is used to spatially discretise the problem.

The global approximation of the density and displacement fields, as well as its respective test functions are given by

$$\begin{aligned}
\rho \approx \rho^h &= \sum_{I=1}^{n_{\mathrm{np}}} N^\rho_I\rho_I & \boldsymbol{u} \approx \boldsymbol{u}^h &= \sum_{J=1}^{n_{\mathrm{np}}} N^u_J\boldsymbol{u}_J \\
\mathrm{Grad}\rho \approx \mathrm{Grad}\rho^h &= \sum_{I=1}^{n_{\mathrm{np}}}\mathrm{Grad}N^\rho_I\rho_I & \mathrm{Grad}\boldsymbol{u} \approx \mathrm{Grad}\boldsymbol{u}^h &= \sum_{J=1}^{n_{\mathrm{np}}}\mathrm{Grad}N^u_J\otimes\boldsymbol{u}_J \\
\Delta\rho \approx \Delta\rho^h &= \sum_{I=1}^{n_{\mathrm{np}}} N^\rho_I\Delta\rho_I & \Delta\boldsymbol{u} \approx \Delta\boldsymbol{u}^h &= \sum_{J=1}^{n_{\mathrm{np}}} N^u_J\boldsymbol{\Delta u}_J \\
\delta\rho \approx \delta\rho^h &= \sum_{I=1}^{n_{\mathrm{np}}} N^\rho_I\delta\rho_I & \delta\boldsymbol{u} \approx \delta\boldsymbol{u}^h &= \sum_{J=1}^{n_{\mathrm{np}}} N^u_J\boldsymbol{\delta u}_J\,,
\end{aligned}$$

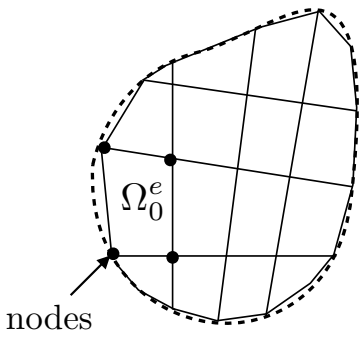

Fig. 5.1: Finite element discretisation of the domain Ω_0 into elements $\Omega_0^e, e = 1 : n_{\text{elm}}$, where n_{elm} is the number of elements. The element nodes are indicated.

where n_{np} are the global nodes. N^ρ and N^u are position dependent shape functions for the density and displacement degrees of freedom respectively and $\rho, \boldsymbol{u}, \delta\rho, \boldsymbol{\delta u}, \Delta\rho$ and $\boldsymbol{\Delta u}$ are the nodal values of the respective quantities. The same shape functions are used for the density and displacements.

The discretised residual statements are detailed below.

$$
\begin{aligned}
R^\rho &= \sum_{I=1}^{n_{\text{np}}} \int_{\Omega_0} N_I^\rho \frac{\rho_{I,n+1} - \rho_{I,n}}{\Delta t}\, dV + \int_{\Omega_0} \text{Grad} N_I^\rho \cdot \boldsymbol{R}_{n+1}\, dV - \int_{\Omega_0} N_I^\rho R_{0n+1}\, dV - \int_{\partial\Omega_0} N_I^\rho \bar{R}_{n+1}\, dS \\
\boldsymbol{R}^u &= \sum_{J=1}^{n_{\text{np}}} \int_{\Omega_0} \text{Grad} N_J^u \cdot \boldsymbol{P}_{n+1}\, dV - \int_{\partial\Omega_0} N_J^u\, \bar{\boldsymbol{T}}_{n+1}\, dS\,,
\end{aligned}
$$

The directional derivatives are discretised as

$$
\begin{aligned}
d R^\rho &= \underbrace{\sum_{I=1}^{n_{\text{np}}} \sum_{K=1}^{n_{\text{np}}} \int_{\Omega_0} \left[N_I^\rho \frac{1}{\Delta t} N_K^\rho - N_I^\rho \frac{\partial R_0}{\partial \rho} N_K^\rho - \text{Grad} N_I^\rho \cdot K_0 \text{Grad} N_K^\rho\, dV \right]}_{K_{\rho\rho}} \Delta\rho_K \\
&\quad - \underbrace{\sum_{I=1}^{n_{\text{np}}} \sum_{L=1}^{n_{\text{np}}} \int_{\Omega_0} \left[N_I^\rho \frac{\partial R_0}{\partial \boldsymbol{F}} \cdot \text{Grad} N_L^u dV \right]}_{K_{\rho u}} \cdot \boldsymbol{\Delta u}_L \\
d\boldsymbol{R}^u &= \underbrace{\sum_{J=1}^{n_{\text{np}}} \sum_{K=1}^{n_{\text{np}}} \int_{\Omega_0} \left[\text{Grad} N_J^u \cdot \frac{\partial \boldsymbol{P}}{\partial \rho} N_K^\rho\, dV \right]}_{K_{\rho u}} \Delta\rho_K \\
&\quad + \underbrace{\sum_{J=1}^{n_{\text{np}}} \sum_{L=1}^{n_{\text{np}}} \int_{\Omega_0} \left[\text{Grad} N_J^u \cdot \frac{\partial \boldsymbol{P}}{\partial \boldsymbol{F}} \cdot \text{Grad} N_L^u\, dV \right]}_{K_{uu}} \cdot \boldsymbol{\Delta u}_L
\end{aligned}
$$

where the components $K_{\rho\rho}, K_{\rho u}, K_{u\rho}$ and K_{uu} make up the global tangent stiffness matrix.

At each time step the following system of equations is solved:

$$
\begin{bmatrix} \Delta\rho \\ \boldsymbol{\Delta u} \end{bmatrix} = - \begin{bmatrix} K_{\rho\rho} & \boldsymbol{K}_{\rho u} \\ \boldsymbol{K}_{u\rho} & \boldsymbol{K}_{uu} \end{bmatrix}^{-1} \begin{bmatrix} R^\rho \\ \boldsymbol{R}^u \end{bmatrix}\,.
$$

5.6 Mesh convergence

When the finite element method is implemented, the element sizes play an important role, as the solution is approximated element-wise. The finer the finite element mesh, the more accurate the solution. To quantify the convergence upon mesh refinement, the L_2 or H^1 norm is determined. The definition of the L_2 and H^1 norms of $\boldsymbol{u}$ is given by

$$||\boldsymbol{u}||_{L_2} = \sqrt{\int_{\Omega_0} \boldsymbol{u} \cdot \boldsymbol{u} \, dV} \qquad \text{and} \qquad ||\boldsymbol{u}||_{H^1} = \sqrt{\int_{\Omega_0} \boldsymbol{u} \cdot \boldsymbol{u} + \text{Grad}\boldsymbol{u} \, : \, \text{Grad}\boldsymbol{u} \, dV}$$

5.7 Approximation of the density

The mass flux is important in the bone remodelling formulation, as it smooths the solution and accounts for size effects present in bone due to the microstructure (Kuhl et al., 2003). The density distribution in bone depends on the size of the bone. Smaller bones have a more uniform density distribution and larger bones exhibit a less dense interior and a denser outer shell (Kuhl, 2004). Kuhl demonstrated that the mass flux captures the size effect of bone.

Given the importance of accounting for mass flux, the density has to be chosen as a function in H^1 and not L_2. This implies that the density can not be condensed out at the element level.

5.8 Aspects of the implementation of the finite element method

Sophisticated open source programs and commercial codes are available to solve PDEs using the finite element method. The Ace library, an extension of Wolfram Mathematica, consisting of the AceGen (Korelc, 2016b) and AceFEM (Korelc, 2016a) libraries, is a commercial tool to implement the finite element method. Most problems that can be solved with the finite element method can be implemented in the hybrid symbolic-numeric based code in the Ace library. The Ace library, made up of two components, facilitates the development of a finite element code, where the AceGen component provides an environment for the code development at element level at a Gauss point and the AceFEM component is a non-linear solver. A great advantage of AceGen is automatic differentiation, which allows for the fast implementation of new constitutive laws. This means that the element tangent matrices, as detailed in section 5.4 can be computed automatically and exactly. This is an efficient and reliable method to solve the problem, as the chances of mistakes are reduced. This is especially relevant in the medical field, where new constitutive laws are regularly developed for the highly complex materials. The theory for bone remodelling, as detailed in the previous sections, is coded in the AceGen environment and the global problem is solved in AceFEM. AceGen generates the source code for an element subroutine. The source code can be generated for different programmes, including AceFEM.

The element code is provided in Appendix A.

6

Validation of numerical model

To validate the finite element model developed in the previous section, the various components have to be validated against benchmarks problems reported in the literature. These include the hyperelastic part and each component of the remodelling model.

6.1 Benchmark problem: the nearly incompressible strip

To validate the hyperelastic component of our finite element model, the benchmark problem reported by Bonet and Wood (2008) is simulated. A two-dimensional strip of size 20 mm $\times$ 20 mm is stretched in the x - direction as shown in Figure 6.1. The total stretch in the x - direction is 3. The material properties of the strip are given in Table 6.1 for plain strain conditions.

The deformed domain is shown in Figure 6.2. The result exactly matches that reported by Bonet and Wood. The hyperelastic component of the code in AceGen is thus validated.

Table 6.1: The material properties of the plane strain nearly incompressible strip (Bonet and Wood, 2008).

property	value	unit
shear modulus $\mu =$	0.4225	Nmm^{-2}
bulk modulus $\kappa =$	5	Nmm^{-2}
Poisson's ratio $\nu =$	0.46	

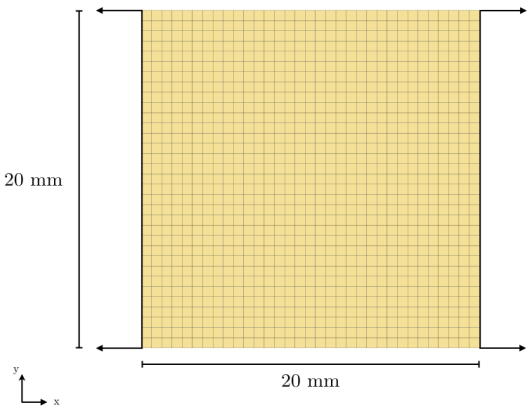

Fig. 6.1: The underformed domain and mesh of the nearly incompressible strip example.

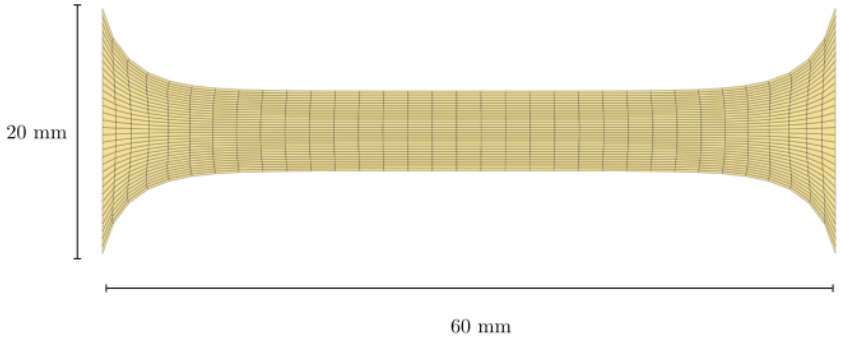

Fig. 6.2: The deformed mesh, after a stretch of 3 was applied in the x - direction.

6.2 Heat equation

The balance of mass 4.8 is analogous to the heat equation given by

$$\rho c D_t \theta = \mathrm{div}(\boldsymbol{K}\mathrm{Grad}\theta) + s\,,$$
$$\text{where } \boldsymbol{K} = k_0 \boldsymbol{I}\,,$$

and θ is the temperature, ρ is the material density, c is the heat capacity, $\boldsymbol{K}$ is the conductivity tensor, where k_0 is the heat conductivity, $\boldsymbol{I}$ is the unit tensor and s is the heat source. To allow a comparison between the two equations, the heat equation, given in Section 4.2.1 in equation 4.7 was also implemented. The same approach as for the density evolution was adopted to implement the heat equation in AceGen. That is, the strong form was developed and then cast into the weak form. The finite element and time discretisation was introduced.

To validate the heat equation, the example reported by Zienkiewicz et al. (2005) was solved. A square plate of dimension 1 m $\times$ 1 m with the boundary conditions illustrated in Figure 6.3 was modelled. All boundaries are of essential type with a prescribed temperature of $\theta = 0$ K. A time-dependent heat source $s(t) = f_0 e^{-\alpha t}$ acts throughout the domain. The material properties are summarised in Table 6.2.

Table 6.2: The material properties and simulation data for the transient linear heat conduction example (Zienkiewicz et al., 2005)

property		value	unit
material density	$\rho =$	1	$\mathrm{kg\,m^{-3}}$
heat capacity	$c =$	1	$N\mathrm{m\,kg^{-1}}K^{-2}$
heat conduction coefficient	$k_0 =$	$\frac{0.75}{\pi^2}$	$W\mathrm{m^{-1}}K^{-1}$
heat source term constant 1	$f_0 =$	1	$N\mathrm{m^{-2}}K^{-1}s^{-1}$
heat source term constant 2	$\alpha =$	1	s^{-1}
time step size	$\Delta t =$	0.01	s
total time	$t =$	4	s
number of elements	$n =$	400	

Owing to the symmetry of the problem, only a quarter of the domain is modelled. The heat flux is set to zero along the symmetry boundaries. The resulting heat distributions at various time steps are shown in Figure 6.4. The results match those reported by Zienkiewicz et al.

The normalised temperature at the centre of the domain over time and the analytical solution reported by Zienkiewicz et al. are shown in Figure 6.5. The numerical results are identical.

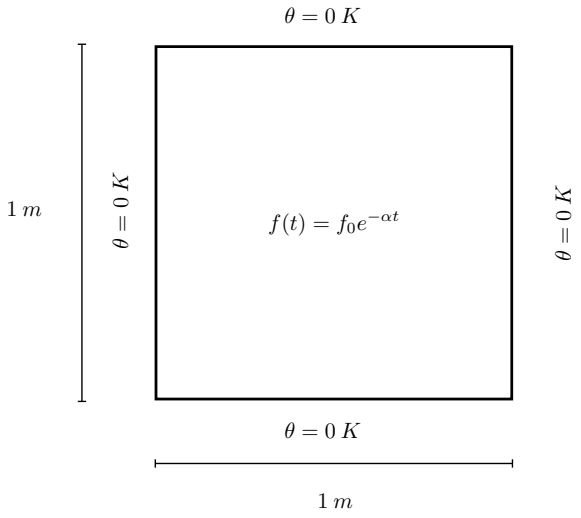

Fig. 6.3: The boundary conditions of the heat equation (Zienkiewicz et al., 2005).

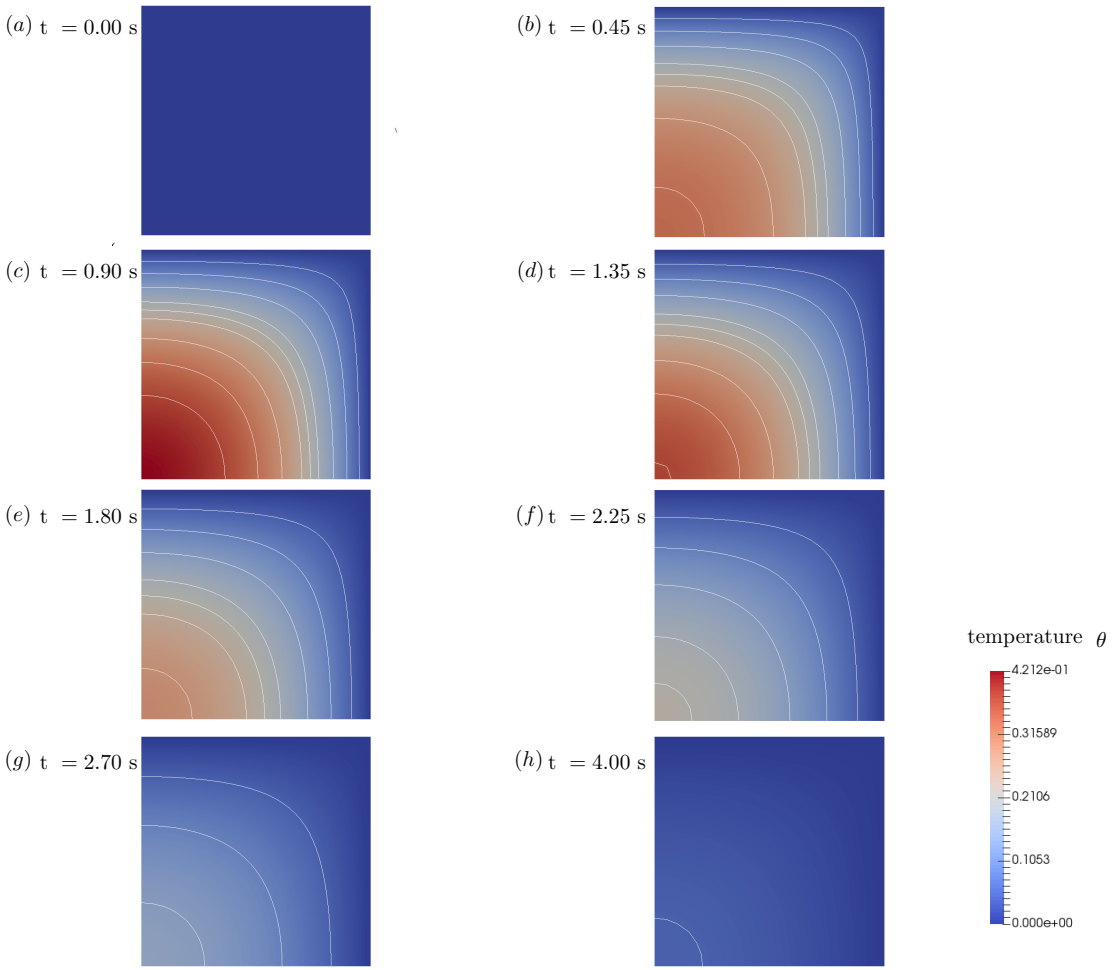

Fig. 6.4: The temperature distribution in a quarter of the domain at various times. The isotherms are shown.

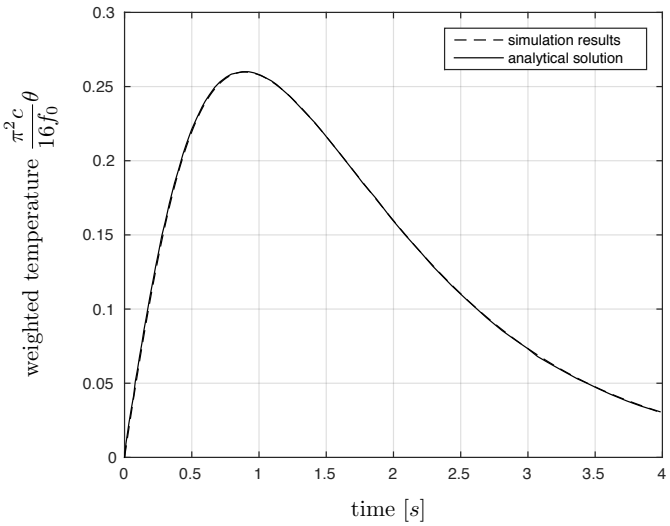

Fig. 6.5: A comparison of the analytical solution for the normalised temperature evolution at the centre of the full domain from (Zienkiewicz et al., 2005) and the simulation results.

6.3 An investigation of the mass source term under uni-axial loading conditions

In this section, we investigate the behaviour of the remodelling model to variations in the mass source. Kuhl and Steinmann (2003) reported on an uni-axial loading problem, where the influence of the mass source is investigated. A specimen is loaded in tension by a time-dependent, piecewise-defined forcing function as shown in Figure 6.6 (a). Waffenschmidt et al. (2012) also applied a piece-wise defined loading scenario to a unit-size specimen as shown in Figure 6.6 (b). Both problems were analysed using the remodelling theory, documented in the previous sections. From now on the model by Kuhl and Steinmann will be, where convenient, referred to as the KS model and the Waffenschmidt et al. model will be referred to as the W model.

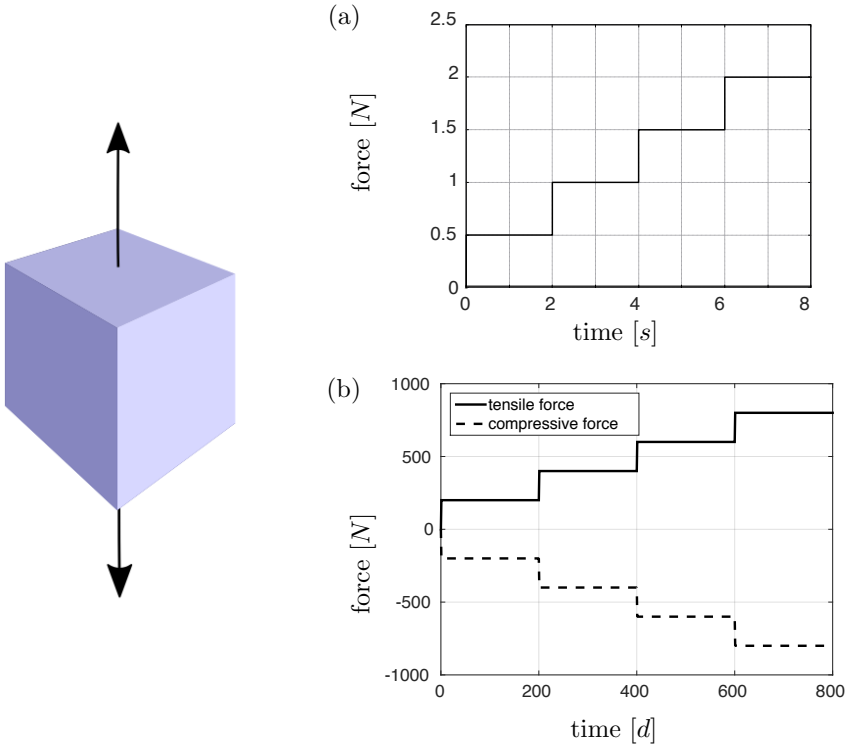

Fig. 6.6: A piece-wise defined forcing function applied to a specimen as defined by (a) Kuhl and Steinmann and (b) Waffenschmidt et al. (2012).

Kuhl and Steinmann chose the material properties and time step units without attaching any physically meaningful values. The aim of this benchmark is to investigate the mass source and the influence of the constitutive parameters on the evolution in uni-axial tension.

Waffenschmidt et al. chose material parameters to match those of the bone in the human tibia. The loading magnitude is larger than that chosen by Kuhl and Steinmann to mimic a realistic load and both tension and compression were considered. The applied force is shown in Figure 6.6 (b). The spatial dimensions were also considered in mm, rather than metres. Finally, the time unit is in days, rather than seconds.

In both cases, the problem is modelled with one element. This is sufficient to capture the model, as the problem is one-dimensional.

The material parameters used in each study are summarised in Table 6.3.

Table 6.3: The constitutive parameters reported by Kuhl and Steinmann (2003) and Waffenschmidt et al. (2012). The Lamé constants relate to the Young's modulus and Poisson's ratio as $\lambda = \frac{E_y \nu}{(1+\nu)(1-2\nu)}$ and $\mu = \frac{E_y}{2(1+\nu)}$.

Property		Kuhl and Steinmann (2003)		Waffenschmidt et al. (2012)	
Young's Modulus	E_y	1	[N m^{-2}]	-	[N mm^{-2}]
1st Lamé constant	λ	-	[N m^{-2}]	2186.0	[N mm^{-2}]
shear modulus	μ	-	[N m^{-2}]	1458.0	[N mm^{-2}]
Poisson's ratio	ν	0	[-]	-	[-]
attractor stimulus	Ψ_0^*	1	[N m^{-2}]	0.0275	[N mm^{-2}]
initial density	ρ_0^*	1	[kg m^{-3}]	1.0	[kg mm^{-3}]
	n	2	[-]	2	[-]
	m	3	[-]	3	[-]
density growth velocity	c	1	[s m^{-2}]	0.4	[d mm^{-2}]
mass conduction coefficient	K_0	0	[m^2 s^{-1}]	0	[mm^2 d^{-1}]

The evolution of the relative density and the displacement history for the Kuhl and Steinmann problem is shown in Figure 6.7. The simulations replicate the results reported by Kuhl and Steinmann perfectly. The density and displacement change abruptly as the initial force and the subsequent step-wise increases of the force are applied and then converge to an equilibrium state. The initial density decrease is related to the choice of material parameters. The attractor stimulus has the greatest influence on the behaviour of the density evolution. This is discussed in the following.

The evolution of the volume specific, density weighted free energy Ψ_0 and the biological stimulus $[\tilde{\rho_0} + 1]^{-m} \Psi_0$ are shown in Figure 6.8. The abrupt changes and the subsequent convergence towards an equilibrium state can yet again be observed. The coupling between the density, displacement and the free energy is also evident. It is important to note that the biological stimulus will always drive towards the attractor stimulus Ψ_0^*, which equals 1 Pa in this example. The other quantities are increasing with an increasing force, as expected.

Figure 6.9 shows a comparison of the remodelling code with a hyper- and linear-elastic code. A comparison between the free energies is shown in Figure 6.9 (a). The density-weighted free energy is much smaller than that of the purely hyper-elastic model. It is initially close to the hyper-elastic counterpart, but then the density weighting results in a very small increase in free energy and the linear-elastic energy continues to increase, as it is only dependent on the force, which is increasing step-wise. When the remodelling is neglected, the model behaves as a Neo-Hookean hyper-elastic material, as expected. The displacement trends are identical to the trends of the free energies, also as expected.

Next, Kuhl and Steinmann investigated the influence of the model parameters. The graphs capturing these analyses are shown in Figure 6.10. First of all, the influence of the material parameters n and

m were considered. These parameters drive the density evolution in the mass source term. When substituting the definition of the volume specific free energy Ψ_0 into the mass source term, it takes the form:

$$R_0 = \frac{c}{\rho_0^*}\left[(\tilde{\rho_0}+1)^{n-m}\,\Psi^{\text{neo}} - \Psi_0^*\right].$$

A decrease in these parameters results in a rapid increase in the density and simultaneously, the rate of convergence to an equilibrium state decreases. This can be seen in Figure 6.10 (a) with the solution for $n = m = 1$, where the convergence rate has significantly decreased. For large values of n and m, the solution converges very quickly, but the density magnitudes are much smaller. This demonstrates that the choice of these two parameters is important and has to be considered carefully.

The influence of the attractor stimulus Ψ_0^* is investigated next, as shown in Figure 6.10 (b). This is a very important parameter. As mentioned earlier, the initial decrease of density is due to the parameter choice, specifically that of the attractor stimulus. There is an inverse relationship between the attractor stimulus and the density. This is explained with the nature of the mass source. As the attractor stimulus is smaller, the increase in density is naturally greater.

Finally, the influence of the time-step size and initial density are investigated, as shown in Figures 6.10 (c) and (d). Neither of the two parameters influence the density evolution significantly. The convergence rate is affected, but the steady state is the same. As the unconditionally stable, implicit backward Euler time scheme is used, it is expected that the solution always converges. However, the accuracy of the solution depends on the time step size. The choice of the initial density should not have major influence on the results, provided that it falls within a reasonable, physically meaningful range. This can be seen in Figure 6.10 (c). When very large values of the initial density are chosen, such as $\rho_0^* = 10$ kg m^{-3} or 100 kg m^{-3}, the solution changes significantly. Similarly, if very small initial values of the density, such as $\rho_0^* = 0.01$ kg m^{-3}, are chosen, it can be seen that the solution is unstable and the density tends to negative infinity. However, if the density is chosen in a reasonable range for bone such as $\rho_0^* = 0.5 - 2.0$ kg m^{-3} the solution is virtually insensitive to the choice of the initial density as shown in Figure 6.10 (c).

Next, the load sensitivity of the problem is considered as shown in Figure 6.11. When no loading is applied, as shown in Figure 6.11 (a), the free energy Ψ_0 does not evolve and the density is driving towards $-\infty$. However, even if a very small load is applied, such as shown in Figure 6.11 (b), where the maximum force is 10^{-3} N, the system is stable. The density does initially decrease very quickly, but then stabilises. If a very large force is applied, e.g. 1000 N, as shown in Figure 6.11 (c), the density and free energy Ψ_0 increase accordingly. The initial density decrease is eliminated when this large force is applied. Therefore the density evolution does not only depend on the choice of the attractor stimulus Ψ_0^*, but also on the magnitude of the load.

The density evolution and displacement history of the Waffenschmidt et al. (2012) problem are shown in Figure 6.12. Owing to the choice of different material parameters and far greater loads, the magnitudes of the densities are far greater than the Kuhl and Steinmann (2003) results. A $\pm$ 350 % final increase in density follows from the larger force, compared to a mere $\pm$ 65 % final increase reported in the Kuhl and Steinmann (2003) paper. However, the same trends are observed. Each quantity changes abruptly and then converges towards an equilibrium value, driving towards the attractor stimulus.

The parameter sensitivity study reported by Waffenschmidt et al. (2012) is conducted with a force 10 % less than initially reported. As demonstrated before, a large force corresponds to a greater increase in density and therefore it is unlikely that resorption will occur. Because the effects of resorption should be investigated, a smaller force is used in the study. The results are shown in Figure 6.13. Here the influence of the load magnitude on the density evolution becomes apparent. A 10 % decrease in force results in a drastic decrease in final density from $\pm$ 350 % to $\pm$ 80 %.

The trends of the influence of various parameters in the Waffenschmidt et al. model are comparable to the results reported by Kuhl and Steinmann (2003). The decrease in the parameters n and m leads to an increase of the density magnitudes and a decrease of the convergence rate as shown in Figure

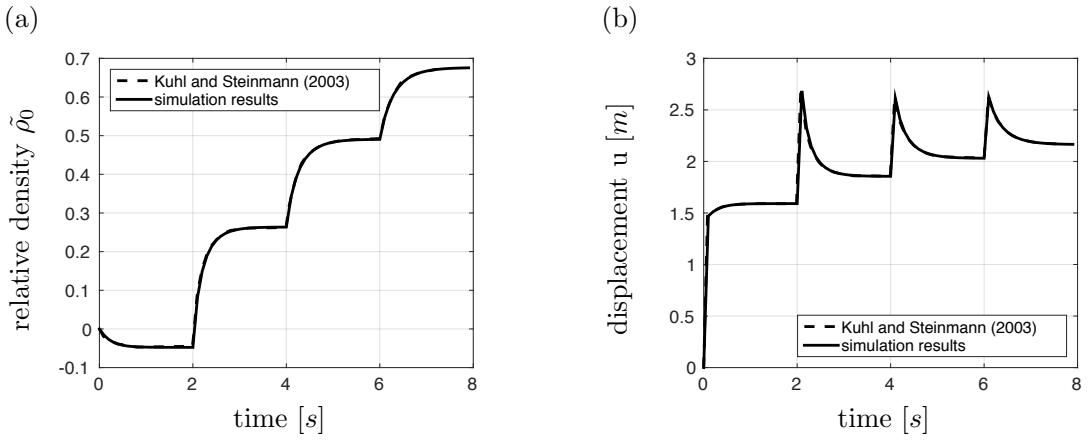

Fig. 6.7: Comparison of the simulated results with those reported by Kuhl and Steinmann (2003). The density evolution is shown in (a) and the displacement history in (b).

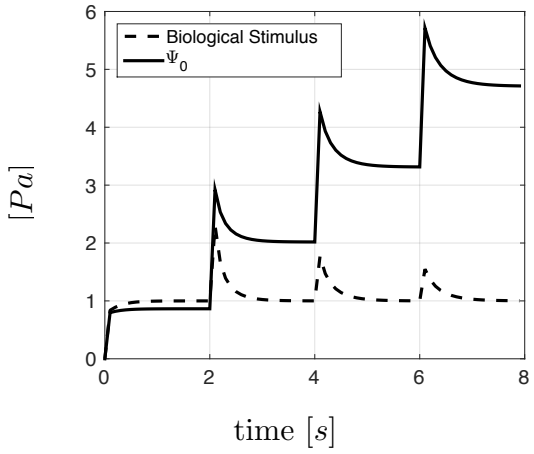

Fig. 6.8: Simulated results of the evolution of the free energy Ψ_0 and the biological stimulus $[\tilde{\rho}_0 + 1]^{-m} \Psi_0$.

6.13 (a). The attractor stimulus Ψ_0^* again proves to have great impact on the problem as shown in Figure 6.13 (b). A larger choice of Ψ_0^* initially drives the density evolution to resorption. For smaller values of Ψ_0^*, the magnitude of the density increases, as expected.

The influence of the remodelling speed c is investigated by Waffenschmidt et al. (2012) as shown in Figure 6.13 (c). This does not have a significant impact on the solution. As the name indicates, it simply has an influence on the rate of convergence. The equilibrium state is always achieved.

Finally, the effect of the initial density is again investigated as shown in Figure 6.13 (d). As detailed above, the initial density does not have a great impact on the problem, provided the choice of the initial density falls within a reasonable margin.

Further, a parameter study on the Waffenschmidt et al. problem with the full magnitude of the force has been conducted, as shown in Figure 6.14. The influence of the density growth velocity c, as shown in Figure 6.14 (b) follows the exact same trend as detailed above for the problem with a 10 % decrease in the force. The investigation of the attractor stimulus Ψ_0^*, as shown in Figure 6.14 (a), is interesting. Smaller values for the attractor stimulus again result in a significant increase of the density. Larger values, however, do not drive the density into the negative region. Rather, convergence

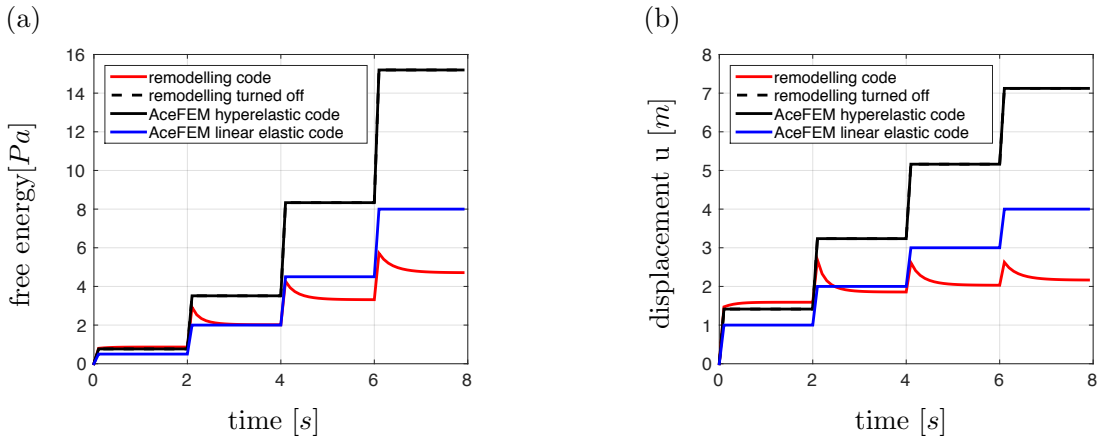

Fig. 6.9: A comparison between the evolutions of the free energies (a) and displacements (b) with time for remodelling and no remodelling, to a Neo-Hookean model and a linear elastic code.

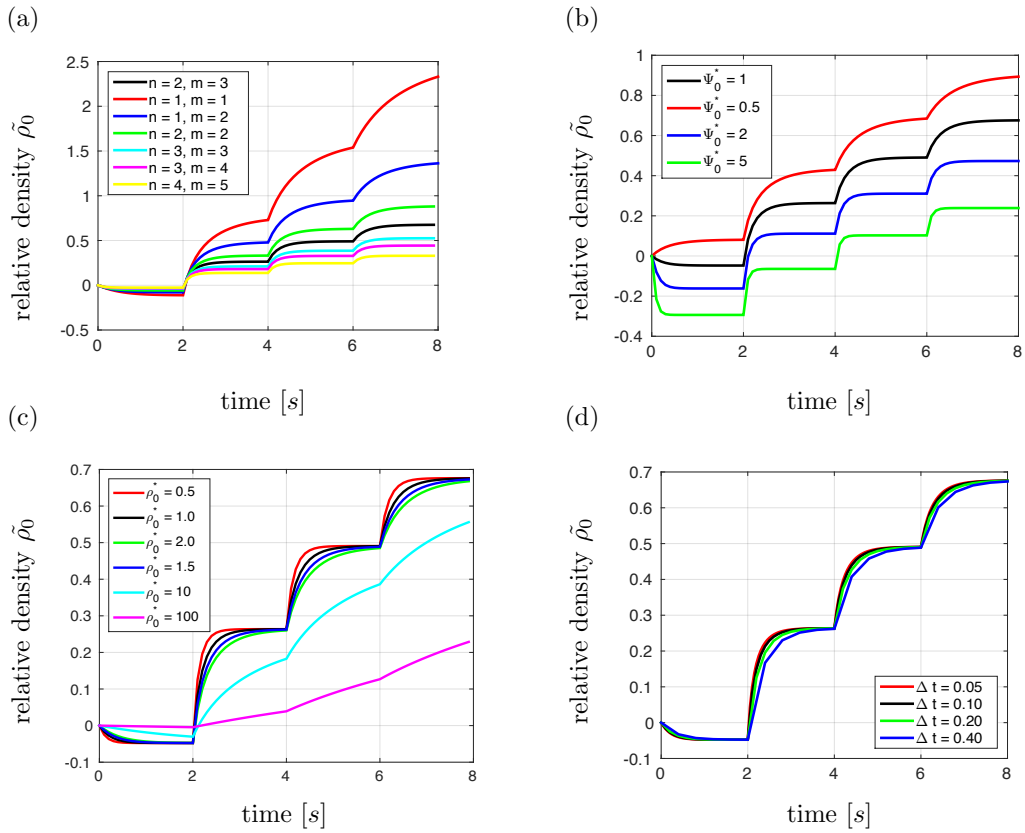

Fig. 6.10: The parameter sensitivity study for the Kuhl and Steinmann (2003) problem. The effect of the material parameters n and m are shown in (a), the influence of the attractor stimulus Ψ_0^* is shown in (b) and finally the initial density ρ_0^* and time step size Δt are investigated in (c) and (d), respectively

is reached nearly immediately. As the attractor stimulus is increased even further beyond a value of

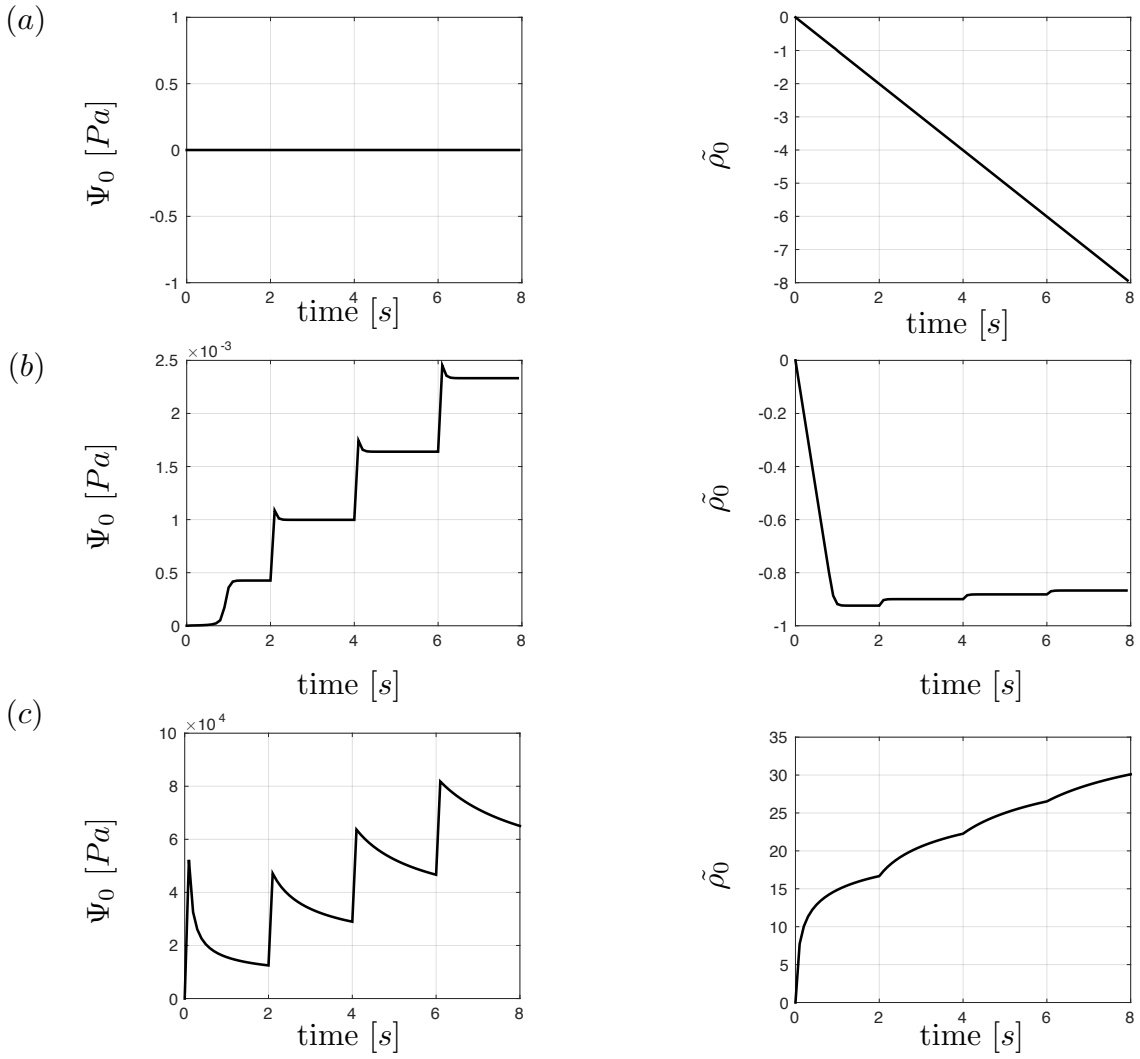

Fig. 6.11: The time evolution of the density weighted free energy Ψ_0 and of the density for the KS model are shown above when (a) the maximum force = 0 N, (b) maximum force = 0.001 and (c) final force = 1000 N is applied.

$\Psi_0^* = 2.5$ MPa, the solution becomes unstable. The density is simply driven to $-\infty$ as shown in Figure 6.15 for a value of $\Psi_0^* = 2.51$ MPa.

Finally, the L_2 norm of the density solution was determined for both cases and are detailed in Table 6.4. The number of elements does not change the result indicating that one element would be sufficient to simulate this uniform problem, and demonstrates that the assembly process in the finite element method is correct.

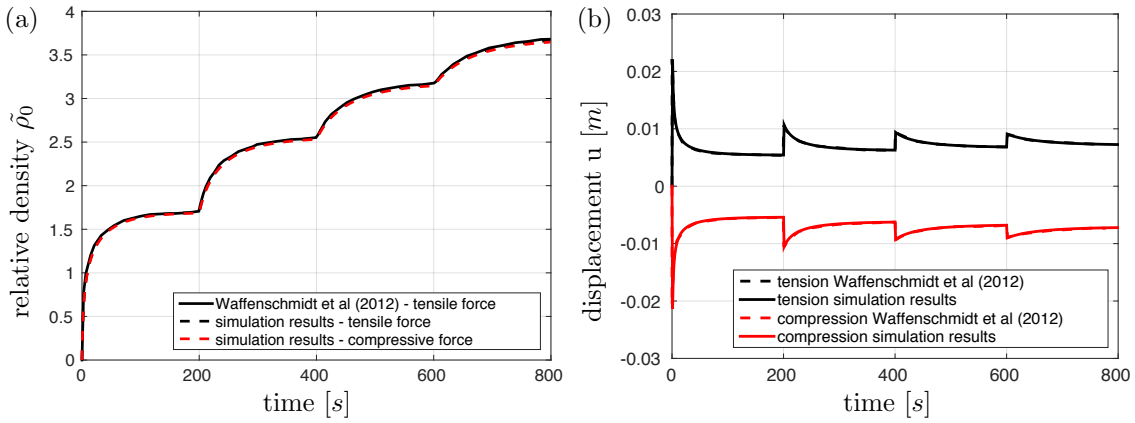

Fig. 6.12: The results of the simulation are compared to the results reported by Waffenschmidt et al. (2012). The density evolution is shown in (a) and the displacement history in (b).

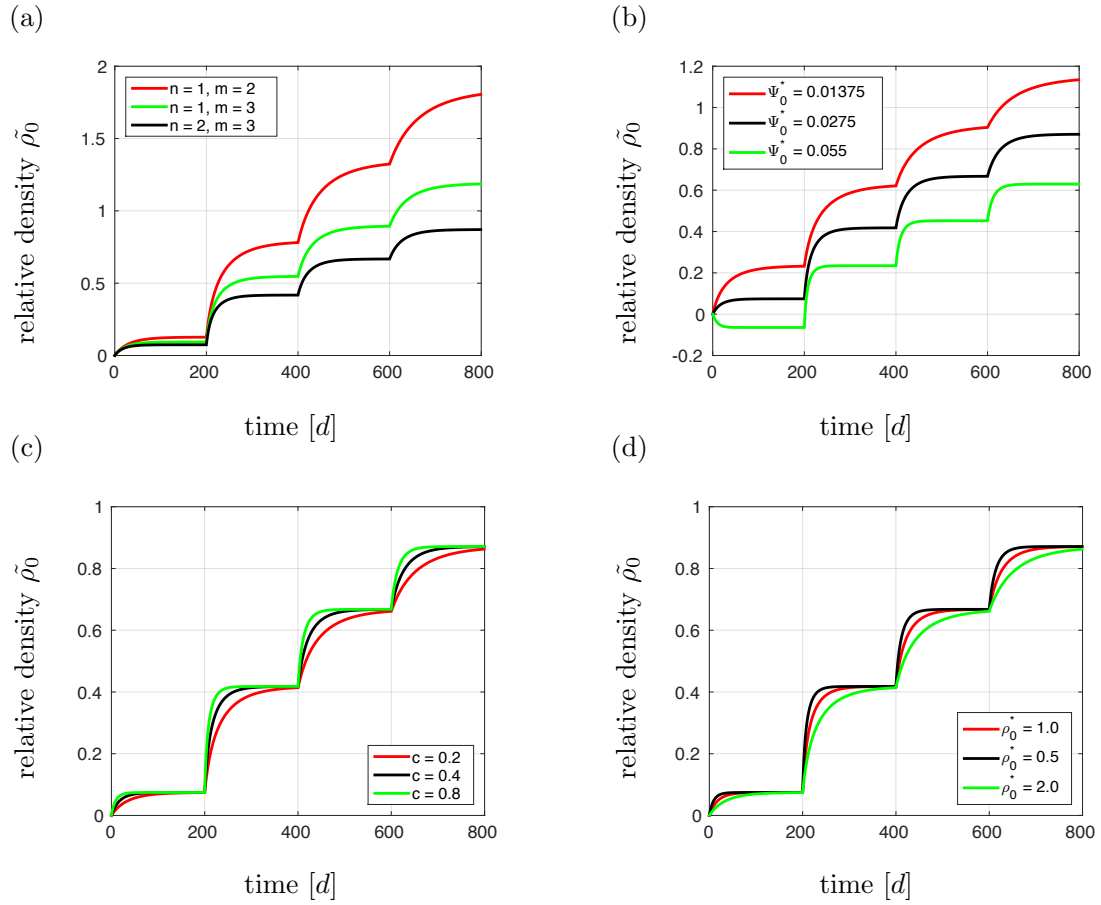

Fig. 6.13: Simulation results of the parameter sensitivity with respect to (a) the material parameters n and m, (b) the attractor stimulus Ψ_0^*, (c) the density evolution velocity c, and (d) the initial density ρ_0^* with a tensile load, which is decreased by a factor of 10 is shown.

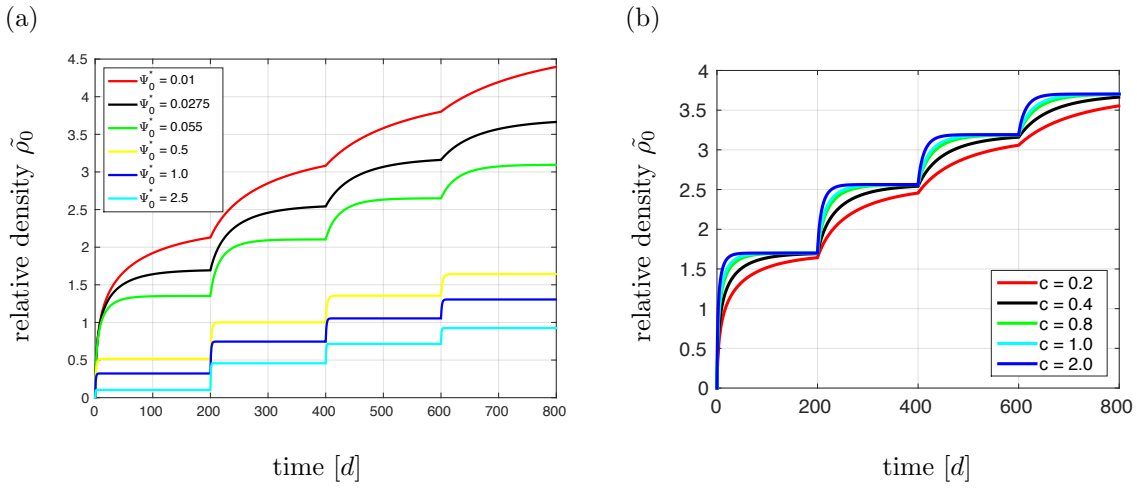

Fig. 6.14: The parameter sensitivity of the relative density $\tilde{\rho}_0$ to (a) the attractor stimulus Ψ_0^* and (b) the density evolution velocity c for the full tensile load, using the Waffenschmidt et al. (2012) parameters.

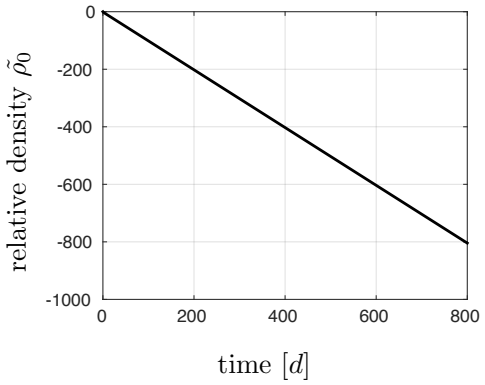

Fig. 6.15: The density evolution for the full Waffenschmidt et al. (2012) tensile problem with an attractor stimulus $\Psi_0^* = 2.51$ MPa.

Table 6.4: The L_2 norm of the density for the problem reported by Kuhl and Steinmann (2003) and Waffenschmidt et al. (2012).

	no. elements	L_2 norm ($\tilde{\rho}_0$)
Kuhl and Steinmann (2003)	1 5 10 100	0.477737
Waffenschmidt et al. (2012)	1 5 10 100	3.66424

6.4 An investigation of the influence of the mass flux

The mass flux term is now investigated. The material properties are summarised in Table 6.5. To investigate the effect of the mass flux, a non-uniform initial density distribution was assigned to a three-dimensional unit size specimen. Two different density distributions were analysed. First, the problem proposed by Kuhl and Steinmann (2003) was implemented and then a different, smoother initial density distribution was considered. The initial density distributions for both cases are shown in Figure 6.16.

Table 6.5: The constitutive parameters reported by Kuhl and Steinmann (2003).

Young's Modulus	E_y	1	[N m^{-2}]
Poisson's ratio	ν	0	[-]
attractor stimulus	Ψ_0^*	1	[N m^{-2}]
	n	2	[-]
	m	3	[-]
mass conduction coefficient	K_0	1	[m^2 s^{-1}]

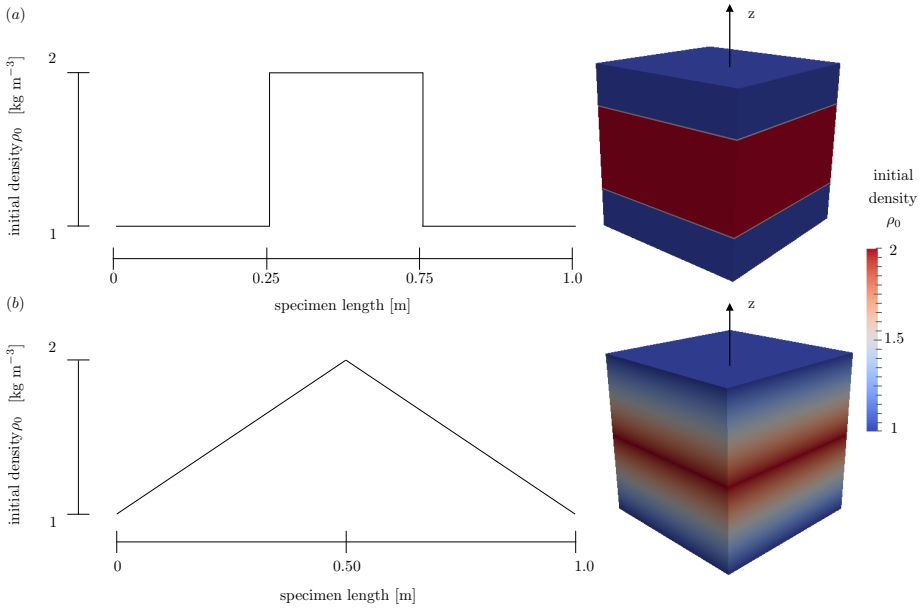

Fig. 6.16: The initial density distributions along the central (z) axis of the specimen, (a) Case 1: as reported by Kuhl and Steinmann (2003) and (b) Case 2: modified initial density distribution with a smoother gradient.

Kuhl and Steinmann (2003) termed the initial density distribution as shown in Figure 6.16 (a) a hat-type distribution. The gradient tends to infinity at the step-change in density. This causes a potential numerical issue, as it is difficult to capture this sudden change in density using a conforming finite element approximation of the density.

Figure 6.17 shows a snapshot of the density distribution along the central axis of the specimen at different times. The time step size was chosen as $\Delta t = 0.1$ s and the domain was divided into 500 elements. The density evolves from the very sharp initial distribution to a uniform distribution due to the mass flux. Figure 6.18 shows the density evolution reported by Kuhl and Steinmann (2003). The trend of the density smoothing to a uniform distribution is identical to the simulation results. It is important to note that the domain analysed here is also divided into a large number of elements. It is not reported what time-step size Kuhl and Steinmann (2003) used. It is evident however, that it must have been a rather large time-step size as equilibrium is reached $t = 500$ s. The effect of the time-step size and number of elements on the solution is discussed shortly.

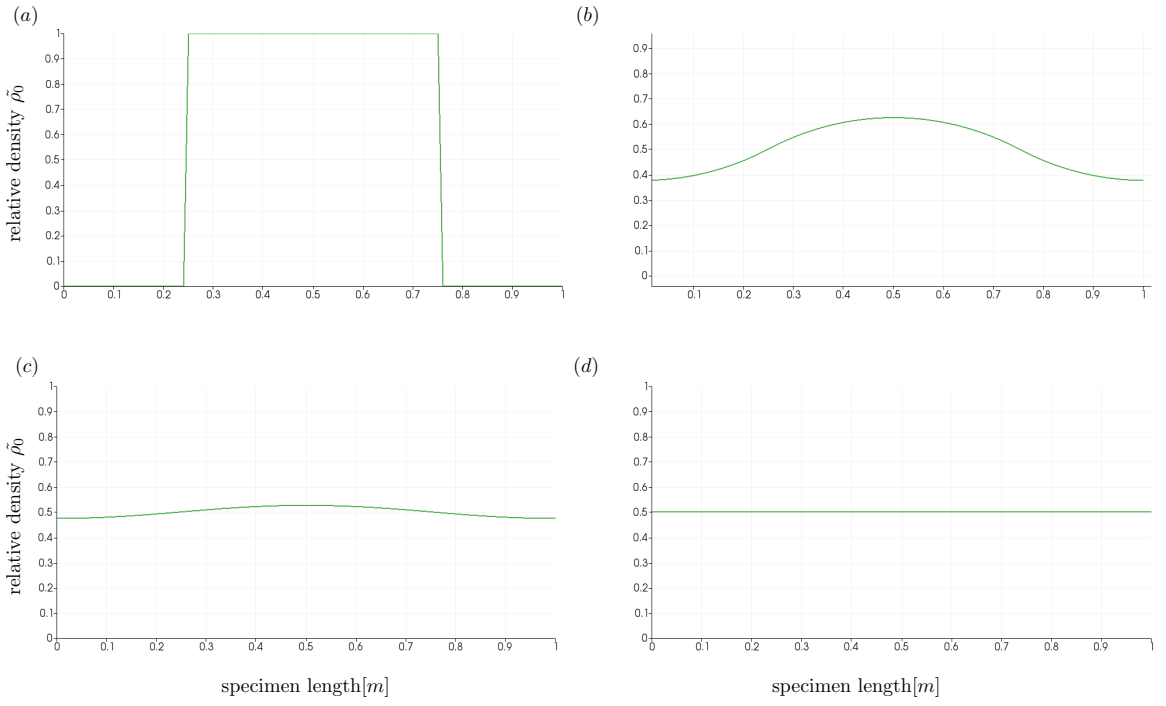

Fig. 6.17: Case 1: the density distribution along the central axis of a specimen with 500 elements and a time-step of $\Delta t = 0.1$ at (a) t = 0 , (b) t = 0.1, (c) t = 0.2 and finally at (d) t = 0.5.

The density evolution of the problem with an initial density distribution as shown in Figure 6.16 (b) is shown in Figure 6.19 at $t = 0$ s,$t = 0.1$ s and at $t = 0.4$ s when equilibrium is reached. The domain is divided into 10 elements and again a time-step size of $\Delta t = 0.1$ s was used. As the jump between different density values is removed, the solution is smoother.

The L_2 norm of the density at the end of the simulations was determined for a number of different elements for both cases to investigate mesh convergence. The results are captured in Table 6.6. Case 2 is insensitive to the number of elements used. Provided two or more elements are used, the solution is stable and converges to $\rho_0 = 0.5$ kg m^{-3} as expected.

The scenario is different for the first case. Here the number of elements is very important. The more elements are used, the more accurate the solution. If the number of elements is decreased past a certain threshold, in this case less than 20 elements, the jump in the density is not captured accurately.

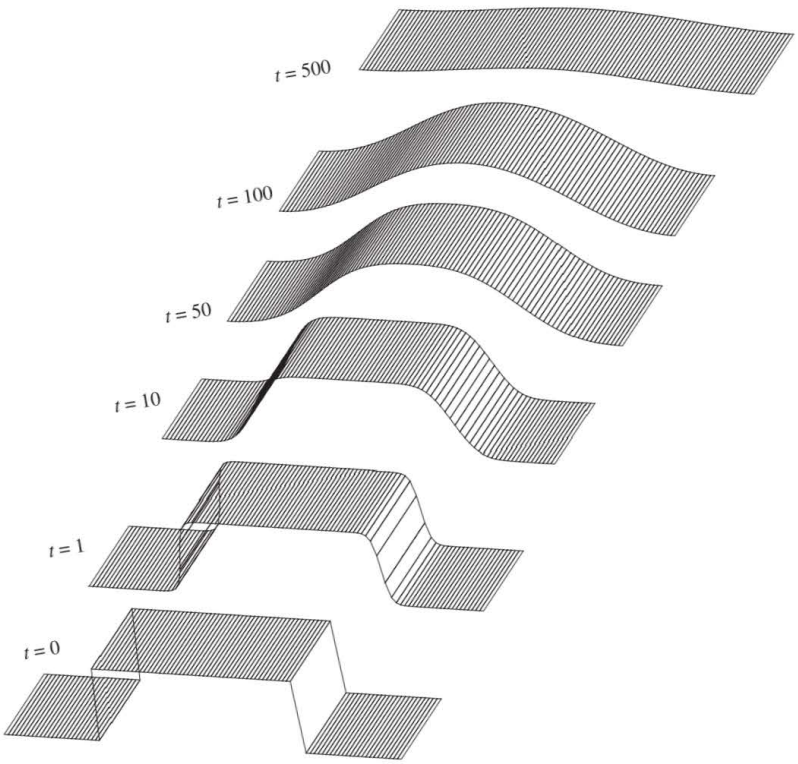

Fig. 6.18: The density evolution computed by Kuhl and Steinmann (2003).

Rather, the initial density distribution is smoothed, as a gradient is introduced across the element encompassing the region of the jump.

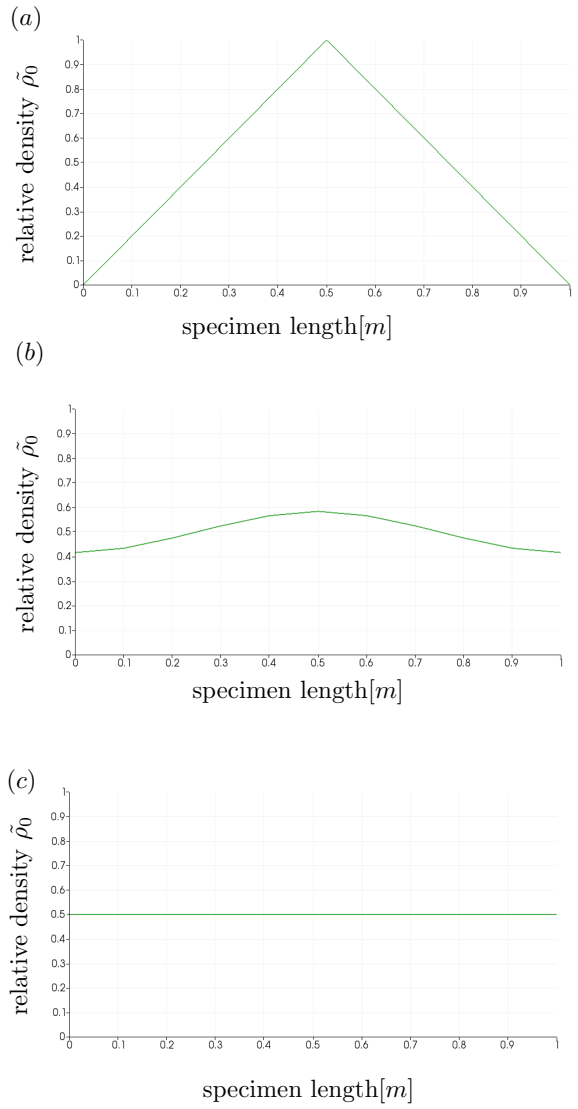

Fig. 6.19: Case 2: the density distribution along the central axis of a specimen with 10 elements and a time-step of $\Delta t = 0.1$ at (a) t = 0 , (b) t = 0.1 and finally at (c) t = 0.4 s.

Table 6.6: Mesh convergence for case 1 and 2.

	no. elements	L_2 norm ($\tilde{\rho_0}$)
Case 1:	2	0.5
	10	0.5
	20	0.5500
	100	0.5100
	500	0.5020
	1000	0.5010
	2000	0.5005
	5000	0.5002
Case 2:	2	0.50
	10	
	100	
	5000	

Finally, the effect of the time-step size on the solution is analysed. Depending on the choice of time-step size, the time until equilibrium is reached is different, as detailed in Table 6.7. This is due to the parabolic nature of the problem. To show that this behaviour is expected, the same initial conditions were applied to the heat equation as shown in Figure 6.20. The density evolution along the central axis is shown in Figure 6.21 at various time-steps. The heat equation behaves in exactly the same way as the balance of mass equation. The same phenomenon that the end time is different for different time-step sizes is observed.

Table 6.7: The dependence of the time until convergence to an equilibrium state is reached (t_{end}) on the time-step size for case 1 and 2 and the heat equation.

	case 1	case 2	heat equation
Δt [s]		t_{end} [s]	
0.01	0.20	0.18	0.2
0.1	0.5	0.4	0.4
1.0	2.0	2.0	3.0

Table 6.8: The material properties used for the heat equation

property		value	unit
material density	$\rho =$	1	$\mathrm{kg\,m^{-3}}$
heat capacity	$c =$	1	$N\mathrm{m\,kg^{-1}}K^{-2}$
heat conduction coefficient	$k_0 =$	1	$W\mathrm{m^{-1}}K^{-1}$
heat source term	$s =$	0	N m^2 K

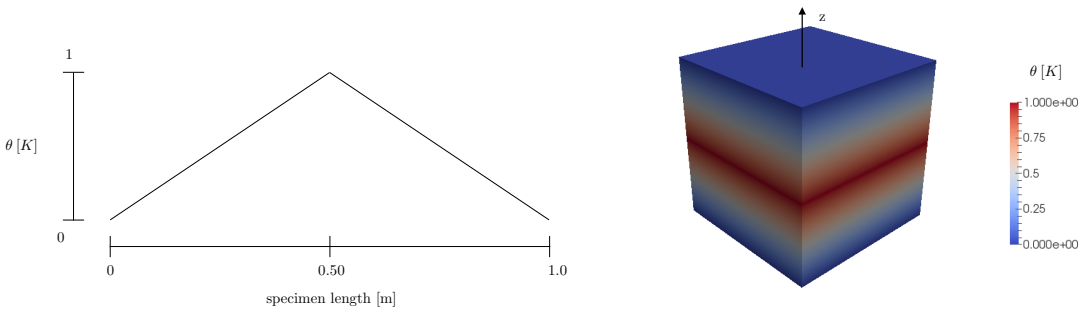

Fig. 6.20: Initial conditions in the heat flux example.

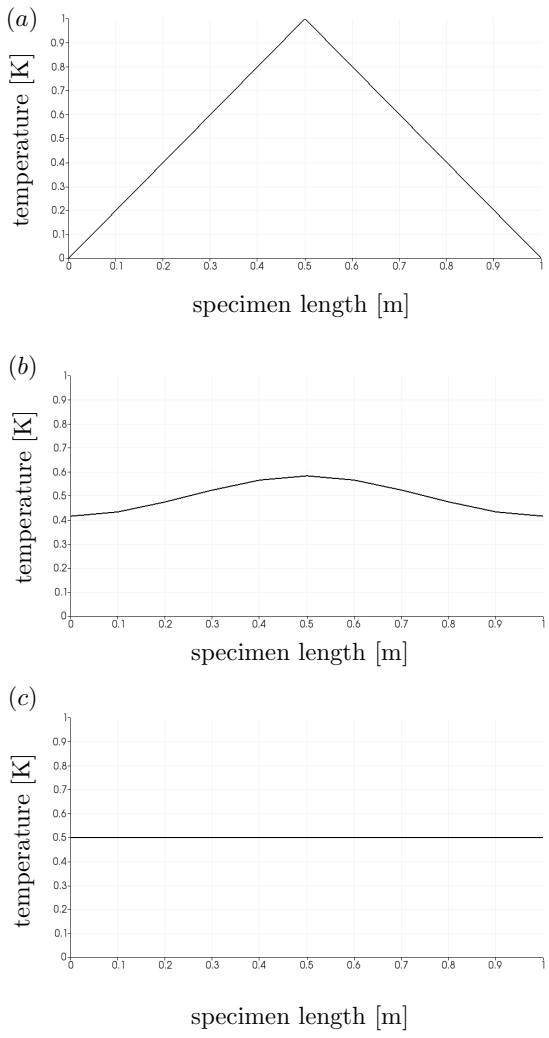

Fig. 6.21: Case 2: the temperature distribution along the central axis of a specimen with 10 elements and a time step of $\Delta t = 0.1$ at (a) t = 0.0 s, (b) t = 0.1 s and (c) t = 0.4 s.

6.5 An investigation of the influence of the mass source and flux

The mass source and flux are now investigated in conjunction. Following Kuhl and Steinmann (2003) a different attractor stimulus was assigned to different sections of the three-dimensional, unit-size specimen shown in Figure 6.22. Assigning different attractor stimuli to the different regions, means that the mass source term will evolve differently in those regions, resulting in an inhomogeneous density distribution. To investigate the influence of the mass flux, the mass conduction coefficient was varied between $K_0 = 0$ and $K_0 = 1$ m^{2}s^{-1}. In total, six simulations were conducted, each with a different conduction coefficient. The remaining material parameters were homogeneous throughout the specimen and are listed in Table 6.9.

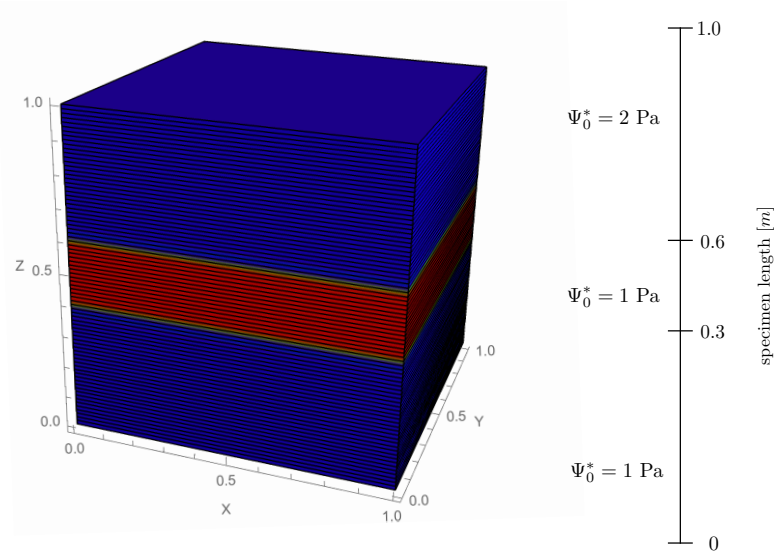

Fig. 6.22: Different domains, each assigned a different attractor stimulus (Kuhl and Steinmann, 2003).

No essential boundary conditions are assigned. An initial density of $\rho_0 = 10$ kg m^{-3} was assigned, to ensure that the density distribution remains positive. The six density distributions at the final time step for different values of the conduction coefficient are shown in Figure 6.23 and the respective results reported by Kuhl and Steinmann (2003) are shown in Figure 6.24. The density profiles match perfectly for each value of the conduction coefficient.

When no mass flux is present in the system, the solution cannot capture the jump in attractor stimulus Ψ_0^* accurately as discussed in the previous section 6.4. When a mass flux is present in the system, the solution is smoothed and the discontinuity is eliminated. For small values of the conduction coefficient, the solution is sufficiently smoothed to eliminate the discontinuity and still capture the features of the solution. As expected, the density is greater in the central region, where the attractor stimulus Ψ_0^* is smaller. However, if the conduction coefficient is very large, the effect of assigning different attractor stimuli to different regions is removed, as the influence of the mass flux dominates the mass source term.

This investigation shows that including both a mass source and flux can be beneficial, especially if discontinuities are present in the system. However, the conduction coefficient must be chosen to be small enough to ensure that the mass flux does not overly smear the solution.

Table 6.9: The homogeneous constitutive and time parameters (Kuhl and Steinmann, 2003).

Young's Modulus	E_y	1	[N m^{-2}]
Poisson's ratio	ν	0	[-]
initial density	ρ_0^*	1	[kg m^{-3}]
	n	2	[-]
	m	3	[-]
density growth velocity	c	1	[s m^{-2}]
mass conduction coefficient	K_0	[0 , 1]	[m^2 s^{-1}]
initial condition	$\tilde{\rho_0}$	10	[kg m^{-3}]
time step	Δt	0.1	[s]
end time	t_{end}	5	[s]

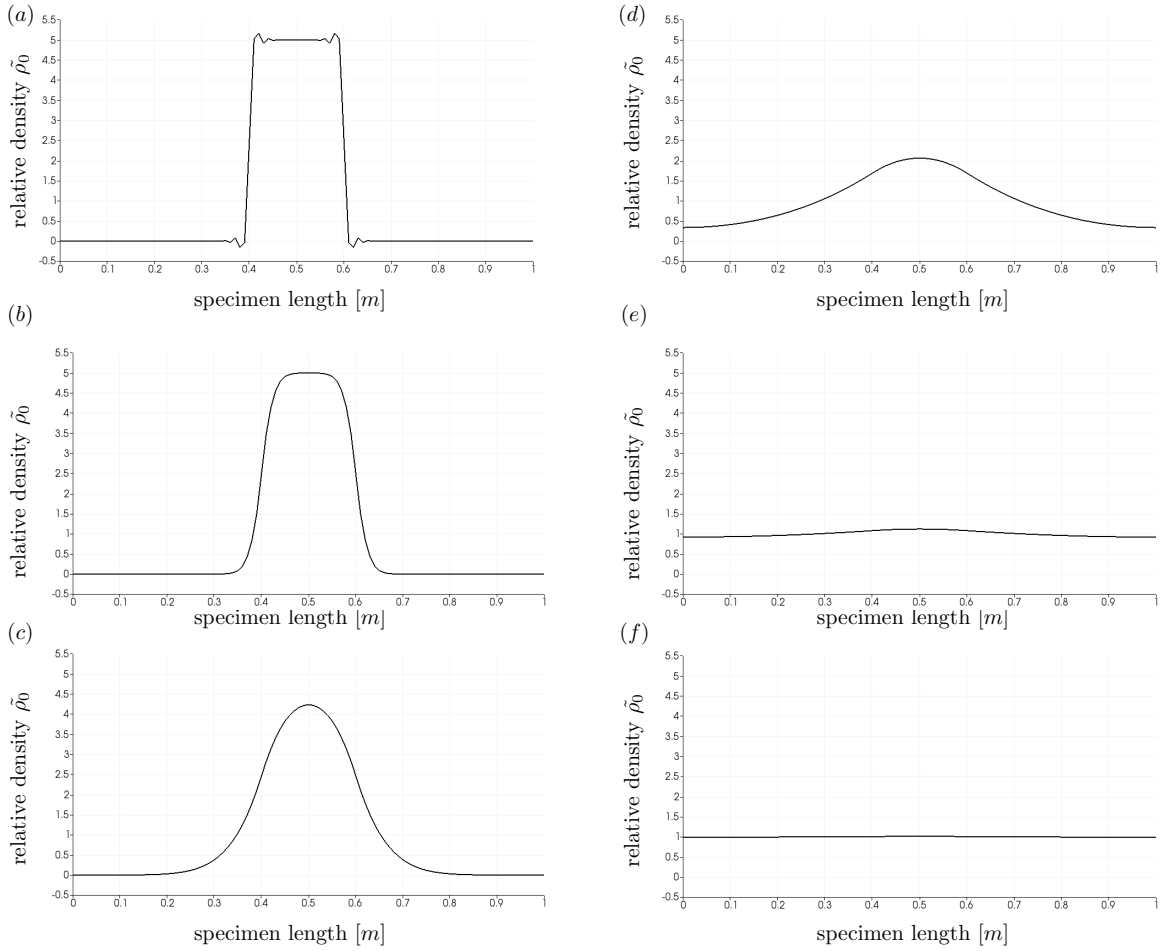

Fig. 6.23: The density distribution once equilibrium has been reached with 80 elements with (a) $K_0 = 0$ [$\mathrm{m}^2\,\mathrm{s}^{-1}$] ,(b) $K_0 = 0.0001$ [$\mathrm{m}^2\,\mathrm{s}^{-1}$] ,(c) $K_0 = 0.0010$ [$\mathrm{m}^2\,\mathrm{s}^{-1}$] ,(d) $K_0 = 0.0100$ [$\mathrm{m}^2\,\mathrm{s}^{-1}$] ,(e) $K_0 = 0.1000$ [$\mathrm{m}^2\,\mathrm{s}^{-1}$] and (f) $K_0 = 1.0000$ [$\mathrm{m}^2\,\mathrm{s}^{-1}$].

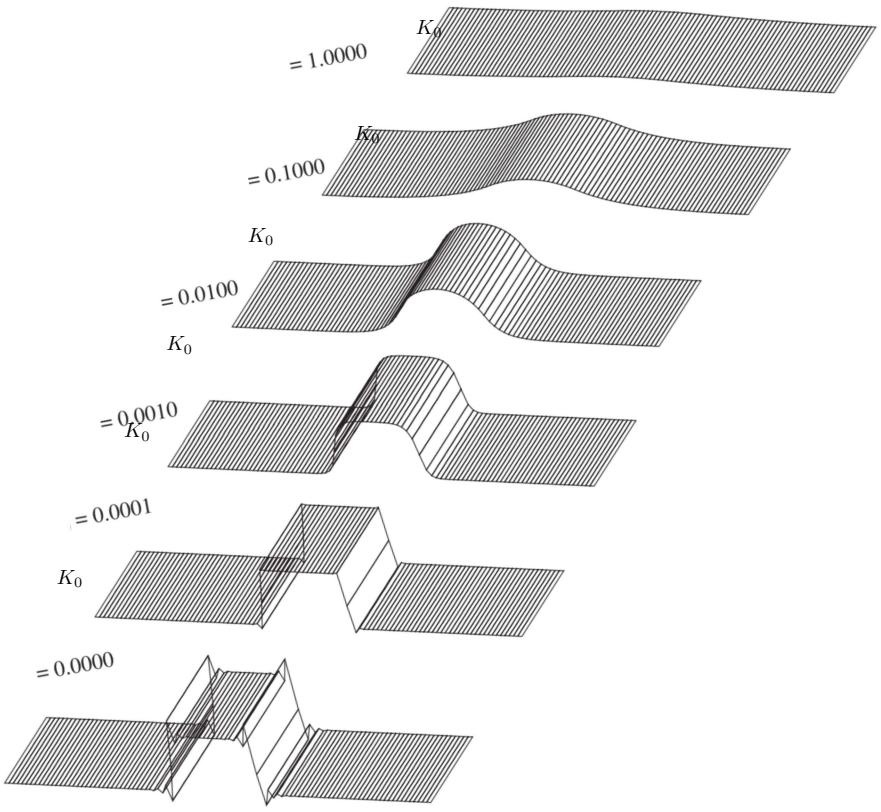

Fig. 6.24: The density evolution predicted by Kuhl and Steinmann (2003).

6.6 Topology optimisation - 2d and 3d analyses

Kuhl and Steinmann (2003) reported on a topology optimisation problem. Different loading conditions are applied to a three-dimensional specimen, which remodels in response to the applied loading. The material properties and simulation parameters are reported in Table 6.10.

Table 6.10: The constitutive and time parameters .

Young's Modulus	E_y	1000	[N m^{-2}]
Poisson's ratio	ν	0.3	[-]
attractor stimulus	Ψ_0^*	0.5	[N m^{-2}]
initial density	ρ_0^*	0.1	[kg m^{-3}]
	n	2	[-]
	m	3	[-]
density growth velocity	c	1	[s m^{-2}]
mass conduction coefficient	K_0	0	[m^2 s^{-1}]
time-step	Δt	0.01	[s]
end time	t_{end}	0.2	[s]

Three different loading scenarios are applied to the specimen. In each case the full load is applied instantaneously and held constant throughout the simulation.

The first load scenario is shown in Figure 6.25 applied to the 1 m × 0.5 m × 0.5 m block, which is fixed along the left and right bottom edge, as indicated. The density evolution is shown at time $t = 0.1$ s and once equilibrium has been reached at $t = 0.5$ s. The final density distribution is a strut-like structure, which is the optimal shape for the loading condition. Figure 6.27 shows the density evolution at two points in the domain. At t = 0.2 s the densities begin to converge, as reported by Kuhl and Steinmann (2003).

A comparison between the simulation result and the result reported by Kuhl and Steinmann (2003) is shown in Figure 6.26 (a). Two further load conditions are analysed and the final density distributions and boundary conditions are shown in Figure 6.26. In each case the results qualitatively match those of Kuhl and Steinmann (2003). The force magnitude and mesh size used by Kuhl and Steinmann (2003) was not provided, precluding a quantitative comparison. The simulations were conducted with a force magnitude of 0.1 N.

Kuhl and Steinmann (2003) further report on an investigation of the mass flux term on the problem. Mass conduction coefficients of $K_0 = 0.05 m^2\,s^{-1}$, $K_0 = 0.1 m^2\,s^{-1}$, $K_0 = 2.0 m^2\,s^{-1}$, $K_0 = 1$ and $K_0 = 5.0 m^2\,s^{-1}$ were investigated, as shown in Figure 6.28. The solution is smoothed, as the mass conduction coefficient is increased. Once $K_0 = 5.0 m^2\,s^{-1}$ is applied, the effect of the mass flux dominates and the resulting density distribution is uniform across the domain. These results prove again that a sufficiently small mass conduction coefficient results in a smooth solution.

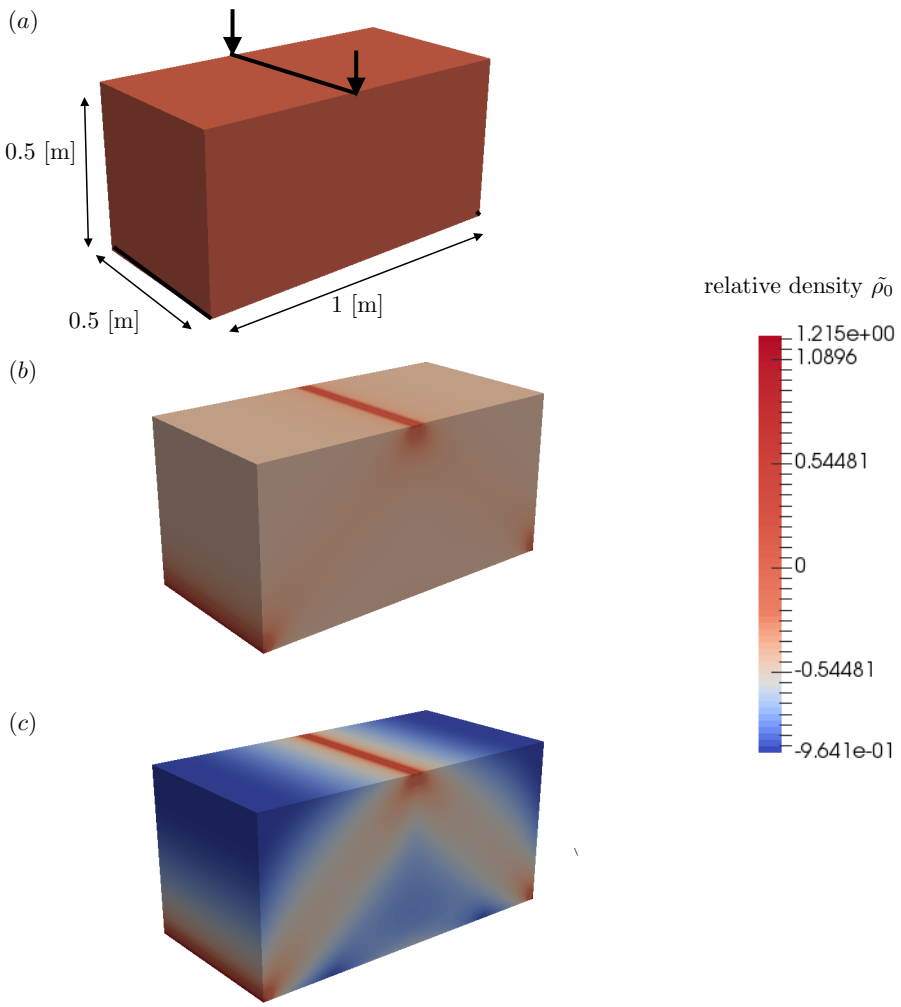

Fig. 6.25: The first loading scenario. The boundary conditions and dimensions are shown in (a) at t = 0 s. The density distribution at t = 0.1 s is shown in (b) and finally in the equilibrium state at t = 0.5 s in (c).

Finally, a mesh convergence study is performed. A two-dimensional test specimen was used and the first loading scenario considered. The L_2 norm for the density was determined as a measure of global convergence. The results are detailed in Table 6.11. The L_2 norm is identical up to three significant figures. The reason for the slight discrepancy is due to the boundary conditions. The force and essential boundary conditions are applied point-wise, resulting in singularities. The problem would be improved by altering the boundary conditions.

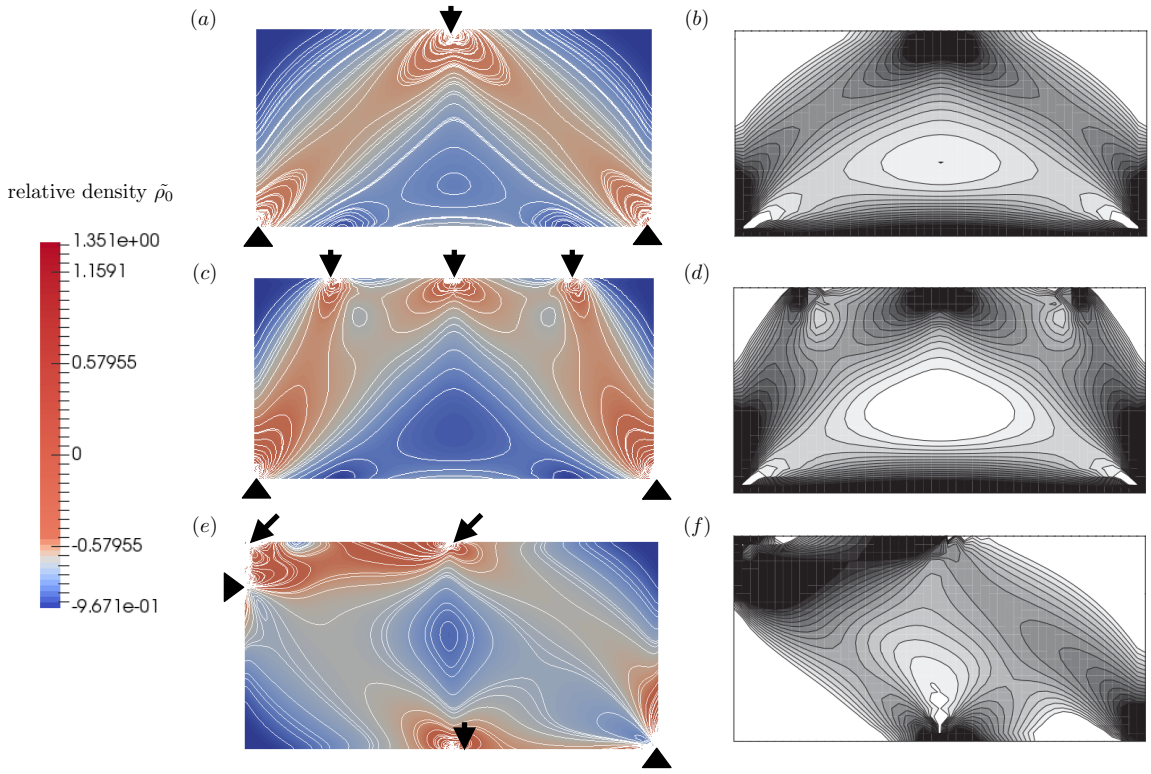

Fig. 6.26: The density distribution for three different load cases. The simulation results for load case 1 and the loading condition are shown in (a) and are compared to (b) the result by Kuhl and Steinmann (2003). Similarly the simulation result and load case 2 are shown in (c) and the Kuhl and Steinmann solution in (d). Finally loading scenario 3 and the simulation result is shown in (e) and the result of Kuhl and Steinmann in (f).

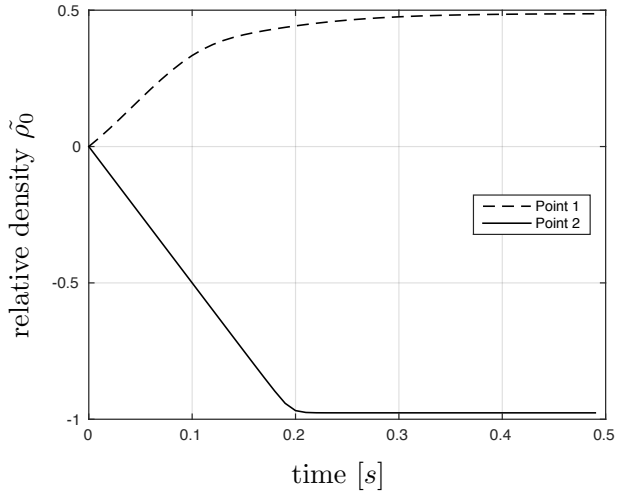

Fig. 6.27: The density evolution at a point in the top right corner of the specimen. Convergence is reached when t = 0.2 s.

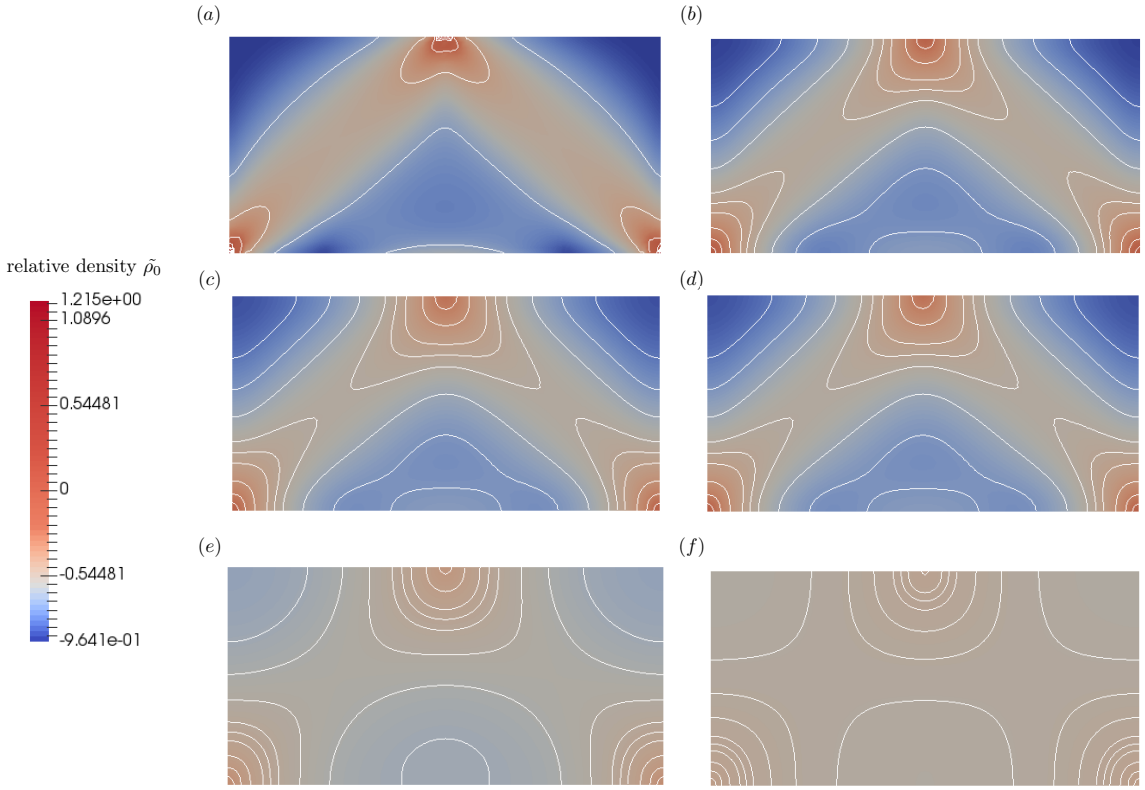

Fig. 6.28: The density distribution for load case 1, for (a) $K_0 = 0\mathrm{m}^2\,\mathrm{s}^{-1}$, (b) $K_0 = 0.05\mathrm{m}^2\,\mathrm{s}^{-1}$, (c) $K_0 = 0.1\mathrm{m}^2\,\mathrm{s}^{-1}$, (d) $K_0 = 0.20\mathrm{m}^2\,\mathrm{s}^{-1}$, (e) $K_0 = 1.0\mathrm{m}^2\,\mathrm{s}^{-1}$ and finally (f) $K_0 = 5.0\mathrm{m}^2\,\mathrm{s}^{-1}$.

Table 6.11: Mesh convergence for the two-dimensional problem using the L_2 norm of the density for the first loading scenario.

mesh division	L_2 norm ($\tilde{\rho}_0$)
25×50	0.576055
40×80	0.576184
50×100	0.576191
100×200	0.576144

6.7 Benchmark problem: proximal femur

The classical benchmark problem of the proximal femur is now analysed. A two-dimensional mesh of the femur from StanfordUniversity (2016) was used. The approximate loading conditions for maximum adduction and the mid-stance of the gait cycle are reported in Table 6.13. The material properties and time parameters reported by Kuhl and Steinmann (2003) for the same problem were used and are summarised in Table 6.12. The femur is fixed in the direction of the vertical axis along the bottom edge and fully fixed on the bottom-right corner.

The result of the simulation is shown in Figure 6.29 (c). The result reported by Kuhl and Steinmann (2003) is shown in Figure 6.29 (b). The results are in good qualitative agreement. Discrepancies may be due to different meshes and different finite element formulations. Kuhl and Steinmann may have used an element level based finite element formulation for the density, as no flux is present.

The influence of the mass flux is analysed as shown in Figure 6.29 (d). A mass conduction coefficient of $K_0 = 0.01$ s m^{-2} is used. This smoothed the solution and increased the convergence rate. Also, the bounds of the density were decreased. If the mass conduction coefficient is chosen too large, the result is non-physical. Therefore, applying a small conduction coefficient is a good choice.

The results can be compared to an x-ray image of femur, reported by Jacobs et al. (1997). The density distribution correlates well to the actual density distribution of the human femur. However, no quantitative conclusion can be drawn. In order to do this, physiological boundary conditions would have to be applied to a realistic three-dimensional geometry.

Kaczmarczyk and Pearce (2011) extended this model to a three-dimensional geometry and came to the conclusion that the theory captures density remodelling well. However, to draw meaningful conclusions from the model, it is essential to apply realistic material parameters and boundary conditions.

Table 6.12: The constitutive and time parameters reported by Kuhl and Steinmann (2003) for the proximal femur benchmark.

Young's Modulus	E_y	500	[MPa = N mm^{-2}]
Poisson's ratio	ν	0.2	[-]
attractor stimulus	Ψ_0^*	0.01	[MPa = N mm^{-2}]
initial density	ρ_0^*	1.2	[kg mm^{-3} = g cm^{-3}]
	n	2	[-]
	m	3	[-]
density growth velocity	c	1	[s m^{-2}]
mass conduction coefficient	K_0	0	[m^2 s^{-1}]
time-step	Δt	0.2	[s]
end time	t_{end}	250	[s]

Table 6.13: Loading on the femur as reported by Jacobs et al. (1997). The angle of loading is measured from the horizontal.

	LHS	RHS
load case 1:	2.317 kN @ 24^o	0.703 kN @ 28^o
load case 2:	0.351 kN @ -8^o	1.158 kN @ -15^o
load case 3:	0.468 kN @ 35^o	1.548 kN @ 56^o

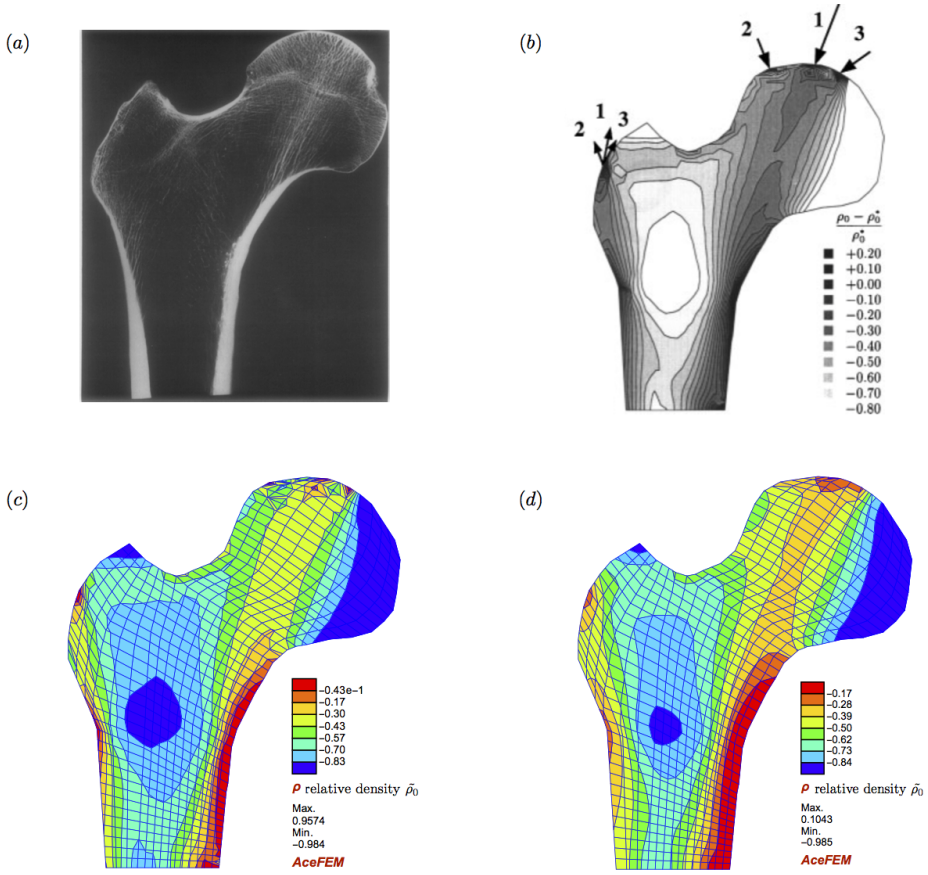

Fig. 6.29: Figure (a) is a X-ray image of the human femur, taken from Jacobs et al. (1995). The light colour indicates regions of high density. Further figures show the results from (b) Kuhl and Steinmann (2003), (c) simulation results with no mass flux and (d) simulation results with a mass flux of $K_0 = 0.01\ \mathrm{m}^2\,\mathrm{s}^{-1}$.

7

Computational investigation of the reverse shoulder procedure

The validated finite element model for bone remodelling is now applied to the reverse shoulder. The model is tested with the ASTM F2028 standard polyurethane foam block simulation. A stress analysis is conducted and remodelling is investigated. Remodelling in the intact scapula is then analysed. Finally the model is applied to a reverse shoulder prosthesis.

7.1 Polyurethane foam block simulation

Polyurethane is a proxy material for bone. Polyurethane obviously does not undergo remodelling but we use the following example to explore features of our model. The polyurethane (PU) foam block example was constructed with guidance from the ASTM F2028 standard as detailed in Chapter 3. A CAD model of a reverse shoulder prosthesis was provided by collaborators in the Division of Biomedical Engineering at UCT. The prosthesis was virtually implanted into the foam block. The assembly was then meshed in the BETA CAE preprocessing package ANSA (BETACAESystems, 2016) using the hexablocking technique and then imported to the AceFEM library. Owing to the symmetry of the problem, only half of the geometry was modelled. The geometry and mesh are shown in Figure 7.1.

Two loading conditions were applied following the ASTM guidelines as shown in Figure 7.2. In the first loading scenario a compressive force of 750 N was considered. A 750 N force acting at 45^o on the glenosphere was applied in the second loading scenario.

The material properties were chosen from literature and are summarised in Table 7.1. The polyurethane foam block is first modelled as a hyperelastic material. Remodelling is then activated to analyse how the density would change in the block, if it were living bone, in response to the loading condition. The Young's modulus and Poisson's ratio were chosen from the recommendations stated in the ASTM standard (ASTM, 2014; Virani et al., 2008). The parameters c and ρ_0^* were taken from Waffenschmidt et al. (2012), as was the attractor stimulus Ψ_0^*, where the smallest value reported in the study was used. The choice of the attractor stimulus Ψ_0^* was made as the material properties are also lower than those used by Waffenschmidt et al. (2012). The screws, metaglene and glenosphere are modelled as linear elastic materials. The material parameters for the implant were chosen as the most frequently reported values in literature (see Table 3.1 in Chapter 3). The different components were modelled as perfectly bonded, which means that no relative sliding or opening between the components was permitted (i.e. the nodes at the interfaces are shared).

The model consists of 254 389 degrees of freedom for the remodelling problem. A mesh convergence check was conducted by determining the L_2 and H_1 displacement norms, as detailed in Table 7.2 to ensure that the mesh is fine enough.

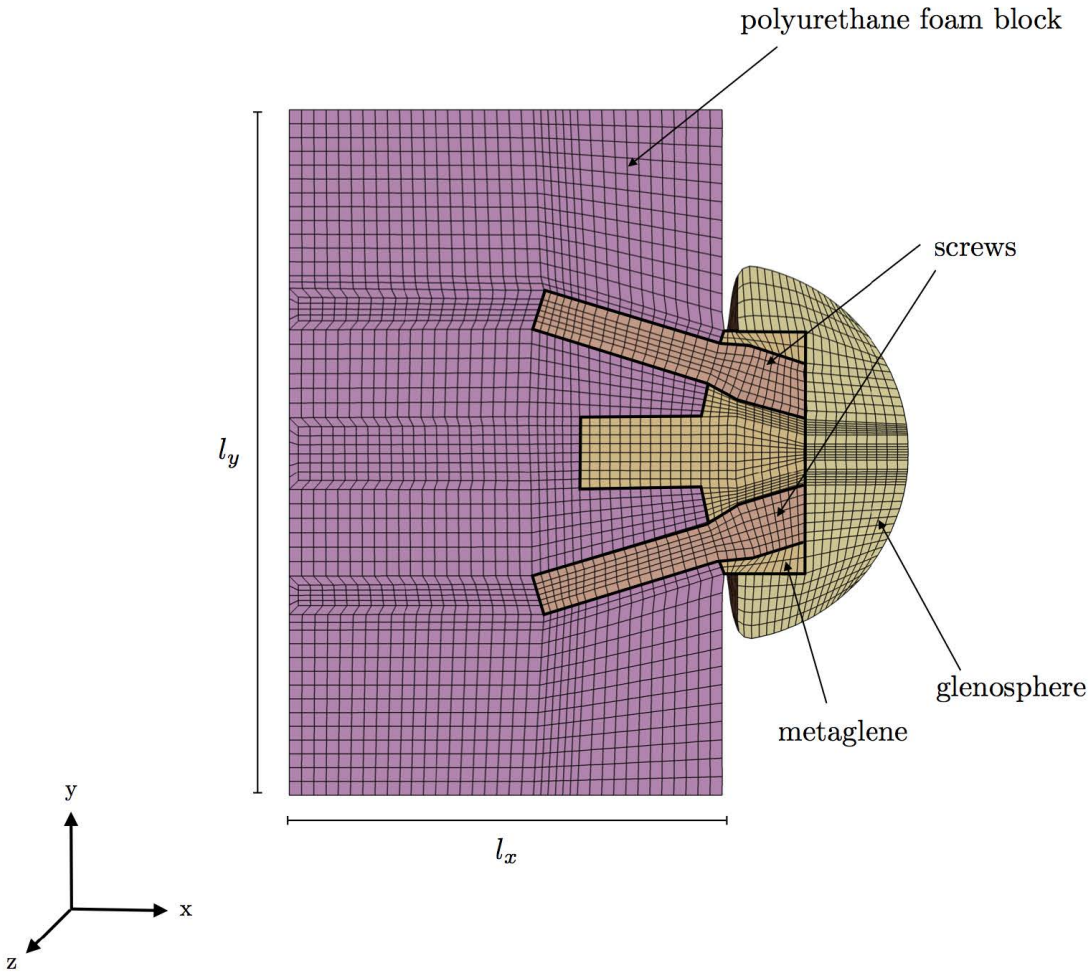

Fig. 7.1: The mesh of the polyurethane foam block model, showing all components.

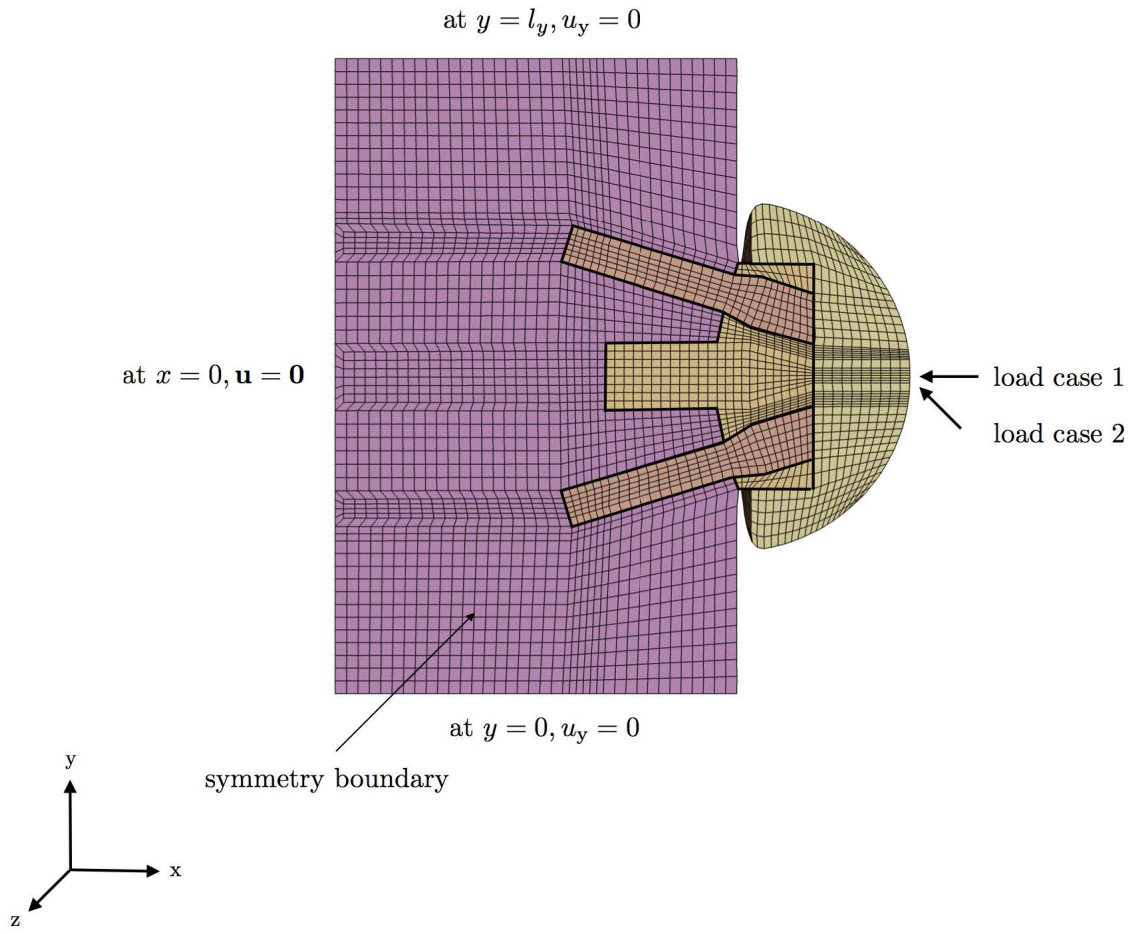

Fig. 7.2: Two loading conditions detailed by the ASTM F2028 standard were considered. In loading condition 1 a 85% of a standard body force (= 750 N) compressive force is applied and in load case 2 the same force is applied at 45^o to the vertical.

Table 7.1: The material properties used in the polyurethane foam block example.

polyurethane foam block:		
Young's modulus	$E_y = 193$	Nmm^{-2}
Poisson's ratio	$\nu = 0.25$	
initial density	$\rho_0^* = 1$	$\mathrm{g\,cm}^{-3}$
attractor stimulus	$\Psi_0^* = 0.01375$	Nmm^{-2}
parameter 1	$n = 2$	
parameter 2	$m = 3$	
speed of adaptation	$c = 0.0$ (hyperelastic)	dcm^{-2}
	$c = 0.4$ (remodelling)	
conduction coefficient	$K_0 = 0.0$ (hyperelastic)	$\mathrm{mm}^2\mathrm{d}^{-1}$
	$K_0 = 0$ - 0.01 (remodelling)	$\mathrm{mm}^2\mathrm{d}^{-1}$
screws and metaglene:		
Young's modulus	$E_y = 117\ 000$	Nmm^{-2}
Poisson's ratio	$\nu = 0.3$	
glenosphere:		
Young's modulus	$E_y = 230\ 000$	Nmm^{-2}
Poisson's ratio	$\nu = 0.3$	

Table 7.2: Mesh convergence check for the polyurethane foam block example with the displacement norms.

degrees of freedom	L_2 norm	H_1 norm
201 781	34.7653	34.8075
254 389	34.7627	34.8050
343 056	34.7609	34.8033

7.1.1 Hyper-elastic model

The response of the polyurethane foam block modelled as a Neo-Hookean hyper-elastic material for both load cases is now analysed. The results are shown in Figures 7.3 and 7.4. Following Sharma and Robertson (2013) a time-step size of $\Delta t = 10$ d was used. The simulation was run until $t = 500$ d, where the solution is fully converged.

The results of load case 1 show that the stress is located in the screws as shown in Figure 7.3 (c) and (d). This is expected, as the screws are stiff, load bearing components. The line of action thus travels through the screws. The less stiff foam block is then deformed as a result of the loading. This can be seen from the displacement of the implant into the foam block and the resulting strain, which is concentrated around the screws in the foam block. The deformed domain is shown in Figure 7.3 (a) and (b). Due to the interpolation in the post processing procedure, a transition region at the interfaces is evident, especially in the strain field. A solution to this issue may be to introduce two nodes at the interface, or even refining the mesh in the affected areas to minimise the unwanted smoothing.

Comparing the results to the second load case shows that the stress magnitude is nearly twice as large in the second example, as shown in Figure 7.4 (c) and (d). This is expected, as only one screw carries the load. Because the load is concentrated on one side, the Green-Lagrange strain magnitude and displacement magnitude, shown in Figure 7.4 (a) and (b), are also greater on the loaded side compared to the first loading scenario.

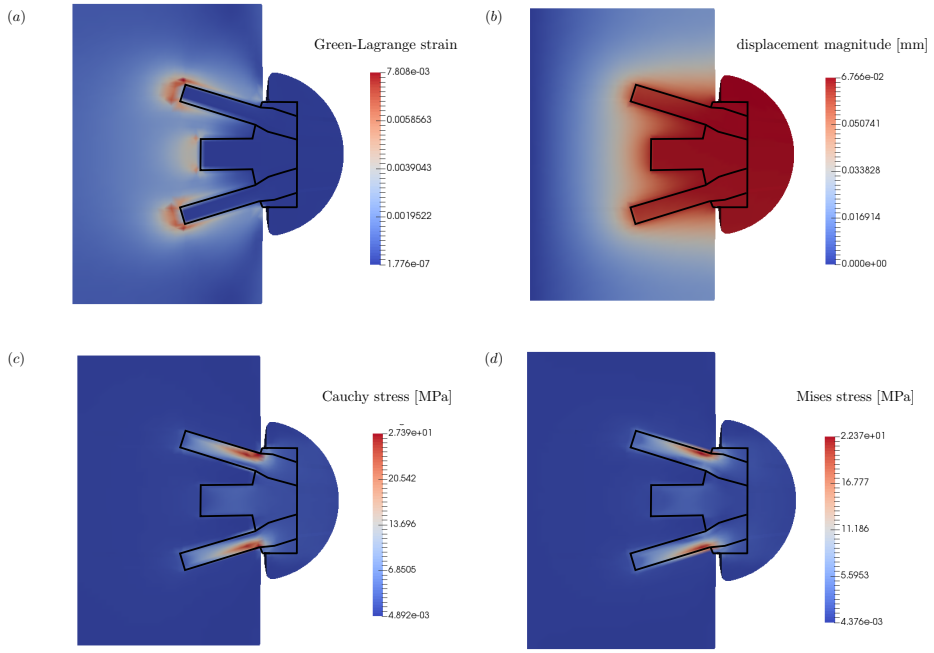

Fig. 7.3: Resulting strain, displacement and stress magnitudes after loading condition 1 was applied for 500 d with $\Delta t = 10$ d.

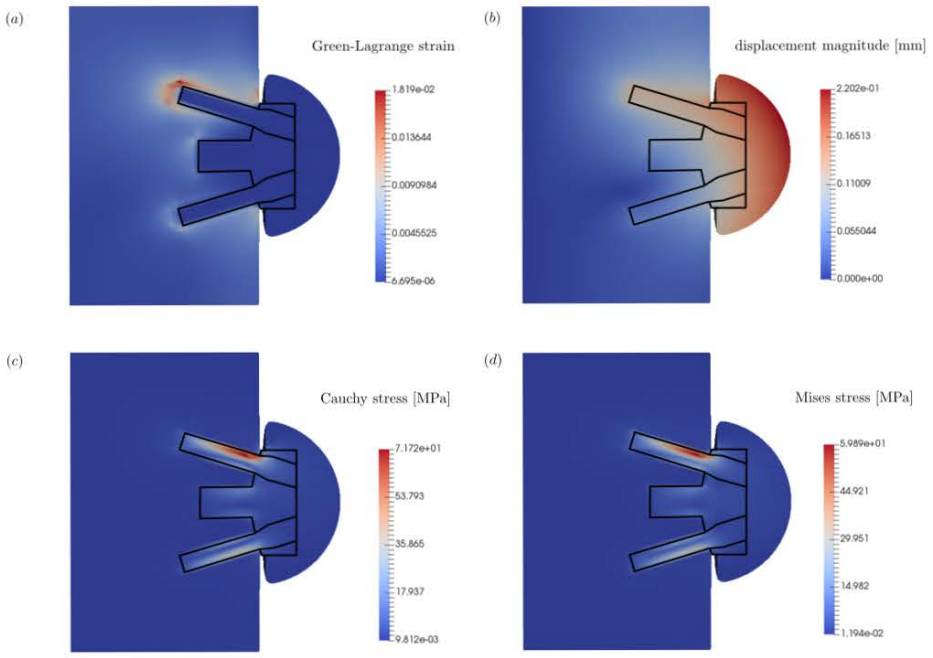

Fig. 7.4: Resulting strain, displacement and stress magnitudes after loading condition 2 was applied for 500 d with $\Delta t = 10$ d.

7.1.2 Remodelling

The hypothetical remodelling response of the foam block is now investigated. Note, the density degree of freedoms at the bone-implant interface are allowed to undergo remodelling in the current finite element implementation.

Load cases 1 and 2 are applied to the foam block with a mass conduction coefficient $K_0 = 0.01$ $\mathrm{mm^2\,d^{-1}}$. Again following Sharma and Robertson (2013), a time step size $\Delta t = 10$ d was used. The influence of the conduction coefficient is investigated by comparing the results of load case 1 for a conduction coefficient of $K_0 = 0.005$ $\mathrm{mm^2\,d^{-1}}$ to a zero condition. Finally, the influence of the time-step size is studied. Load case 1 is again considered with a conduction coefficient of $K_0 = 0$ $\mathrm{mm^2\,d^{-1}}$ and $K_0 = 0.01$ $\mathrm{mm^2\,d^{-1}}$, in both cases with a time-step size $\Delta t = 0.5$ d.

The resulting relative densities, displacement and stress magnitudes after loading conditions 1 and 2 were applied for 500 d with $\Delta t = 10$ d and a mass conduction coefficient of $K_0 = 0.01$ $\mathrm{mm^2\,d^{-1}}$ are shown in Figures 7.5 and 7.6. The stress is concentrated in the screws, as expected, as these are stiff, load-bearing components. As a result, the foam block density increases in the vicinity of the screws. As the greater part of the foam block does not experience any loading, the density decreases in these areas. This demonstrates that bone would not evolve to the non-optimal shape of a rectangular block. The implant is displaced by a fairly large amount, as the density in the foam block decreased in many regions where the loading was low. Because the density is coupled to the material properties through the definition of the free energy, the bone is less stiff in the regions of low density and therefore offers little resistance to deformation. Conversely, in the regions of increased density, the stiffness increases and consequently the resistance to deformation increases and therefore larger stresses are observed. The stress magnitudes are of an order of magnitude larger in the remodelling block, compared to the hyper-elastic counterpart. Similarly, the minimum stress is two orders of magnitude smaller in the remodelling block compared to the hyper-elastic model. This is observed for both loading cases. The coupling between the stress and density evolution is also observed when comparing the two loading conditions in the remodelling block. As the stress is about twice as big in loading condition 2 than in 1, the maximum density is accordingly about double.

These results show that it is important to incorporate remodelling when investigating the stresses and strains in bone.

The remodelling behaviour is further investigated by adjusting the mass flux coefficient K_0 for load case 1. Figures 7.7 and 7.8 show the density distribution, displacement, and stress magnitudes at $t = 500$d for $K_0 = 0.005\mathrm{mm^2\,d^{-1}}$ and $K_0 = 0\mathrm{mm^2\,d^{-1}}$, respectively. As the mass flux coefficient decreases, the density range increases, as shown in Figure 7.9, because the mass flux no longer smooths the solution. This in turn means that the time until convergence is reached, is increased. With a conduction coefficient $K_0 = 0.01\mathrm{mm^2\,d^{-1}}$ the solution converges at $t = 270$ d according to a convergence criteria, similar to that reported by Sharma and Robertson, where the average density $\Delta\rho_{0\mathrm{avg}} = 0.5\,(\rho_{\max} + \rho_{\min}) < 0.01\mathrm{g\,cm^{-3}}$. With no mass flux in the system, convergence is reached at $t = 330$d. Even though mass conduction coefficient K_0 has an influence on the density and convergence rate, the stress and strain state does not change significantly.

What is of interest, is whether the choice of time step size is adequate to arrive at an accurate solution and the influence of the time-step size on the convergence rate. To draw conclusions on the choice of time-step size, the problem was run for load case 1 with $K_0 = 0.01\mathrm{mm^2\,d^{-1}}$ and $K_0 = 0\mathrm{mm^2\,d^{-1}}$ with a significantly smaller time step size $\Delta t = 0.5$d. The resulting density distribution, displacement and stress magnitudes for $K_0 = 0.01\mathrm{mm^2\,d^{-1}}$ and $K_0 = 0\mathrm{mm^2\,d^{-1}}$ at $t = 500$d are shown in Figures 7.10 and 7.11.

The densities lie within a tolerance of $0.01\mathrm{g\,cm^{-3}}$ when compared to the corresponding results with the larger time-step size. A time-step size of $\Delta t = 10$d is therefore sufficient to accurately capture the final density distribution, while saving on computational cost, thereby reducing the simulation time by hours.

The rate of convergence is further affected by the choice of time step size. With no mass flux in the system, convergence is reached at $t = 335$d with $\Delta t = 0.5$d, which is close to the 330d reported with a time-step size of $\Delta t = 10$d. However, when the conduction coefficient is increased to $K_0 = 0.01\mathrm{mm^2\,d^{-1}}$

the solution converges at $t = 253.5$d compared to $t = 270$d with the bigger time-step size. This phenomenon is discussed in Section 6.4.

This means that the time until convergence does not necessarily have a physical interpretation.

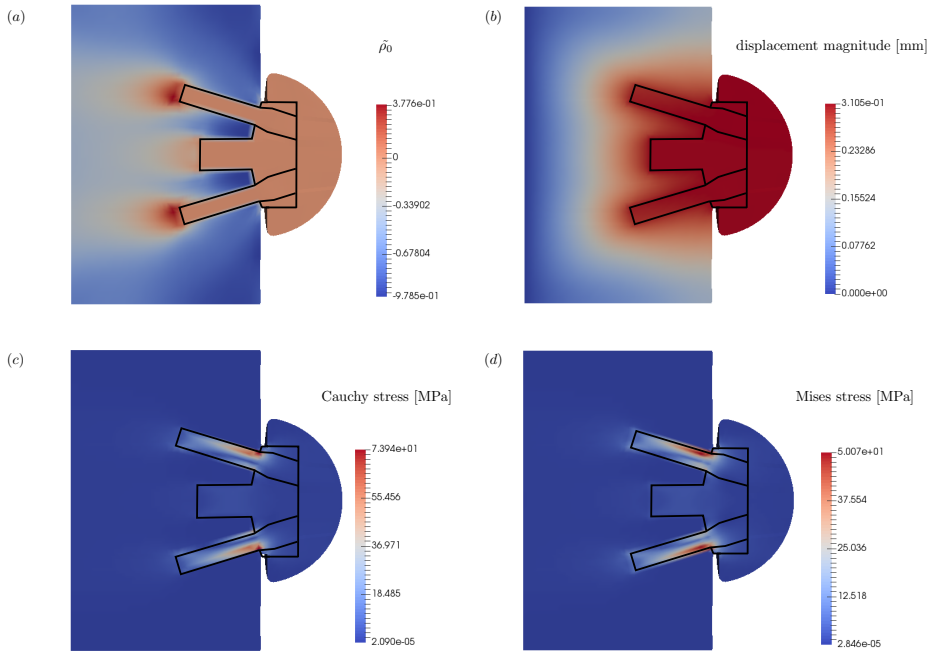

Fig. 7.5: Resulting relative density $\tilde{\rho}_0$ and displacement and stress magnitudes after loading condition 1 was applied for 500 d with $\Delta t = 10$ d with a mass conduction coefficient of $K_0 = 0.01$ mm^{2}d^{-1}.

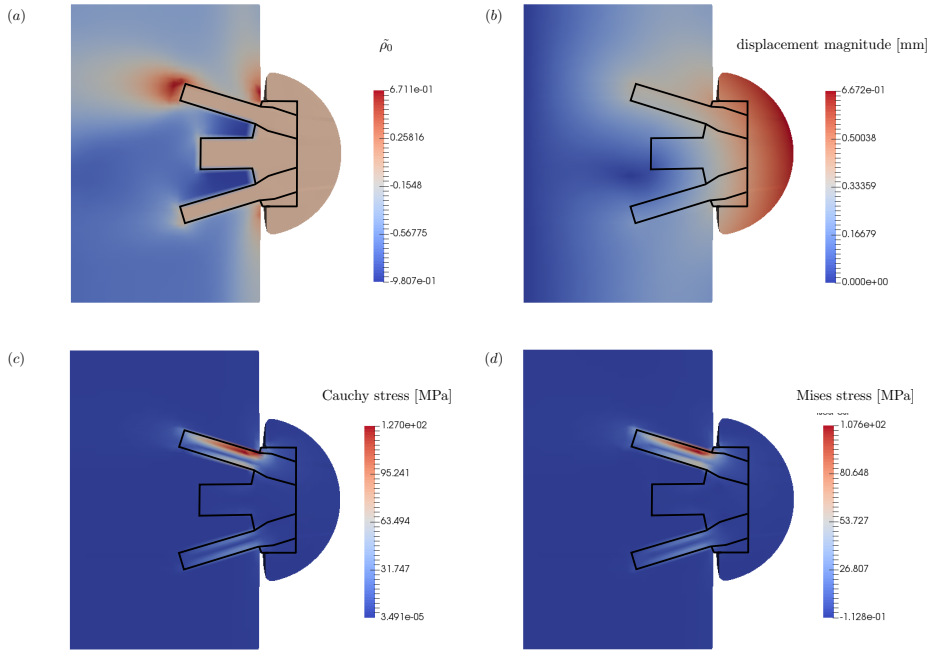

Fig. 7.6: Resulting relative density $\tilde{\rho}_0$ and displacement and stress magnitudes after loading condition 2 was applied for 500 d with $\Delta t = 10$ d with a mass conduction coefficient of $K_0 = 0.01$ mm^{2}d^{-1}.

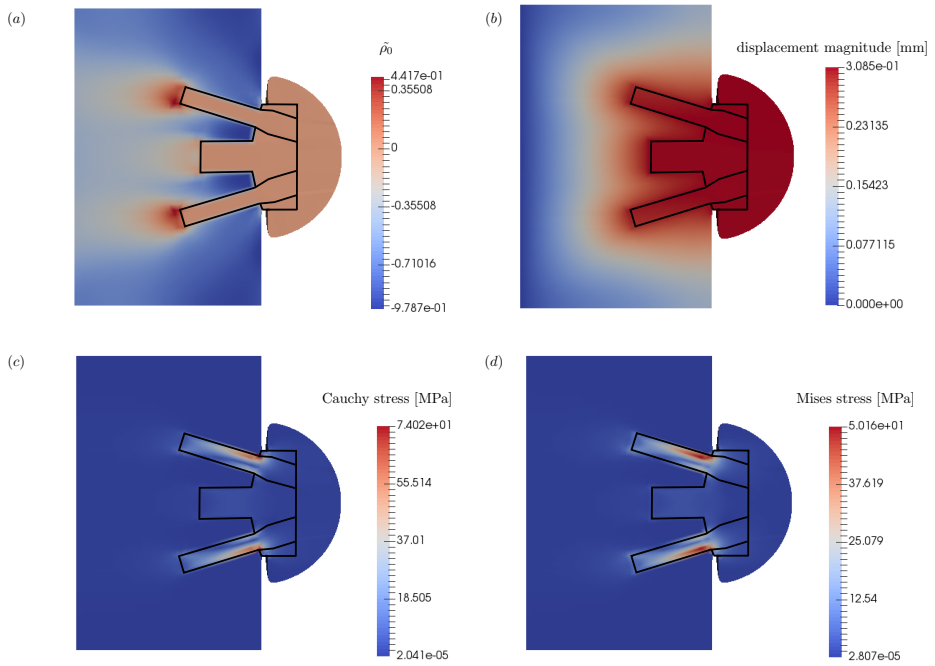

Fig. 7.7: Resulting relative density $\tilde{\rho}_0$ and displacement and stress magnitudes after loading condition 1 was applied for 500 d with $\Delta t = 10$ d with a mass conduction coefficient of $K_0 = 0.005$ mm^{2}d^{-1}.

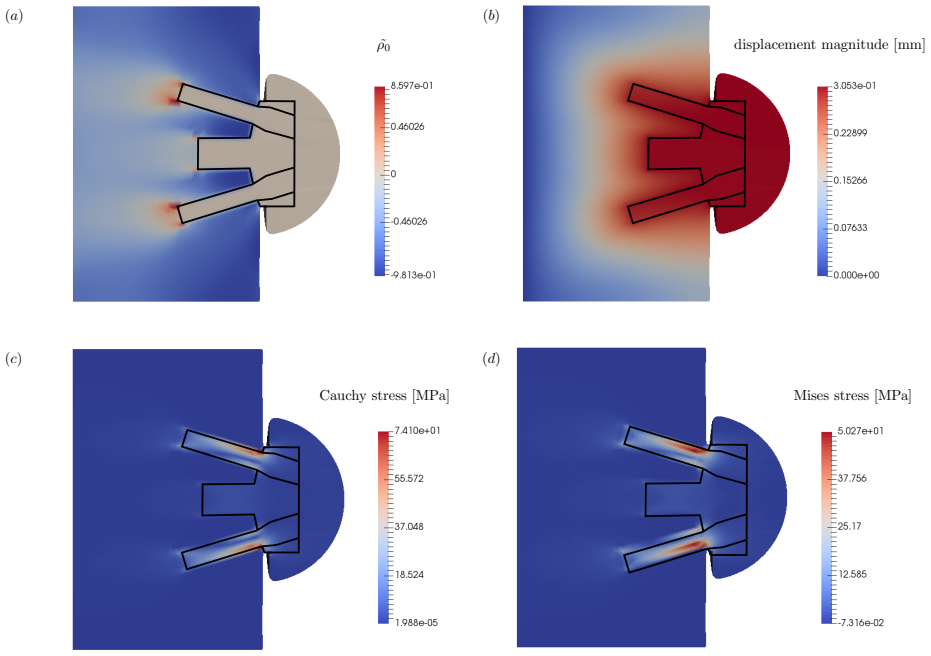

Fig. 7.8: Resulting relative density $\tilde{\rho}_0$ and displacement and stress magnitudes after loading condition 1 was applied for 500 d with $\Delta t = 10$ d with a mass conduction coefficient of $K_0 = 0.00$ mm^{2}d^{-1}.

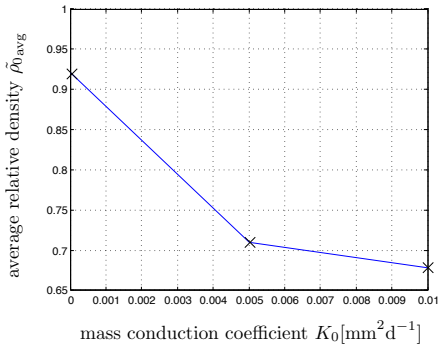

Fig. 7.9: The influence of the mass conduction coefficient of K_0 mm^{2}d^{-1} on the relative density $\tilde{\rho}_0$ after loading condition 1 was applied for 500 d with $\Delta t = 10$ d.

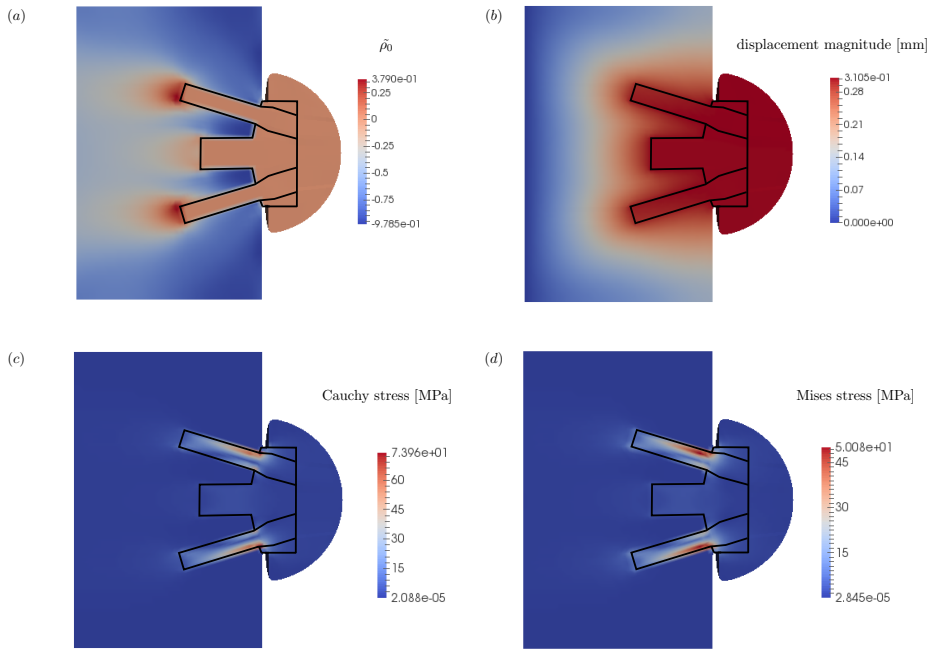

Fig. 7.10: Resulting relative density $\tilde{\rho}_0$ and displacement and stress magnitudes after loading condition 1 was applied for 500 d with $\Delta t = 0.5$ d with a mass conduction coefficient of $K_0 = 0.01$ mm^{2}d^{-1}.

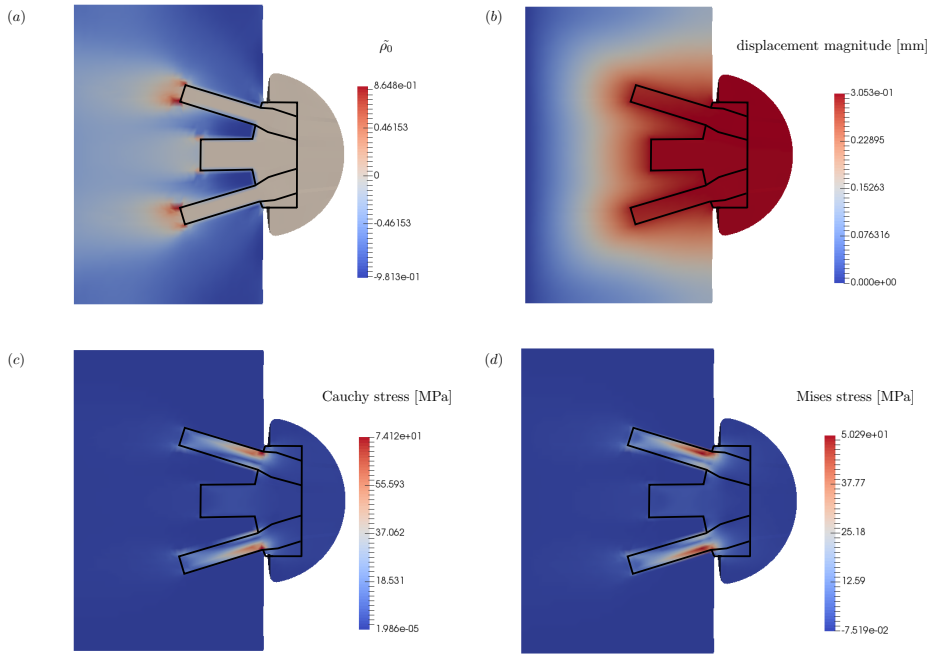

Fig. 7.11: Resulting relative density $\tilde{\rho}_0$ and displacement and stress magnitudes after loading condition 1 was applied for 500 d with $\Delta t = 0.5$ d with a mass conduction coefficient of $K_0 = 0.00$ mm^{2}d^{-1}.

7.2 Scapula

The model for bone remodelling is now applied to predict the response of the intact scapula. The geometry of the scapula was provided by Mutsvangwa et al. (2015). The scapula is a statistical shape model, developed from 70 MRI scans. The BETA CAE pre-processing package ANSA BETACAESystems (2016) and the hexablocking technique were used to mesh the geometry. The mesh was then imported to the AceFEM finite element library.

The boundary conditions were approximated from the boundary conditions reported by Sharma and Robertson (2013), who applied the muscle forces at 90^o abduction. Both sets of boundary conditions are shown in Figure 7.12. The levator scapula and rhomboid forces were omitted in this simulation, as these are small compared to the other forces. The tractions were assumed to act normal to the surface.

The material properties assigned to the scapula are as used for the polyurethane foam block, see Table 7.3. These values are a reasonable approximation of the actual material properties. The mass conduction coefficient was chosen as $K_0 = 0.05\text{mm}^2\,\text{d}^{-1}$ based on the scoping simulations of the polyurethane foam block.

The resulting density distributions from the simulations and the results reported by Sharma and Robertson (2013) are shown in Figure 7.13 (a) and (b) respectively. The solution converges two iterations later than reported by Sharma and Robertson (2013) at $t = 120$ d. The resulting minimum and maximum density values of $\tilde{\rho_0}_{\text{min}} = $ -0.9734 and $\tilde{\rho_0}_{\text{max}} = 1.934$ correspond to densities $\rho_0 = 0.016$ $\text{g}\,\text{cm}^{-3}$ and $\rho_0 = 1.76$ $\text{g}\,\text{cm}^{-3}$. The density distribution is similar to that reported by Sharma and Robertson (2013), who directly enforced the density limits in their simulations to $\rho_0 = 0$ $\text{g}\,\text{cm}^{-3}$ and $\rho_0 = 1.8$ $\text{g}\,\text{cm}^{-3}$, which is the density of cortical bone. Sharma and Robertson also interpolated the actual density values from the CT-scan using the Hounsfield unit. The interpolated density values in Figure 7.13 (b) are labelled "actual" and the simulation results are labelled "predicted". The densities are not identical due to the differences in geometry, applied tractions, muscle attachment points, material parameters and, importantly, the different bone remodelling theory used. The regions of high density coincide with the muscle attachment points, as expected. To accurately model the density distribution in the scapula, more realistic loading conditions should be included in the simulation. The fact that the code could produce a reasonable result considering the above mentioned uncertainties is promising.

Table 7.3: The material properties used in the scapula example.

Young's modulus	$E_y = 193$	Nmm^{-2}
Poisson's ratio	$\nu = 0.25$	
initial density	$\rho_0^* = 0.6$	$\text{g}\,\text{cm}^{-3}$
attractor stimulus	$\Psi_0^* = 0.01375$	Nmm^{-2}
parameter 1	$n = 2$	
parameter 2	$m = 3$	
speed of adaptation	$c = 0.4$	dcm^{-2}
conduction coefficient	$K_0 = 0.05$	mm^2d^{-1}

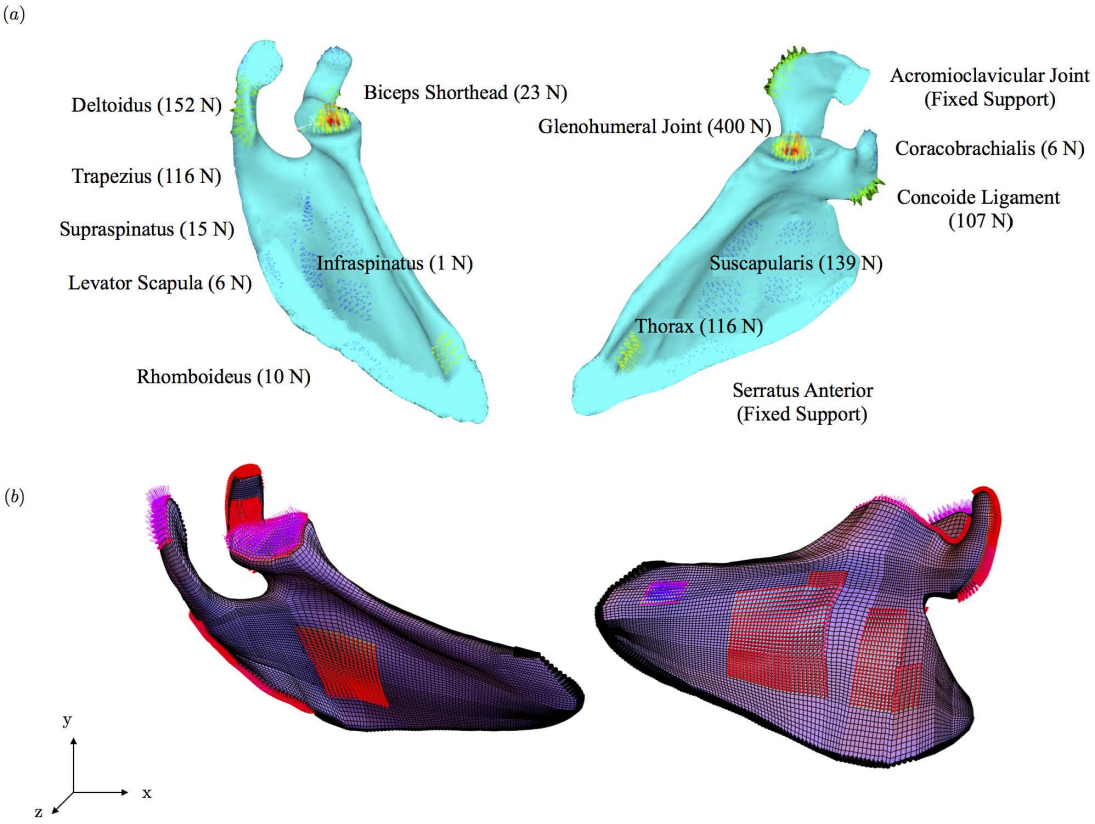

Fig. 7.12: The boundary conditions and geometry reported by (a) Sharma and Robertson (2013) and (b) the model with the boundary conditions used in the simulation.

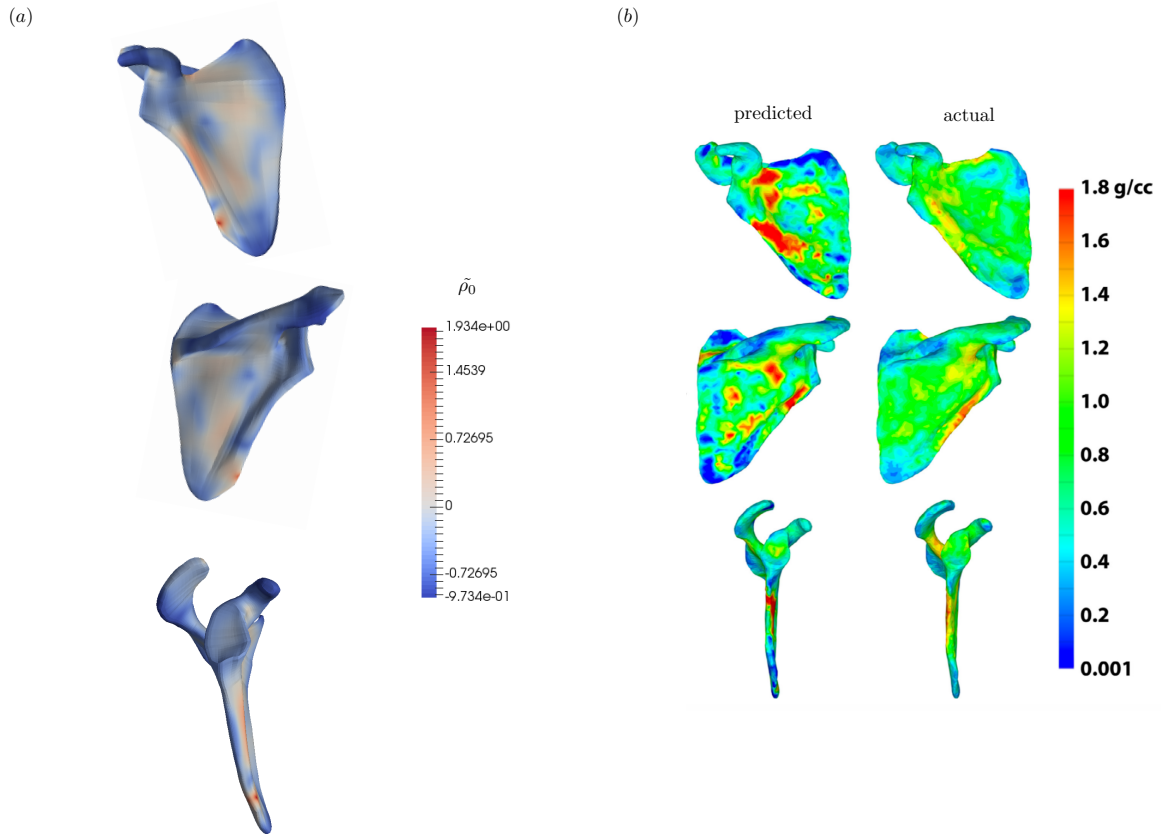

Fig. 7.13: The simulated density distribution in the scapula at $t = 120$ d is shown in (a). The density distributions computed by Sharma and Robertson (2013) are shown in (b), where "actual" corresponds to the density values from the CT scan and "predicted" refers to the simulation results at $t = 100$ d.

7.3 Reverse shoulder

Finally, the finite element code developed here is used to simulate the density remodelling in the scapula post reverse total shoulder arthroplasty. The reverse shoulder prosthesis was virtually implanted in the statistical shape model of the scapula as discussed in the previous sections. The same implant geometry as in the polyurethane foam block example was used. The surgical guidelines defined in the DePuy Delta XTEND reverse shoulder systems surgical techniques (Reconstruction, 2013) were followed. The virtual operation was performed in the CAD software 3-matic (Materialise, 2016a), which is part the CAD package offered by Materialise, whose main product is Mimics, a medical imaging processor (Materialise, 2016b). The components of the model are shown in Figure 7.14.

The magnitudes of the muscle forces were obtained from three patients, whose shoulders were modelled using the Newcastle shoulder model, which was described in Chapter 3.4. The forces were provided at 90^o abduction, which is the same movement used in the model of the intact scapula. However, in the case of the reverse shoulder, the rotator cuff muscles (infraspinatus, supraspinatus, teres minor and subscapularis, see Figure 3.2) are no longer present.

The Newcastle shoulder model produces point-wise muscle attachment points and forces for each muscle. The point-wise forces for each muscle were averaged per patient and then each muscle force was averaged over the three patients. The muscle attachment regions were estimated from the attachment points in the Newcastle shoulder model as well as the BioDigitalHuman application (BioDigitalHuman, 2015). The forces were assumed to act normal to the surface. The force magnitudes are summarised in Table 7.5. The forces were then applied per area of attachment, which was obtained from ANSA, as tractions. The boundary conditions are shown in Figure 7.15.

The same material properties used for the intact scapula and the implant components in the foam block example were used, as detailed in Table 7.4. The mesh consists of 182601 hexahedral elements. The same time-stepping scheme was used with $\Delta t = 10$ d and the solution was run up to $t = 200$ d, where equilibrium was again reached at $t = 120$ d. The average iterations per step are 5.15, where each iteration took on average 0.92 min. The total time for to run the simulation up to $t = 200$ d is 97.5 min. The simulations were done on a Dell PowerEdge R815 with 2 x AMD Opteron 6376 16-core CPUs and 128GB of RAM.

The resulting density distributions are shown in Figure 7.17. The minimum and maximum relative density values of $\tilde{\rho_0}_{\min} = -0.9745$ and $\tilde{\rho_0}_{\max} = 0.6651$ correspond to densities $\rho_0 = 0.0153$ g cm^{-3} and $\rho_0 = 0.999$ g cm^{-3} respectively. It was observed that the regions that do not carry much of the load converge faster than the highly loaded regions. The fast convergence when the density decreases close to the limit of $\tilde{\rho_0} = -1$ has been observed and discussed in Chapter 6.3.

Interestingly, the maximum density is significantly less than reported for the intact scapula. In the reverse shoulder, fewer muscle forces act on the scapula, and the glenohumeral joint contact force, which is the largest force applied on the system, is applied directly onto the prosthesis. This means that the stresses are concentrated in the screws, shown in Figure 7.16, as was also observed in the polyurethane foam block example see for example Figure 7.10. As the screws are bearing the load, the stress in the bone is decreased, which results in a decrease in density. This is a known phenomenon in orthopaedics, termed stress shielding.

The density distribution in the vicinity of the implant is comparable to the results from the polyurethane foam block example. In the regions where the muscle forces are applied, the density increases, as observed in the previous section on the intact scapula. The density falls within the physiologically reasonable range. Of concern, however, is that the density decreases significantly following the reverse shoulder procedure. Especially the regions directly below and adjacent to the metaglene are concerning, as density loss in these regions can lead to implant loosening and ultimately to the failure of the prosthesis, resulting in devastating consequences for the patient. This is the reported cause of failure observed in literature.

A definite conclusion about the remodelling response requires further study. More loading conditions to mimic everyday activities should be considered. The statistical shape model of the scapula used here, should be imported into the Newcastle Shoulder Model so that the muscle attachment points and loading directions on the scapula can be determined accurately for the problem. Further, the material properties of the scapula need to be determined to ensure accurate input data to the model. It is

necessary to calibrate the model parameters against experimental data. Once this has been achieved, a definite conclusion about the remodelling response can be drawn and the model may serve as a predictive tool in the design process of an improved reverse shoulder prosthesis, which promotes bone growth in the regions necessary to ensure secure implant fixation.

Table 7.4: The material properties used in the reverse example.

scapula:		
Young's modulus	$E_y = 193$	Nmm^{-2}
Poisson's ratio	$\nu = 0.25$	
initial density	$\rho_0^* = 0.6$	$\mathrm{g\,cm}^{-3}$
attractor stimulus	$\Psi_0^* = 0.01375$	Nmm^{-2}
parameter 1	$n = 2$	
parameter 2	$m = 3$	
remodelling speed	$c = 0.4$	dcm^{-2}
conduction coefficient	$K_0 = 0.05$	$\mathrm{mm}^2\mathrm{d}^{-1}$
screws and metaglene:		
Young's modulus	$E_y = 117\,000$	Nmm^{-2}
Poisson's ratio	$\nu = 0.3$	
glenosphere:		
Young's modulus	$E_y = 230\,000$	Nmm^{-2}
Poisson's ratio	$\nu = 0.3$	

Table 7.5: The muscle, ligament and joint forces at 90^o abduction. Data provided by collaborators from three patients using the Newcastle Shoulder Model.

muscle	force magnitude
Trapezius	11 N
Levator Sacpulae	0.57 N
Serratus Anterior	10 N
Deltoid Middle	162 N
Coracobrachialis	8 N
Biceps Shorthead	16 N
Concoid Ligament	63 N
Glenohumeral Joint	389 N

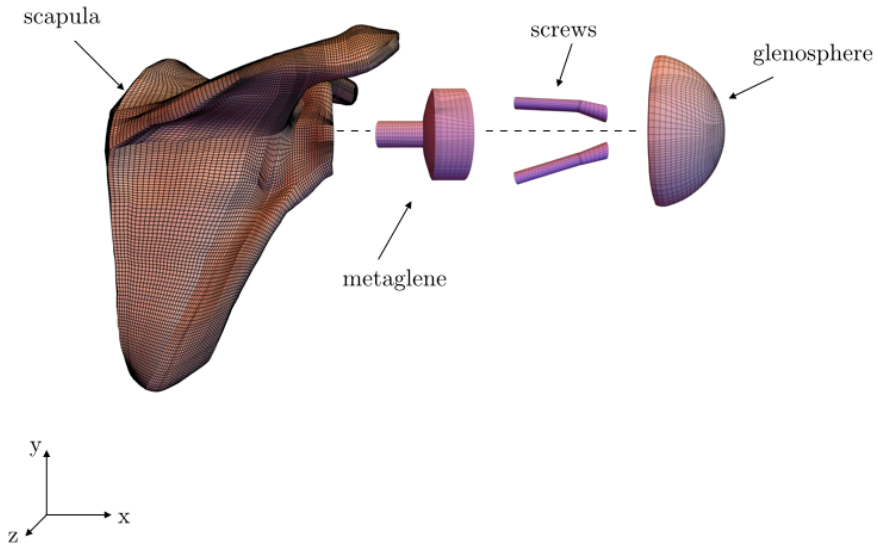

Fig. 7.14: The components of the reverse shoulder.

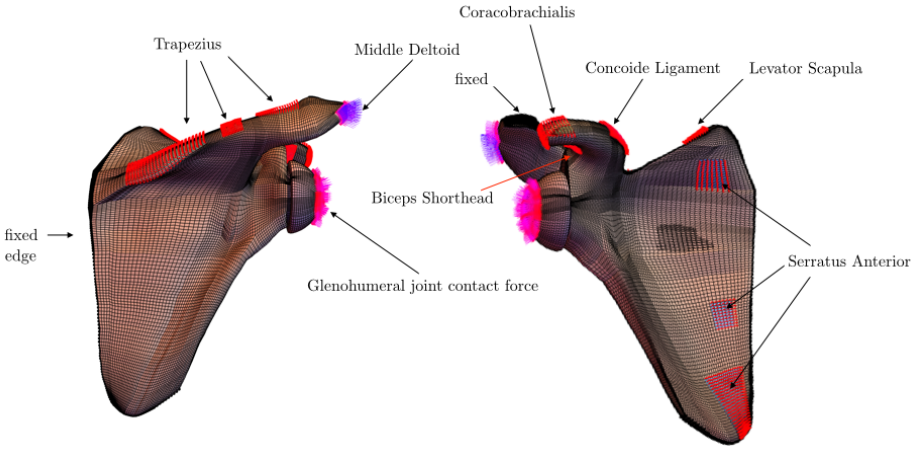

Fig. 7.15: The boundary conditions applied to the reverse shoulder.

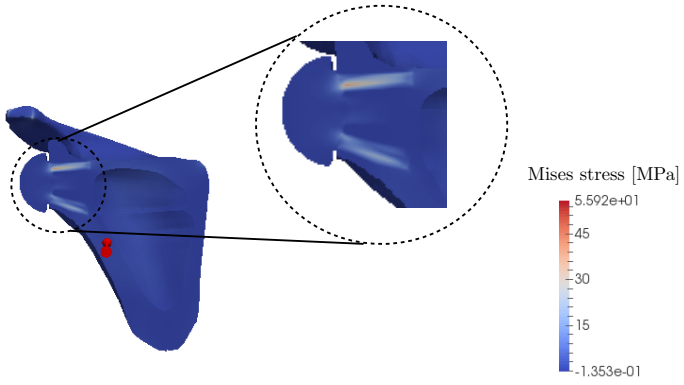

Fig. 7.16: The von Mises stress concentrated in the screws in the reverse shoulder at $t = 120$ d.

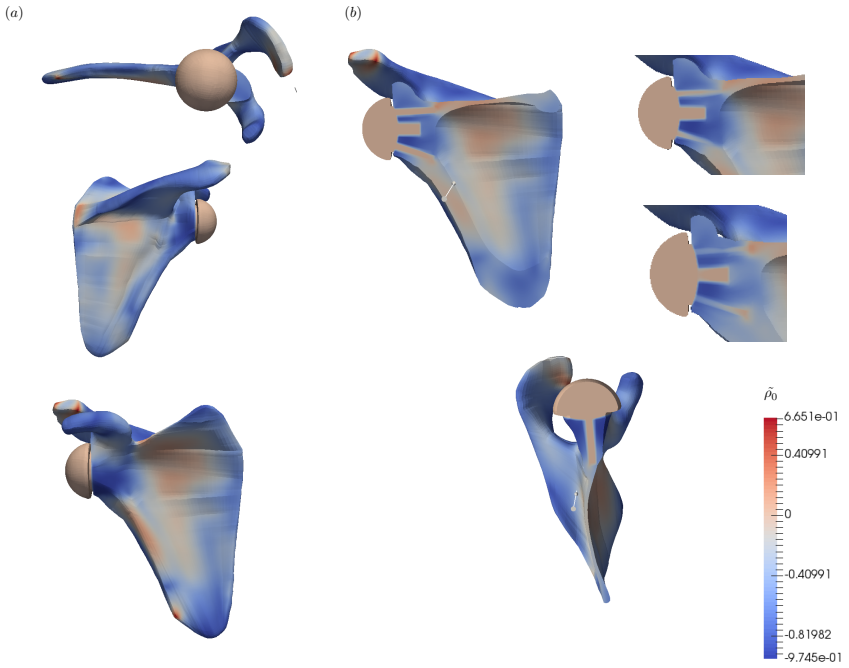

Fig. 7.17: The density distribution in the reverse shoulder after $\Delta t = 10$, at $t = 120$ d. Three views of the scapula are shown in (a) and section views are shown in (b).

8

Discussion and conclusions

A model for the computational simulation of bone remodelling was successfully applied to the scapula post reverse total shoulder arthroplasty. The theoretical underpinning of the remodelling formulation was proposed by Kuhl and Steinmann (2003). The model was implemented in a finite element code using the AceGen library.

The theory is based on open system continuum thermodynamics. The balance of mass and linear momentum are coupled through the density weighted constitutive relations. The balance of mass is defined by a source and flux term analogous to the heat equation, and the balance of linear momentum is the equilibrium equation. The displacements and density were introduced as the degrees of freedom on the nodal level (i.e. they were assumed continuous over the domain) and the coupled problem was solved monolithically using a parallel direct solver.

The finite element code was validated against various benchmark problems reported in the literature. The constitutive relation for bone is based on a density-weighted Neo-Hookean hyperelastic free energy, while the density evolution resembles the heat equation. The remodelling finite element code was then validated against several benchmark problems. Different aspects of the theory were elucidated and features of the model clarified.

The choice of model parameters and constitutive properties for bone is delicate. The material parameters, i.e. the Young's modulus E_y and Poisson's ratio ν, as well as the initial density distribution ρ_0^* should be chosen as the physical properties of the bone under consideration. This is difficult, as a wide range of material properties of bone are reported in literature and furthermore, the material properties of the scapula are not well known. As demonstrated, if the initial density is chosen within a realistic range and applied uniformly to the model, it adjusts as the density evolves according to the loading conditions.

The model parameters n and m capture the material porosity and ensure numerical stability. The parameter n stems from density - material property relations frequently reported in literature for bone and is commonly chosen as 2. Harrigan (1994) reported that numerical stability is ensured if $m > n > 0$, where m is commonly chosen as 3 in literature. These choices were shown to be appropriate.

The remodelling speed c in the mass source term has a small influence on the density magnitudes and the rate of convergence and should therefore be chosen in the calibration process of the model. The mass conduction coefficient K_0 in the mass flux term, however, proved to have the biggest impact on the density bounds (i.e. the maximum and minimum density in the domain). The density bounds do not have to be enforced directly, rather the coefficient can be adjusted. It must not be chosen too large, as this means that the solution is overly smoothed and is no longer meaningful. The mass conduction coefficient and time step size were also shown to have an influence on the rate of convergence, owing to the nature of the continuous and discrete problems. The time at remodelling equilibrium therefore has no obvious physical interpretation.

Finally, the loading should be as realistic as possible, to ensure meaningful results, as the density evolves accordingly. This is achieved by importing the exact geometry into a biomechanical model to accurately determine the muscle attachment points and force vectors.

Once the aspects of the computational model were understood, the shoulder was examined post-procedure. First, the glenoid component of a reverse shoulder implant was placed in a polyurethane

foam block, which was modelled as a hyperelastic material and allowed to undergo remodelling. Densification was observed in the vicinity of the screws, where the stress is concentrated. The greater part of the block does not experience significant loading, resulting in severe density resorption. A bone would therefore not evolve to a non-optimal shape such as the foam block. It was also shown that including the density remodelling is important, as the stress and strain magnitudes change significantly due to the remodelling response of bone. A simple stress analysis of a orthopaedic implant would not capture this important aspect of the behaviour of bone and would produce significantly different results. With a good understanding of the computational model, the remodelling response in the scapula pre- and post-reverse shoulder procedure was investigated.

The finite element model was applied to a statistical shape model of the scapula. The forces at 90^o abduction were taken from literature and applied normal to the surface of the scapula. It is difficult to compare the results to the literature as the geometry, muscle attachment points and even the bone remodelling theory is significantly different. Nevertheless, the results are comparable to Sharma and Robertson (2013) after the mass conduction coefficient is calibrated so that the physical density bounds are enforced. In most other remodelling theories, the density bounds are explicitly enforced, which is not necessary in the current model, as mentioned.

A reverse shoulder prosthesis, as used in the foam block simulation, was implanted in the statistical shape model of the scapula and then analysed. The resulting density values in the scapula post procedure were much smaller than in the intact scapula, due to the absent rotator cuff muscles and because the screws are the load bearing capacity in the system. This results in a densification around the screws and density resorption underneath and adjacent to the implant. This stress shielding phenomenon is a cause for concern, as density resorption around the implant may lead to implant loosening and ultimately failure of the prosthesis. The areas where the muscle forces act, experience density apposition. The model is not yet calibrated and validated against patient data, however, it provides valuable insight to the bone remodelling behaviour post reverse shoulder arthroplasty and is capable of qualitatively comparing different implants (i.e. implant geometries and screw placements). The model can therefore provide insight into the fixation quality of the implants and thereby support the design process so that ultimately, once the full validation and calibration against patient data has taken place, less physical experiments would be necessary to evaluate the success of an implant design.

In conclusion, the remodelling finite element code implemented here provides reliable results. What is outstanding is a comprehensive study of the scapula and calibration of the model parameters against experimental studies. Further, the exact geometry has to be imported to the muscoloskeletal shoulder model and a number of everyday loading scenarios considered. An extension of the model to include anisotropy considerations in the density evolution is also important. Further, modelling contact between the implant and the bone may yield a more physically realistic loading. The finite element model developed here for the scapula could, if extended as suggested, be used as a reliable and powerful predictive tool in the research and design process of orthopaedic devices in the context of reverse shoulder arthroplasty.

A

AceGen Remodelling Element

NOTE: $\rho 0 = \rho_{0}{}^{\sim}$ denotes the relative density [$\rho 0 = \rho_{0}{}^{\sim} = (\rho 0 - \rho 0^{*}) / \rho 0$]

```
<< AceGen`

SMSInitialize["Element", "Environment" → "AceFEM", "Mode" → "Optimal"];
```

Define Element: NoNodes, DOFs

```
FEData[] := (

  nuDOF    = 3;                (* displacement dofs     *)
  nρDOF    = 1;                (* density dofs          *)
  nDOF     = nuDOF + nρDOF;    (* total dofs per node  *)
  nNodes   = 8;                (* number of nodes on element*)
  (* numbering of dofs: first 3 displacements,
  4th one density at each node: *)
  uDOFBeg = 1;
  uDOFEnd  = nuDOF;
  ρDOFBeg  = nuDOF + 1;
 )

FEData[];
```

Element Template

```
SMSTemplate[
  "SMSTopology" → "H1",
  "SMSNoNodes"   → nNodes,
  "SMSDOFGlobal" →  Table[nDOF, {i, nNodes}],
  "SMSSymmetricTangent" → False,
  "SMSDomainDataNames" → {
    "Em      - Youngs modulus",
    "ν       - Poisson ratio",
    "Ψ0star - reference value free energy",
    "ρ0star - reference value of relative density",
    "n       - material parameter (porosity)",
    "m       - material parameter ",
    "c       - governs speed of adaption process [t/L^2]",
    "K0      - mass flux conduction coefficient"
   },
  "SMSDefaultData" → {
    1, 0, 1, 1, 2, 3, 1, 1},
  "SMSPostIterationCall" → True,
  "SMSCharSwitch" → {"L2", "H1", "L2Rho"}
 ];
```

Discretisation

```
Discretisation[] := (

  (* isoparametric domain: Gauss points & shape functions: *)
  Ξ = {ξ, η, ζ} ⊢ Table[SMSReal[es$$["IntPoints", i, Ig]], {i, SMSNoDimensions}];
  Ξ□ = {{-1, -1, -1}, {1, -1, -1}, {1, 1, -1}, {-1, 1, -1},
     {-1, -1, 1}, {1, -1, 1}, {1, 1, 1}, {-1, 1, 1}};
  ℕh ⊨
   Table[1 / 8 (1 + ξ Ξ□[[i, 1]]) (1 + η Ξ□[[i, 2]]) (1 + ζ Ξ□[[i, nuDOF]]), {i, 1, nNodes}];

  (*VALUE OF DOFS: *)
  (* initial coordinates: *)
  𝕏I ⊢ Table[SMSReal[nd$$[i, "X", j]], {i, SMSNoNodes}, {j, SMSNoDimensions}];
  𝕏 ⊢ SMSFreeze[ℕh.𝕏I];

  (*Jacobian: *)
  𝕁 ⊨ SMSD[𝕏, Ξ];
  det𝕁 ⊨ Det[𝕁];

  (* at: current value of jth DOF *)
  ℙI ⊢ Table[SMSReal[nd$$[i, "at", j]], {i, 1, SMSNoNodes}, {j, 1, nDOF}] ;
  ℙe ⊨ Flatten[ℙI];
  𝕦I ⊢ Table[ℙI[[i, j]], {i, SMSNoNodes}, {j, nuDOF}];
  ρI ⊢ Table[ℙI[[i, ρDOFBeg]], {i, SMSNoNodes}];

  (*ap: value of jth DOF at end of previous step *)
  ℙI0 ⊢ Table[SMSReal[nd$$[i, "ap", j]], {i, 1, SMSNoNodes}, {j, 1, nDOF}] ;
  ρI0 ⊢ Table[ℙI0[[i, ρDOFBeg]], {i, SMSNoNodes}];
  (* interpolate values at nodes: *)
  𝕦 ⊨ ℕh.𝕦I;   (* current *)
  ρ ⊨ ℕh.ρI;  (* current *)
  ρn ⊨ ℕh.ρI0; (* previous*)

  (*deformation gradient*)
  D𝕦 ⊨ SMSD[𝕦, 𝕏, "Dependency" → {Ξ, 𝕏, SMSInverse[𝕁]}];
  𝔽 ⊨ SMSFreeze[IdentityMatrix[3] + D𝕦];
  Gradρ ⊨ SMSD[ρ, 𝕏, "Dependency" → {Ξ, 𝕏, SMSInverse[𝕁]}];

  (*value of current real time increment:*)
  Δt ⊨ SMSReal[rdata$$["TimeIncrement"]];

 )
```

Constitutive Equations

```
ConstitutiveEqs[] := (

  (* Material parameters*)
  {Em, ν, Ψ0star, ρ0star, n, m, c, K0} ⊢
   SMSReal[Table[es$$["Data", i], {i, Length[SMSDomainDataNames]}]];
  {λ, μ} ⊨ SMSHookeToLame[Em, ν]; (* constant for all elements *)

  (* STRAIN *)
  detF ⊢ Det[F];
  C ⊨ SMSFreeze[Transpose[F].F];
  (* Right Cauchy Green Strain Tensor *)
  E ⊢ 1 / 2 (C - IdentityMatrix[3]); (* Green-Lagrange Strain Tensor     *)

  (* FREE ENERGY: NeoHookean, impose incompressiblity constraint on BCs *)
  ΨNeo ⊨ 1/2 λ (Log[detF])^2 + 1/2 μ (Tr[C] - nuDOF - 2 Log[detF]);
  Ψ ⊨ (ρ + 1)^(n-1) 1/ρ0star ΨNeo;

  (*SMSPower*)

  Ψ0 ⊨ ρ0star (ρ + 1) Ψ;

  (* Mass Flux *)

  R  ⊨ K0 Gradρ;

  (* Mass source *)

  R0 ⊨ c/ρ0star ((ρ + 1)^-m (Ψ0 + 10^-5 * Ψ0star) - Ψ0star);

  BioStimulus ⊨ (ρ + 1)^-m Ψ0;

  (* STRESS *)

  P ⊢ ρ0star (ρ + 1) SMSD[Ψ, F]; (* First Piola-Kirchhoff stress *)

  S ⊢ SMSInverse[F].P; (* Second Piola-Kirchhoff stress *)

  Ftranspose ⊢ Transpose[F];

  σ ⊢ P.Ftranspose/detF; (* Cauchy Stress *)

  normσ ⊢ SMSSqrt[Tr[σ.σ]];
  normP ⊢ SMSSqrt[Tr[P.P]];
)
```

Subroutine

```
SMSStandardModule["Tangent and residual"];

(* Gauss Points *)
SMSDo[Ig, 1, SMSInteger[es$$["id", "NoIntPoints"]]];

Discretisation[];
ConstitutiveEqs[];

(* Gauss weights *)
wgp = SMSReal[es$$["IntPoints", 4, Ig]];

SMSDo[

  (* density field test function *)
  δρ = SMSD[ρ, ℙe, II];
  (* gradient of density field test function *)
  Gradδρ = SMSD[δρ, 𝕏, "Dependency" -> {Ξ, 𝕏, SMSInverse[𝕁]}];

  (* displacement field test function *)
  fu = Flatten[u];
  δΦ = SMSD[fu, ℙe, II];
  GradδΦ = SMSD[δΦ, 𝕏, "Dependency" -> {Ξ, 𝕏, SMSInverse[𝕁]}];

  (* Residual: Galerkin Method *)

  ℝg = det𝕁 wgp ((1 / Δt) δρ (ρ - ρn)
       + Gradδρ . ℝ
       - δρ R0 + Total[GradδΦ ℙ, 2]);

  (* Residual: Min Pot Energy *)
  (*ℝg=det𝕁 wgp ((1/Δt) δρ(ρ - ρn)
        + Gradδρ . ℝ
        - δρ R0 +SMSD[Ψ,ℙe,II,"Constant" → ρ]);*)

  SMSExport[ℝg, p$$[II], "AddIn" → True];

  SMSDo[
   (* Tangent *)
   𝕂g = SMSD[ℝg, ℙe, JJ];
   SMSExport[𝕂g, s$$[II, JJ], "AddIn" → True];

   , {JJ, If[SMSSymmetricTangent, II, 1], SMSNoDOFGlobal}];
  , {II, 1, SMSNoDOFGlobal}];

SMSEndDo[];
```

Postprocessing

```
SMSStandardModule["Postprocessing"];

(* Gauss Points *)
SMSDo[Ig, 1, SMSInteger[es$$["id", "NoIntPoints"]]];

Discretisation[];
ConstitutiveEqs[];

SMSNPostNames =
  {"DeformedMeshX", "DeformedMeshY", "DeformedMeshZ", "u", "v", "w", "ρ"};

SMSExport[
  Table[ {
    uI[[II, 1]]
    , uI[[II, 2]]
    , uI[[II, 3]]
    , uI[[II, 1]]
    , uI[[II, 2]]
    , uI[[II, 3]]
    , ρI[[II]]
   }, {II, SMSNoNodes}],
  Table[npost$$[II, pp],
   {II, SMSNoNodes},
   {pp, Length[SMSNPostNames]}]];

SMSGPostNames = {
   "E11", "E22", "E33", "E12", "E13", "E23",
   "S11", "S22", "S33", "S12", "S13", "S23",
   "P11", "P22", "P33", "P12", "P13", "P23",
   "sigma11", "sigma22", "sigma33", "sigma12", "sigma13", "sigma23",
   "|sigma|",
   "|P|",
   "detF", "Ψ", "Ψ0", "ΨNeo", "BioStimulus"};

Tensor2Voigt = { {1, 1}, {2, 2}, {3, 3}, {1, 2}, {1, 3}, {2, 3}};

SMSExport[
  Join[
   Extract[𝔼, Tensor2Voigt],
   Extract[𝕊, Tensor2Voigt],
   Extract[ℙ, Tensor2Voigt],
   Extract[σ, Tensor2Voigt],
   normσ {{1}},
   normℙ {{1}},
    detF {{1}},
   Ψ {{1}} ,
   Ψ0 {{1}} ,
   ΨNeo {{1}},
   BioStimulus {{1}}
  ],
  gpost$$[Ig, #1] &];

SMSEndDo[];
```

```
SMSStandardModule["Tasks"];
task ⊧ SMSInteger[Task$$];

SMSIf[task < 0

  , SMSSwitch[task
    , -1,
    SMSExport[{1, 0, 0, 0, 1}, TasksData$$];
    , -2,
    SMSExport[{1, 0, 0, 0, 1}, TasksData$$];
    , -3,
    SMSExport[{1, 0, 0, 0, 1}, TasksData$$];
   ];
  ,

  SMSDo[Ig, 1, SMSInteger[es$$["id", "NoIntPoints"]]];
  wgp ⊧ SMSReal[es$$["IntPoints", 4, Ig]];

  Discretisation[];
  ConstitutiveEqs[];
  SMSSwitch[task
   , 1,
   L2Norm ⊧ detJ wgp (u.u);
   SMSExport[L2Norm, RealOutput$$[1], "AddIn" → True];
   , 2,
   H1Norm ⊧ detJ wgp (u.u + Total[Du Du, 2]);
   SMSExport[H1Norm, RealOutput$$[1], "AddIn" → True];
   , 3,
   L2NormRho ⊧ detJ wgp (ρ * ρ);
   SMSExport[L2NormRho, RealOutput$$[1], "AddIn" → True];
  ];

  SMSEndDo[];
 ];
```

Write Element

```
SMSWrite[];
```

File:	Element.c	Size:	45 739
Methods	No.Formulae		No.Leafs
SKR	320		6301
SPP	229		3893
Tasks	191		2805

B

EBE ethics form

EBE Faculty: Assessment of Ethics in Research Projects

Any person planning to undertake research in the Faculty of Engineering and the Built Environment at the University of Cape Town is required to complete this form before collecting or analysing data. When completed it should be submitted to the supervisor (where applicable) and from there to the Head of Department. If any of the questions below have been answered YES, and the applicant is NOT a fourth year student, the Head should forward this form for approval by the Faculty EIR committee: submit to Ms Zakiya Chikte (Zakiya.chikte@uct.ac.za): New EBE Building, Ph 021 650 5739).
Please note – It is important to keep a signed copy of this form as students must include a copy of the completed form with the dissertation/thesis when it is submitted for examination.

Name of Principal Researcher/Student: HELEN LIEDTKE **Department:** MechEng

If a Student: **Degree:** MSc(MechEng) **Supervisor:** Dr A.T. McBride
Prof. B. D. Reddy

If a Research Contract indicate source of funding/sponsorship:

Research Project Title: COMPUTATIONAL SIMULATION OF BONE REMODELLING POST REVERSE TOTAL SHOULDER ARTHROPLASTY

Overview of ethics issues in your research project:

Question 1: Is there a possibility that your research could cause harm to a third party (i.e. a person not involved in your project)?	YES	(NO)
Question 2: Is your research making use of human subjects as sources of data? If your answer is YES, please complete Addendum 2.	YES	(NO)
Question 3: Does your research involve the participation of or provision of services to communities? If your answer is YES, please complete Addendum 3.	YES	(NO)
Question 4: If your research is sponsored, is there any potential for conflicts of interest? If your answer is YES, please complete Addendum 4.	YES	(NO)

If you have answered YES to any of the above questions, please append a copy of your research proposal, as well as any interview schedules or questionnaires (Addendum 1) and please complete further addenda as appropriate.

I hereby undertake to carry out my research in such a way that

- there is no apparent legal objection to the nature or the method of research; and
- the research will not compromise staff or students or the other responsibilities of the University;
- the stated objective will be achieved, and the findings will have a high degree of validity;
- limitations and alternative interpretations will be considered;
- the findings could be subject to peer review and publicly available; and
- I will comply with the conventions of copyright and avoid any practice that would constitute plagiarism.

Signed by:

	Full name and signature	Date
Principal Researcher/Student:	H. LIEDTKE	29/01/2016

This application is approved by:

Supervisor (if applicable):	B D. REDDY	29/1/2016
HOD (or delegated nominee): Final authority for all assessments with NO to all questions and for all undergraduate research.		03/02/2016.
Chair : Faculty EIR Committee For applicants other than undergraduate students who have answered YES to any of the above questions.		

ADDENDUM 1:
Please append a copy of the research proposal here, as well as any interview schedules or questionnaires:

ADDENDUM 2: To be completed if you answered YES to Question 2:

It is assumed that you have read the UCT Code for Research involving Human Subjects (available at http://web.uct.ac.za/depts/educate/download/uctcodeforresearchinvolvinghumansubjects.pdf) in order to be able to answer the questions in this addendum.

2.1 Does the research discriminate against participation by individuals, or differentiate between participants, on the grounds of gender, race or ethnic group, age range, religion, income, handicap, illness or any similar classification?	YES	NO
2.2 Does the research require the participation of socially or physically vulnerable people (children, aged, disabled, etc) or legally restricted groups?	YES	NO
2.3 Will you not be able to secure the informed consent of all participants in the research? (In the case of children, will you not be able to obtain the consent of their guardians or parents?)	YES	NO
2.4 Will any confidential data be collected or will identifiable records of individuals be kept?	YES	NO
2.5 In reporting on this research is there any possibility that you will not be able to keep the identities of the individuals involved anonymous?	YES	NO
2.6 Are there any foreseeable risks of physical, psychological or social harm to participants that might occur in the course of the research?	YES	NO
2.7 Does the research include making payments or giving gifts to any participants?	YES	NO

If you have answered YES to any of these questions, please describe how you plan to address these issues (append to form):

ADDENDUM 3: To be completed if you answered YES to Question 3:

3.1 Is the community expected to make decisions for, during or based on the research?	YES	NO
3.2 At the end of the research will any economic or social process be terminated or left unsupported, or equipment or facilities used in the research be recovered from the participants or community?	YES	NO
3.3 Will any service be provided at a level below the generally accepted standards?	YES	NO

If you have answered YES to any of these questions, please describe how you plan to address these issues (append to form)

ADDENDUM 4: To be completed if you answered YES to Question 4

4.1 Is there any existing or potential conflict of interest between a research sponsor, academic supervisor, other researchers or participants?	YES	NO
4.2 Will information that reveals the identity of participants be supplied to a research sponsor, other than with the permission of the individuals?	YES	NO
4.3 Does the proposed research potentially conflict with the research of any other individual or group within the University?	YES	NO

If you have answered YES to any of these questions, please describe how you plan to address these issues(append to form)

References

AAOS, 2011. American academy of orthopaedic surgeons - shoulder joint replacement. http://orthoinfo.aaos.org/topic.cfm?topic=A00094, [Online; accessed 15-August-2016].

Ambrosi, D., Ateshian, G. A., Arruda, E. M., Cowin, S. C., Dumais, J., Goriely, A., Holzapfel, G. A., Humphrey, J. D., Kemkemer, R., Kuhl, E., Olberding, J. E., Taber, L. A., Garikipati, K., 2011. Perspectives on biological growth and remodeling. Journal of the Mechanics and Physics of Solids 59 (4), 863–883.

Anglin, C., Tolhurst, P., Wyss, U., Pichora, D., 1984. Mechanical properties of cancellous bone. Proceedings of the First Conference of the ISG, 89–98.

Anglin, C., Tolhurst, P., Wyss, U. P., Pichora, D. R., 1999. Glenoid cancellous bone strength and modulus. Journal of Biomechanics 32 (10), 1091–1097.

Anglin, C., Wyss, U. P., Pichora, D. R., 2000. Glenohumeral contact forces. Proceedings of the Institution of Mechanical Engineers. Part H, Journal of Engineering in Medicine 214 (6), 637–644.

ASTM, 2014. F1839 - 08: Standard Specification for Rigid Polyurethane Foam for use as a Standard Material for Testing Orthopaedic Devices and Instruments. ASTM Book of Standards 13.01 (October), 6–11.

ASTM, 2015. F2028-14: Standard Test Methods for Dynamic Evaluation of Glenoid Loosening or Disassociation 1. ASTM Book of Standards, 1–15.

Berhouet, J., Garaud, P., Favard, L., 2014a. Evaluation of the role of glenosphere design and humeral component retroversion in avoiding scapular notching during reverse shoulder arthroplasty. Journal of Shoulder and Elbow Surgery 23 (2), 151–158.

Berhouet, J., Kontaxis, A., Gulotta, L., Craig, E., Warren, R., Dines, J., Dines, D., 2014b. Effects of the humeral tray component positioning for onlay reverse shoulder arthroplasty design: a biomechanical analysis. Journal of Shoulder and Elbow Surgery, 1–9.

Berliner, J. L., Regalado-Magdos, A., Ma, C. B., Feeley, B. T., 2015. Biomechanics of reverse total shoulder arthroplasty. Journal of Shoulder and Elbow Surgery 24 (1), 150–160.

BETACAESystems, 2016. Ansa the advanced cae pre-processing software for complete model build up. https://www.beta-cae.com/ansa.htm, [Online; accessed 24-October-2016].

BioDigitalHuman, 2015. https://www.biodigital.com/, [Online; accessed 25-October-2016].

Boileau, P., Watkinson, D. J., Hatzidakis, A. M., Balg, F., 2005. Grammont reverse prosthesis: Design, rationale, and biomechanics. Journal of Shoulder and Elbow Surgery 14 (1S), 147–161.

Bonet, J., Wood, R., 2008. Nonlinear Continuum Mechanics for Finite Element Analysis, 2nd Edition. Cambridge University Press, United States of America, New York.

Büchler, P., Ramaniraka, N. A., Rakotomanana, L. R., Iannotti, J. P., Farron, A., 2002. A finite element model of the shoulder: Application to the comparison of normal and osteoarthritic joints. Clinical Biomechanics 17 (9-10), 630–639.

Calais-Germain, B., 2007. Anatomy of Movement, revised english Edition. Easland Press, Seattle,USA.

Campoli, G., Bolsterlee, B., van der Helm, F., Weinans, H., Zadpoor, A. A., 2014. Effects of densitometry, material mapping and load estimation uncertainties on the accuracy of patient-specific finite-element models of the scapula. Journal of the Royal Society 11 (93), 20131146.

Campoli, G., Weinans, H., van der Helm, F., Zadpoor, A. A., 2013. Subject-specific modeling of the scapula bone tissue adaptation. Journal of Biomechanics 46 (14), 2434–2441.

Carter, D. R., Fyhrie, D. P., Whalen, R. T., 1987. Trabecular bone density and loading history: Regulation of connective tissue biology by mechanical energy. Journal of Biomechanics 20 (8).

Carter, D. R., Hayes, W. C., 1977. The Compressive Behavior Porous of Bone Structure as a Two-Phase. The Journal of Bone and Joint Surgery 59 (7), 954–962.

Costantini, O., Choi, D. S., Kontaxis, A., Gulotta, L. V., 2015. The effects of progressive lateralization of the joint center of rotation of reverse total shoulder implants. Journal of Shoulder and Elbow Surgery 24 (7), 1120–1128.

Cowin, S. C., 1999. Bone poroelasticity. Journal of Biomechanics 32 (3), 217–238.

Cowin, S. C., 2004. Tissue growth and remodeling. Annual review of biomedical engineering 6, 77–107.

Cowin, S. C., Cardoso, L., 2015. Blood and Interstitial flow in the hierarchical pore space architecture of bone tissue. Journal of Biomechanics 48 (5), 842–854.

Cowin, S. C., Hegedus, D. H., 1976. Bone remodeling I: theory of adaptive elasticity. Journal of Elasticity 6 (3), 313–326.

Crockett, J. C., Rogers, M. J., Coxon, F. P., Hocking, L. J., Helfrich, M. H., 2011. Bone remodelling at a glance. Journal of Cell Science 124 (7), 991–998.

Currey, J., 1984. Comparative Mechanical Properties and Histology of Bone. American Zoologist 24 (1), 5–12.

Denard, P. J., Lederman, E., Parsons, B. O., Romeo, A. A., 2016. Finite element analysis of glenoid-sided lateralization in reverse shoulder arthroplasty. Journal of Orthopaedic Research, 6–13.

DePuySynthes, 2016. Shoulder replacement. `https://www.depuysynthes.com/patients-and-caregivers/shoulder/shoulder-replacement.html`, [Online; accessed 15-August-2016].

Drake, R., Vogl, W., Mitchell, A. W. M., 2010. Gray's Anatomy for Students. Churchill Livingstone, Elsevier, Canada.

Fernandes, P., Rodrigues, H., Jacobs, C., 1999. A model of bone adaptation using a global optimisation criterion based on the trajectorial theory of Wolff. Computer Methods in Biomechanics and Biomedical Engineering 2 (2), 125–138.

Folgado, J., Fernandes, P. R., Jacobs, C. R., Pellegrini, V. D., 2009. Influence of femoral stem geometry, material and extent of porous coating on bone ingrowth and atrophy in cementless total hip arthroplasty: an iterative finite element model. Computer Methods in Biomechanics and Biomedical Engineering 12 (2), 135–145.

Frich, L. H., Jensen, N., Odgaard, A., Pedersen, C., Sojbjerg, J., Dalstra, M., 1997. Bone strength and material properties of the glenoid. Journal of Shoulder and Elbow Surgery 6 (2), 97–104.

Gibson, L., 1985. The mechanical behaviour of cancellous bone. Journal of Biomechanics 18 (5), 317–328.

Gibson, L. J., 2005. Biomechanics of cellular solids. Journal of Biomechanics 38 (3), 377–399.

Gibson, L. J., Ashby, M. F., 1999. Cellular Solids Structure and Properties, 2nd Edition. Cambridge University Press, Cambrigde.

Gunther, S. B., Lynch, T. L., O'Farrell, D., Calyore, C., Rodenhouse, A., 2012. Finite element analysis and physiologic testing of a novel, inset glenoid fixation technique. Journal of Shoulder and Elbow Surgery 21 (6), 795–803.

Gupta, S., Van Der Helm, F. C. T., Van Keulen, F., 2004. The possibilities of uncemented glenoid component - A finite element study. Clinical Biomechanics 19 (3), 292–302.

Gutiérrez, S., Walker, M., Willis, M., Pupello, D. R., Frankle, M. A., 2011. Effects of tilt and glenosphere eccentricity on baseplate/bone interface forces in a computational model, validated by a mechanical model, of reverse shoulder arthroplasty. Journal of Shoulder and Elbow Surgery 20, 732–739.

Harman, M., Frankle, M., Vasey, M., Banks, S., 2005. Initial glenoid component fixation in "reverse" total shoulder arthroplasty: A biomechanical evaluation. Journal of Shoulder and Elbow Surgery 14 (1S), 162–167.

Harrigan, Timothy P. Hamilton, J. J., 1994. Necessary and sufficient conditions for global stability and uniqueness in finite element simulations of adaptive bone remodeling. International Journal of Solids and Structures 31 (1), 97–107.

Harrigan, T. P., Hamilton, J. J., Reuben, J. D., Toni, A., Viceconti, M., 1996. Bone remodelling adjacent to intramedullary stems: An optimal structures approach. Biomaterials 17 (2), 223–232.

Helgason, B., Perilli, E., Schileo, E., Taddei, F., Brynjólfsson, S., Viceconti, M., 2008. Mathematical relationships between bone density and mechanical properties: A literature review. Clinical Biomechanics 23 (2), 135–146.

Hitzmann, S., 2004. The shoulder complex, part II. http://www.ideafit.com/fitness-library/the-shoulder-complex-part-ii, [Online; accessed 19-August-2016].

Holzapfel, G. A., 2001. Nonlinear solid mechanics - a continuum approach for engineering. John Wiley and Sons, West Sussex, England.

Hopkins, A. R., Hansen, U. N., Bull, a. M. J., Emery, R., Amis, A. a., 2008. Fixation of the reversed shoulder prosthesis. Journal of Shoulder and Elbow Surgery 17, 974–980.

Hsu, S. H., Greiwe, R. M., Saifi, C., Ahmad, C. S., 2011. Reverse Total Shoulder Arthroplasty-Biomechanics and Rationale. Operative Techniques in Orthopaedics 21 (1), 52–59.

Jacobs, C. R., Levenston, M. E., Beaupré, G. S., Simo, J. C., Carter, D. R., 1995. Numerical instabilities in bone remodeling simulations: The advantages of a node-based finite element approach. Journal of Biomechanics 28 (4).

Jacobs, C. R., Simo, J. C., Beaupré, G. S., Cartert, D. R., 1997. Adaptive bone remodeling incorporating simultaneous density and anisotropy considerations. Journal of Biomechanics 30 (96), 603–613.

James, J., Allison, M. A., Werner, F. W., McBride, D. E., Basu, N. N., Sutton, L. G., Nanavati, V. N., 2013. Reverse shoulder arthroplasty glenoid fixation: Is there a benefit in using four instead of two screws? Journal of Shoulder and Elbow Surgery 22 (8), 1030–1036.

Kaczmarczyk, Ł., Pearce, C. J., 2011. Efficient numerical analysis of bone remodelling. Journal of the Mechanical Behavior of Biomedical Materials 4 (6), 858–867.

Kalouche, I., Crépin, J., Abdelmoumen, S., Mitton, D., Guillot, G., Gagey, O., 2010. Mechanical properties of glenoid cancellous bone. Clinical Biomechanics 25 (4), 292–298.

Keaveny, T. M., Hayes, W. C., 1993. Bone. Vol. Volume 7: Bone Growth - B. CRC Press. Inc., United States of America, Ch. 10: Mechanical Properties of Cortical and Trabecular Bone, pp. 285 – 344.

Kontaxis, A., Johnson, G. R., 2009. The biomechanics of reverse anatomy shoulder replacement - A modelling study. Clinical Biomechanics 24 (3), 254–260.

Korelc, J., 2016a. AceFEM system 3.3 the Mathematica finite element environment. https://www.wolfram.com/products/applications/acefem/, [Online; accessed 23-November-2016].

Korelc, J., 2016b. Acegen 3.3 multi-language, multi-environment numerical code generation. https://www.wolfram.com/products/applications/acegen/, [Online; accessed 23-November-2016].

Kuhl, E., 2004. Theory and numerics of open system continuum thermodynamics - spatial and material settings - Habilitationschrift. Fachbereich Maschinenbau und Verfahrenstechnik der Technischen Universitaet Kaiserslautern, Germany.

Kuhl, E., Menzel, a., Steinmann, P., 2003. Computational modeling of growth. A critical review, a classification of concepts and two new consistent approaches. Computational Mechanics 32 (1-2), 71–88.

Kuhl, E., Steinmann, P., 2003. Theory and numerics of geometrically non-linear open system mechanics. International Journal for Numerical Methods in Engineering 58 (11), 1593–1615.

Luijkx, T., Nadrljanski, M., 2016. Computed tomography. https://radiopaedia.org/articles/computed-tomography, [Online; accessed 30-September-2016].

Mansat, P., Barea, C., Hobatho, M.-C., Darmana, R., Mansat, M., 1998. Anatomic variation of the mechanical properties of the glenoid. Journal of shoulder and elbow surgery 7, 109–115.

Mansat, P., Briot, J., Mansat, M., Swider, P., 2007. Evaluation of the glenoid implant survival using a biomechanical finite element analysis: Influence of the implant design, bone properties, and loading location. Journal of Shoulder and Elbow Surgery 16, 79–83.

Materialise, 2016a. Materialise 3-matic. http://biomedical.materialise.com/3-matic, [Online; accessed 23-November-2016].

Materialise, 2016b. Materialise mimics. http://biomedical.materialise.com/mimics, [Online; accessed 25-October-2016].

Mimar, R., Limb, D., Hall, R. M., 2008. Evaluation of the mechanical and architectural properties of glenoid bone. Journal of Shoulder and Elbow Surgery 17 (2), 336–341.

Morgan, E. F., Bayraktar, H. H., Keaveny, T. M., 2003. Trabecular bone modulus-density relationships depend on anatomic site. Journal of Biomechanics 36 (7), 897–904.

MuscoloGraphics, I., 2012-2016. Simm (software for interactive musculoskeletal modeling). http://www.musculographics.com/html/products/simm.html, [Online; accessed 10-November-2016].

Mutsvangwa, T., Burdin, V., Schwartz, C., Roux, C., 2015. An Automated Statistical Shape Model Developmental Pipeline: Application to the Human Scapula and Humerus. IEEE Transactions on Biomedical Engineering 62 (4), 1098–1107.

NCSRR, 2010. National centre for simulation in rehabilitation research - opensim. http://opensim.stanford.edu/, [Online; accessed 25-October-2016].

Nigro, P. T., Gutiérrez, S., Frankle, M. A., 2013. Improving glenoid-side load sharing in a virtual reverse shoulder arthroplasty model. Journal of Shoulder and Elbow Surgery 22 (7), 954–962.

Ohshima, H., 2012. Preventing Bone Loss in Space Flight with Prophylactic Use of Bisphosphonate: Health Promotion of the Elderly by Space Medicine Technologies. https://www.nasa.gov/mission_pages/station/research/benefits/bone_loss.html, [Online; accessed 13-August-2016].

Pomwenger, W., Entacher, K., Resch, H., Schuller-Götzburg, P., 2015. Multi-patient finite element simulation of keeled versus pegged glenoid implant designs in shoulder arthroplasty. Medical and Biological Engineering and Computing 53 (9), 781–790.

Prinold, J. a. I., Masjedi, M., Johnson, G. R., Bull, A. M. J., 2013. Musculoskeletal shoulder models: a technical review and proposals for research foci. Proceedings of the Institution of Mechanical Engineers. Part H, Journal of engineering in medicine 227 (10), 1041–57.

Quental, C., Fernandes, P. R., Monteiro, J., Folgado, J., 2014a. Bone remodelling of the scapula after a total shoulder arthroplasty. Biomechanics and Modeling in Mechanobiology 13 (4), 827–838.

Quental, C., Folgado, J., Fernandes, P. R., Monteiro, J., 2012. Bone remodelling analysis of the humerus after a shoulder arthroplasty. Medical Engineering and Physics 34 (8), 1132–1138.

Quental, C., Folgado, J., Fernandes, P. R., Monteiro, J., 2014b. Subject-specific bone remodelling of the scapula. Computer methods in biomechanics and biomedical engineering 17 (10), 1129–43.

Quental, C., Folgado, J., Fernandes, P. R., Monteiro, J., 2015. Computational analysis of polyethylene wear in anatomical and reverse shoulder prostheses. Medical and Biological Engineering and Computing 53 (2), 111–122.

Reconstruction, D. J., 2013. Delta XTEND reverse shoulder system Surgical technique. revision 8 Edition.

Ribeiro, N. S., Folgado, J., Fernandes, P. R., Monteiro, J., 2011. Wear analysis in anatomical and reversed shoulder prostheses. Computer Methods in Biomechanics and Biomedical Engineering 14 (10), 883–892.

Schileo, E., Taddei, F., Malandrino, A., Cristofolini, L., Viceconti, M., 2007. Subject-specific finite element models can accurately predict strain levels in long bones. Journal of Biomechanics 40 (13), 2982–2989.

Schmidutz, F., Agarwal, Y., Mueller, P., Gueorguiev, B., Richards, R., Sprecher, C., 2014. Stress-shielding induced bone remodeling in cementless shoulder resurfacing arthroplasty: a finite element analysis and in vivo results. Journal of Biomechancis 47, 3509–3516.

Sharma, G. B., Debski, R. E., McMahon, P. J., Robertson, D. D., 2009. Adaptive glenoid bone remodeling simulation. Journal of Biomechanics 42 (10), 1460–1468.

Sharma, G. B., Debski, R. E., McMahon, P. J., Robertson, D. D., 2010. Effect of glenoid prosthesis design on glenoid bone remodeling: Adaptive finite element based simulation. Journal of Biomechanics 43 (9), 1653–1659.

Sharma, G. B., Robertson, D. D., 2013. Adaptive scapula bone remodeling computational simulation: Relevance to regenerative medicine. Journal of Computational Physics 244, 312–320.

SimTK, 2016. Delft shoulder and elbow model. https://simtk.org/projects/dsem, [Online; accessed 5-December-2016].

Singh, A. P., 2012. Cortical Bone and Cancellous Bone. http://boneandspine.com/cortical-bone-and-cancellous-bone/, [Online; accessed 12-August-2016].

Smith, S. L., Li, B. L., Buniya, A., Ho Lin, S., Scholes, S. C., Johnson, G., Joyce, T. J., 2015. In vitro wear testing of a contemporary design of reverse shoulder prosthesis. Journal of Biomechanics 48 (12), 3072–3079.

StanfordUniversity, 2016. Living matter lab. http://biomechanics.stanford.edu/Mechanics_of_growth, [Online; accessed 24-October-2016].

Stone, K. D., Grabowski, J. J., Cofield, R. H., Morrey, B. F., An, K. N., 1999. Stress analyses of glenoid components in total shoulder arthroplasty. Journal of shoulder and elbow surgery 8 (2), 151–158.

Stotts, J., 2015. Understanding kobe bryants rotator cuff injury and the uncertainty it brings. http://instreetclothes.com/2015/01/22/understanding-kobe-bryants-rotator-cuff-injury-uncertainty-brings/, [Online; accessed 15-August-2016].

Taber, L. A., 1995. Biomechanics of growth, remodeling, and morphogenesis. Applied mechanics review 48 (8), 487–545.

Taylor, R. E., Zheng, C., Jackson, R. P., Doll, J. C., Chen, J. C., Holzbaur, K. R. S., Besier, T., Kuhl, E., 2009. The phenomenon of twisted growth: humeral torsion in dominant arms of high performance tennis players. Computer Methods in Biomechanics and Biomedical Engineering 12 (1), 83–93.

Vaupel, Z. M., Baker, K. C., Kurdziel, M. D., Wiater, J. M., 2012. Wear simulation of reverse total shoulder arthroplasty systems: Effect of glenosphere design. Journal of Shoulder and Elbow Surgery 21 (10), 1422–1429.

Virani, N. A., Harman, M., Li, K., Levy, J., Pupello, D. R., Frankle, M. A., 2008. In vitro and finite element analysis of glenoid bone/baseplate interaction in the reverse shoulder design. Journal of Shoulder and Elbow Surgery 17, 509–521.

Waffenschmidt, T., Menzel, A., Kuhl, E., 2012. Anisotropic density growth of bone - A computational micro-sphere approach. International Journal of Solids and Structures 49 (14), 1928–1946.

Weinans, H., Huiskes, R., Grootenboer, H., 1992. The Behavior of Adaptive Bone-Remodeling. Journal of Biomechanics 25 (12), 1425–1441.

Weiner, S., Wagner, H., 1998. The material bone: structuer-mechanical function relations. Annual Review of Material Science 28, 271–298.

Willems, N. M. B. K., Langenbach, G. E. J., Everts, V., Zentner, A., 2014. The microstructural and biomechanical development of the condylar bone: A review. European Journal of Orthodontics 36 (4), 479–485.

Wolff, J., 1892. Das Gesetz der Transformation der Knochen. Hirschwald, Berlin.

Yang, C. C., Lu, C. L., Wu, C. H., Wu, J. J., Huang, T. L., Chen, R., Yeh, M. K., 2013. Stress analysis of glenoid component in design of reverse shoulder prosthesis using finite element method. Journal of Shoulder and Elbow Surgery 22 (7), 932–939.

Yongpravat, C., Kim, H. M., Gardner, T. R., Bigliani, L. U., Levine, W. N., Ahmad, C. S., 2013. Glenoid implant orientation and cement failure in total shoulder arthroplasty: A finite element analysis. Journal of Shoulder and Elbow Surgery 22 (7), 940–947.

Zienkiewicz, O., Taylor, R., Zhu, J., 2005. The Finite Element Method: Its Basis and Fundamentals, 6th Edition. Elsevier Butterworth-Heinemann, Linacre House, Jordan Hill, Oxford OX2 8DP, 30 Corporate Drive, Burlington, MA01803.